Carrier aggregated signal generation for LTE-A

Mohammad Abdi Abyaneh

ParisTech
INSTITUT DES SCIENCES ET TECHNOLOGIES
PARIS INSTITUTE OF TECHNOLOGY

TELECOM ParisTech

EDITE - ED 130

Doctorat ParisTech

T H È S E

pour obtenir le grade de docteur délivré par

TELECOM ParisTech

Spécialité « Communications et Électronique »

Mohammad ABDI ABYANEH

Génération des signaux agrégés en fréquences dans le contexte de LTE-A

Numéro de thèse : 2016-ENST-0062

Directeur de thèse : **Professeur Bernard HUYART**
Co-encadrement de la thèse : **Docteur Jean-Christophe Cousin**

Jury

Mme. Geneviève BAUDOIN, Professeur, ESIEE Paris	Rapporteur
M. Guillaume VILLEMAUD, Maître de Conférences HDR, INSA Lyon	Rapporteur
M. Patrick ROBLIN, Professeur, Ohio State University	Examinateur
M. Aziz BENLARBI-DELAÏ, Professeur, Sorbonne Université-UPMC	Examinateur
M. Guillaume NEVEUX, Maître de Conférences, Université de Limoges	Examinateur
M. Bernard HUYART, Professeur,Télécom-Paristech	Directeur de thèse
M. Jean-Christophe Cousin, Maître de Conférences, Télécom-Paristech	Co-encadrant de la thèse

TELECOM ParisTech
école de l'Institut Mines-Télécom - membre de ParisTech
46 rue Barrault 75013 Paris - (+33) 1 45 81 77 77 - www.telecom-paristech.fr

T H È S E

♣ ♣ ♣

To my dear father ***Hossein*** *and my lovely mother* ***Zahra***

To my ***family***

♣ ♣ ♣

List of Acronyms

3GPP	3rd Generation Partnership Project
ACLR	Adjacent Channel Leakage Ratio
ADC	Analog-to-Digital Converter
ARCEP	Autorité de Régulation des Communications électroniques et des Postes
AWG	Arbitrary Waveform Generator
BER	Bit Error Rate
BP-DSM	Band-Pass Delta-Sigma Modulators
BW	Bandwidth
CA	Carrier Aggregation
CAZAC	Constant Amplitude Zero Auto Correlation
CF	Carrier Feed-through
CP	Cyclic Prefix
DAC	Digital-to-Analog Converter

DDS	Direct Digital Synthesizer
DFE	Decision-Feedback Equalizer
DFT	Discrete Fourier Transform
DL	Down-Link
DPD	Digital Pre-Distortion
DUT	Device Under Test
EDGE	Enhanced Data Rates for GSM Evolution
EVM	Error Vector Magnitude
F-OFDM	Filtered-OFDM
FBMC	Filter Bank Multi-Carrier
FFT	Fast Fourier Transform
FPGA	Field Programmable Gate Array
GFDM	Generalized Frequency Division Multiplexing
GPIB	General Purpose Interface Bus
GPRS	General Packet Radio Service
GSM	Global System for Mobile Communications
HSPA	High Speed Packet Access
HSPA+	Evolved High Speed Packet Access
ICI	Inter Carrier Interference
IDFT	Inverse Discrete Fourier Transform
IFFT	Inverse Fast Fourier Transform
IMT-Advanced	International Mobile Telecommunications-Advanced
IP2	Second Order Intercept Point

IP3	Third Order Intercept Point
ISI	Inter Symbol Interference
ITU	International Telecommunications Union
LAN	Local Area Network
LCM	Least Common Multiple
LIF	Low Intermediate Frequency
LMS	Least Mean Square
LNA	Low Noise Amplifier
LO	Local Oscillator
LPF	Low Pass Filter
LS	Least Square
LTE-A	Long Term Evolution-Advanced
LUT	Look-Up Table
MB-OFDM	Multi-Band Orthogonal Frequency Division Multiplexing
MIMO	Multiple Inputs Multiple Outputs
ML	Maximum Likelihood
MMSE	Minimum Mean Squared Error
MSE	Mean Squared Error
NCO	Numerically Controlled Oscillator
OFDM	Orthogonal Frequency Division Multiplexing
OFDMA	Orthogonal Frequency Division Multiple Access
OOB	Out-of-Band
OSR	Over-Sampling Ratio

PA	Power Amplifier
PAPR	Peak to Average Power Ratio
PLL	Phase Lock Loop
QAM	Quadrature Amplitude Modulation
RF	Radio Frequency
RLS	Recursive Least Square
ROM	Read Only Memories
SC-FDMA	Single Carrier Frequency Division Multiple Access
SDR	Software Defined Radio
SFDR	Spurious Free Dynamic Range
SISO	Single Input Single Output
SMS	Short Message Service
SNR	Signal to Noise Ratio
SSB	Single Side Band
STO	Symbol Timing Offset
TPD	Three-Phase Demodulator
TS	Training Sequence
UFMC	Universal Filtered Multi-Carrier
UL	Up-Link
USRP	Universal Software Radio Peripheral
UWB	Ultra-Wideband

VSA	Vector Signal Analyzer
WCDMA	Wideband Code Division Multiple Access
ZF	Zero-Forcing
ZP	Zero Padding

Abstract

Rose petals let us scatter and fill the cup with red wine
The firmaments let us shatter and come with a new design
-Hafez (1325-1389) Persian poet

LTE-A is introduced by 3GPP as an update on LTE standard. Two main concepts of carrier aggregation (CA) and multiple input multiple output transmissions were added to LTE to respond the increasing demand for data rate. CA consists of transmitting data over different component carriers, simultaneously, in order to obtain more bandwidth in the densely occupied RF spectrum.

In this dissertation, a signal generation structure is proposed using which a multi-tone Local Oscillator (LO) signal is created by a single I/Q modulator. These LOs can be used in the CA receivers to down-convert the transmitted component carriers simultaneously. The multi-tone LO signal structure is further developed to be used at the transmitter as a CA generation solution. Using the proposed structure n-component carriers can be generated in parallel. This structures requires lower sampling rates with respect to the case where RF signals are synthesized directly by digital-to-analog converters. Moreover, less circuitry is required, because one single I/Q modulator is used to generate n component carriers, instead of n I/Q modulators.

This work follows on investigating the origin of impairments and mild nonlinearities in our I/Q modulator. To overcome these problems, we focus on the functionality of the

overall system rather than each component of the I/Q modulator. This method is called behavioral modeling. Once the nonlinear model is obtained, if its inverse function is applied to the input, a linearized output is expected. The generation of the inverse function is called Digital Pre-Distortion (DPD). We propose a tri-band behavioral model for nonlinearities and impairments in tri-band CA using our I/Q modulator. Furthermore, the DPD of the model is evaluated in simulations and experiments.

Finally, this work is concluded with a summary of the results obtained in this research and perspectives are proposed for further studies and applications.

Keywords: LTE-A, carrier aggregation, behavioral modeling, digital pre-distortion, multi-band I/Q modulator, wideband receivers, OFDM, I/Q modulator impairments, nonlinearities

Résumé

Viens t'en, nous effeuillerons la rose et dans la coupe verserons le vin!
Du ciel nous fendrons la voûte et lancerons un plan nouveau
-Hafez (1325-1389) Poet persane.

3GPP a introduit la norme LTE-Avancé (LTE-A) comme la mise à jour de la norme LTE. Elle a ajouté deux concepts d'agrégation en fréquences des bandes LTE et MIMO (*en anglais: Multiple Input Multiple Output*) en réponse à l'augmentation exponentiel de demande de débit de données par les utilisateurs du réseau. L'agrégation en fréquences réalise la transmission de données sur plusieurs porteuses, en parallèle, afin de couvrir une bande passante plus large dans le spectre RF qui est lourdement chargé par d'autres applications.

Dans ce travail de thèse, on a proposé une structure de génération des signaux multi-porteuse afin de créer plusieurs oscillateurs locaux (OL) tout en utilisant qu'un modulateur I/Q. Ces signaux peuvent être utilisés dans les récepteurs de LTE-A pour la transposition des signaux agrégé en fréquence vers la bande de base.

On développe la structure afin de l'utiliser en émetteur répondant aux normes du standard LTE-A. La nouvelle structure nous permet de générer n signaux agrégés en fréquences, de manière simultanée, par une seule chaine de transmission (c.a.d un modulateur I/Q, un OL). En utilisant cette structure on réduit le nombre de circuits utilisés, en comparaison du cas où n signaux agrégés en fréquences sont générés par n émetteurs. La

fréquence d'échantillonnage est réduite dans notre cas par rapport au cas où les signaux sont générés directement de la bande de base à la bande RF avec des convertisseurs analogiques numériques adéquats.

Dans la troisième partie, on se concentre sur les imperfections et les non linéarités du modulateur I/Q dans le cadre de notre structure multi-bande. On modélise le fonctionnement du modulateur multi-bande en utilisant les échantillons en entrée et en sortie. Notre modèle est dérivé de la série de Volterra qui prends en compte les effets non linéaires et les effets mémoires ainsi que les imperfections du modulateur I/Q. Puis, on obtient la fonction "inverse" du modèle et on l'applique à l'entrée du modulateur afin de corriger et linéariser la sortie du modulateur I/Q. La fonction "inverse" est appelée DPD (*en anglais: Digital Pre-Distortion*). Enfin, on a évalué le modèle et la DPD en simulations et en mesures.

A la fin de ce manuscrit, on décrit la conclusion de ce travail de recherche et les directions à suivre pour les futures recherches dans ce domaine.

Mots-Clés: LTE-A, Agrégation en fréquences, DPD, Modulateur I/Q multi-bande, récepteurs très large bande, OFDM, Effets non linéaires, Effets mémoires

Contents

List of Figures

List of Tables

Introduction

Nowadays communications have many different forms. Voice calls, short message service (SMS) and data transmissions are the main forms that are used by network users. To improve the quality of service and to respond the exponentially growing demand for faster and more reliable connections, different technologies have been used throughout the past three decades. From first generation of mobile communications where, only vocal communications were possible, to the fourth generation of mobile communications where high quality video calls are becoming the usual part of the users daily lives. These improvements became possible by evolving structures of transmitters, receivers and core networks. More complex resource allocations algorithms and coding techniques were introduced in digital communications. On the other hand, RF equipment were improved to have a better performance with a lower power consumption and higher autonomy. Besides, optical communications are used as the backbone of the network to carry the massive amount of data.

One of the main factors to improve the data rate in RF communication is the available bandwidth. It is directly proportional to the data rate of the communications. However the RF spectrum is very populated by other users and applications, for example Wi-Fi application is transmitted over frequency bands at 2.4 GHz, 3.6 GHz, 4.9 GHz, 5 GHz and 5.9 GHz. Another example is WiMAX applications where, as stated in IEEE

802.16d and 802.16e, occupies 2.3 GHz, 2.5 GHz, 3.5 GHz and 5.8 GHz. Moreover, the spectrum is an expensive resource for communication operators, for instance, the 4 main operators in France paid 2 798 976 324 Euros, as the licence fee, for LTE applications in 700 MHz band, [703 733] MHz and [758 788] MHz [1]. Hence, it is of great value to use all the small pieces of the available spectrum of the operators to increase the data rate. This idea is proposed by 3rd Generation Partnership Project (3GPP) for LTE-A. The technique is called carrier aggregation (CA). To transmit data over different carriers, simultaneously, multi-band transmitters are needed. Moreover, these signals can have interactions with each other that is an important issue. On the other hand, transmission of wideband signals are vulnerable to frequency selective channels, memory effect, etc. In this dissertation, theses problems are studied and some solutions are proposed to reduce circuitry, cost and consumption of CA systems.

In the first chapter of this dissertation, a structure is proposed for CA receivers which reduces the circuitry and especially the number of local oscillators (LO). At CA receivers, the n component carriers should be down-converted. Thereafter the Low Intermediate Frequencies (LIF) signals should be sampled by analog-to-digital converter (ADC). This is, usually, performed by using n different LOs. The proposed structure consists of a unique LO generating multi-tone continuous wave signal using a particular LIF signal and an I/Q modulator. From original mathematical expressions this particular LIF signal is created using MATLAB® and 2 digital-to-analog converters (DAC). In fact, it is also a multi-tone signal where the tones are distributed over negative and positive LIF in order to reduce the sample frequency of the DAC. Moreover, the structure gives a total control over the amplitude of each tones which is important, since the received component carriers may have different power levels. The proposed LO structure requires one transmission chain, instead of the usual case where n transmission chains are used to create n LOs. Moreover, the practical considerations as well as modulator impairments are analyzed and studied. Finally the structure is simulated in MATLAB® and implemented, in practice, as LOs in a CA receiver. It is also shown that using the proposed structure, sampling rate is much lower than the case where the multi-tone signal is gen-

erated directly from baseband to RF.

In the second chapter of this report, CA transmitter is studied and the multi-tone structure is adapted to be used as component carriers of the CA signal. The chapter begins by description of orthogonal frequency division multiplexing (OFDM) modulation and demodulation. The practical aspects of the OFDM signal implementation, such as time and frequency synchronization of the signal, is explained. Then, a hybrid frequency synchronization method is proposed. The chapter follows by a frequency diversity solution, where an identical OFDM symbol is transmitted over different component carriers. The structure is further developed to be used as a CA transmitter. Different OFDM signals are modulated over different component carriers as required in LTE-A transmitter. The structure is developed and implemented for a case with 3-component carriers. Like the case of multi-tone structure, DAC sampling rate is significantly reduced. Moreover, n transmitters (1 transmitter per component carrier) are replaced by one in the proposed structure. Furthermore, I/Q modulator impairment in the case of CA transmitter are studied and a look-up table compensation solution is proposed. The chapter ends with experimental implementation of the CA structure and demodulation of the component carriers using two different receivers, which are a multi-band three-phase demodulator and a mono-band vector signal analyzer. Finally, the results are compared to the state of the art to evaluate their performances.

In the last chapter of this document, the compensation of impairments and mild nonlinearity of the I/Q modulator of our structure is focused on. Behavioral modeling is used to modelize the functionality of our multi-band I/Q modulator. The chapter begins by citing the state of the art mono-band and multi-band behavioral models. The process of finding the "inverse" of the behavioral model or the digital pre-distorter (DPD) is explained in details. A three-band behavioral model is proposed which includes the mild nonlinearities as well as the I/Q modulators gain and phase imbalances. The DPD signal is obtained using indirect learning and least square algorithm. The model and the DPD are simulated by MATLAB® and experimentally implemented using an arbitrary waveform generator. Simulation shows a significant improvement for the means squared

error of the output of the I/Q modulator. Finally, experimental implementation shows the compensation of the I/Q modulator impairment, but some spectral regrowth are observed at the output of the I/Q modulator which their origin is explained.
Finally, the dissertation ends with the conclusion of this research and perspectives for future works are proposed.

Chapter 1

Multi-Tone Signal Generation

Many applications in radio frequency (RF) communications require multi-tone signaling. They can be used in electromagnetic compatibility tests as multi-source frequency illumination for the device under test (DUT) [2][3]. They are used in the nonlinearity measurements of the mixers, power amplifiers (PA) to characterize their intermodulation parameters such as the second order intercept point (IP2) and the third order intercept point (IP3) [4]. Another important application of multi-tone signals is seen in multi-band heterodyne/superheterodyne receivers where they can play the role of local oscillators (LO) for down-conversion of the RF signals to baseband or low intermediate frequencies (LIF). Multiple local oscillators are proposed in different technologies. Long term evolution-advanced (LTE-A) uses them for the down-conversion of the carrier aggregated signals [5][6]. Moreover, to increase the data rate in 5G, CA is proposed which endorses the importance of multi-tone signals as LOs.

1.1 State of the Art

Several works have been elaborated on multi-tone signaling. In [7], a 4-tone signal generation method is proposed where a local oscillator functions in time division multiplexing

regime using digital registers and adders. The digital signal is then converted to analog using a delta sigma DAC. However, there are two drawbacks: First, the more tones are used and the more separated they are, the higher becomes the DAC sampling frequency. Second, the fact that to generate RF signals directly from baseband, a very powerful DAC is required. Based on Nyquist criterion the sampling frequency must be at least twice as the highest frequency component, meaning over-sampling ratio (OSR) of two. Moreover for practical reasons a higher order OSR is used. For example, to synthesize a 4-tone RF signal with the highest tone at 2 GHz a DAC with a clock frequency of 8 GHz is required to ensure an OSR of 4. In another work, Traverso *et al.* [8] proposed a synthesizer to create a multi-band orthogonal frequency division multiplexing (MB-OFDM) used in IEEE 802.15.3a. 14 channels of 528 MHz of bandwidth (14×528 MHz), are created using one phase lock loop (PLL), 4 divide-by-two circuits, one broadband single side band (SSB) mixer and 4 SSB mixers as shown in Figure 1.1. This method can be adapted to the case of CA, by making up to 5 component carriers. However, there is a huge constraint on the frequency allocations, since the channels must be placed at divisions by two of the center frequency [9]. In a study to minimize the the peak to av-

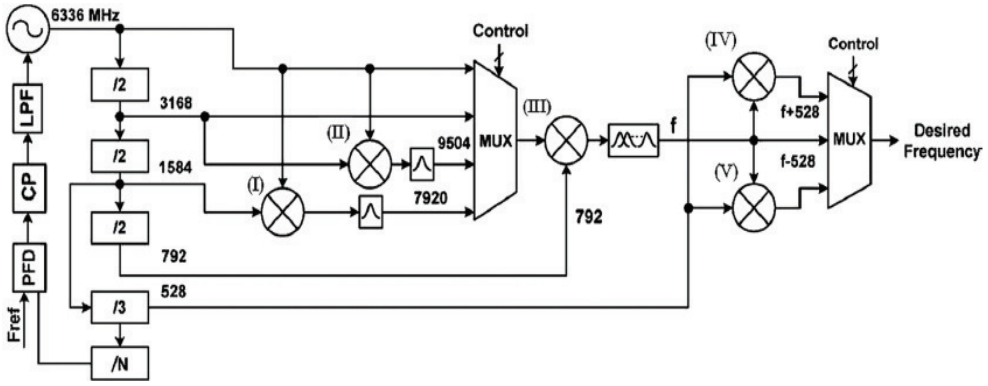

Figure 1.1: Multi-band OFDM synthesizer

erage power ratio of a multi-tone signal [10], two minimization methods are proposed for the cases with 3, 5, 7 and 9 tones. The first method ensures the phase synchronization of each tone at baseband by modifying, numerically, each phase. The second method proposes phase adjustment method in RF domain which yields to a better result in their

study. However, there are some limitations in their multi-tone signal generation. Firstly, only an odd number of tones are generated using their methods. Secondly, the tones are generated at equidistant frequencies. Thirdly, no control on the amplitudes is given and they are taken to be equal. Hence, there are severe constraints for the user in frequency configuration and power transmission at each tone. Keysight implemented multi-tone signaling in its signal generators [11] which follows the concept of generating equidistant tones centered around an RF carrier. Moreover, one can turn off the undesired tones to make a suitable frequency configuration, as shown Figure 1.2. The method has some severe constraints since the tones should be generated with at least a separation of Δf which limits the reconfiguration of the multi-tone signaling in communication systems. As previously mentioned, multi-tone signaling can be used in multi-band receivers which require a highly re-configurable LOs, in terms of transmission frequency and amplitude.

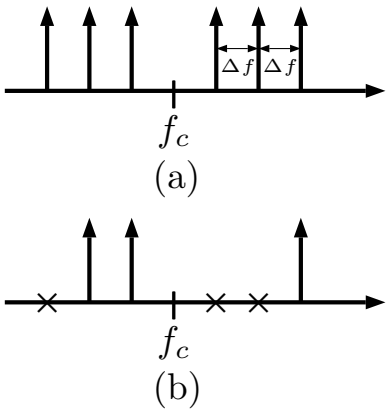

Figure 1.2: Multitone signal generation by making many tones and eliminating the undesired ones

Another possibility is to use direct digital synthesizers (DDS) to generate periodic signals, including, multi-tone signals [12]. A DDS is a sampled based system. It consists of a reference clock frequency, a phase accumulator, a numerically controlled oscillator (NCO) and a DAC. The signal is transformed to phase information and saved in an N-bit accumulator and then by using a look-up table (LUT) each code-word of the accumulator

is mapped to a waveform sample of the signal. At the last part, the analog waveform is generated by the DAC. DDS gives a good control on the resolution and the frequency allocation of the signal. The output frequency of a DDS system is given by equation (2) of [12]-[13].

$$F_o = \frac{F_{clk}}{2^N} \Delta_{ACC} \tag{1.1}$$

Where F_o, F_{clk}, N and Δ_{ACC} are the output frequency, sampling clock frequency, the length of the accumulator and phase increment of the accumulator, respectively. The output frequency can be with a very good precision for any frequency up to $\frac{F_{clk}}{2}$. On the other hand, there are some limitations too, for instance, the DAC harmonic products are directly proportional to $\frac{F_{clk}}{f_o}$ that reduces the spurious free dynamic range (SFDR) of the system. This is mainly due to the fact that quantization error of the DAC varies with this ratio. A solution to this problem is to make a small offset on the output frequency so that the ratio does not make an integer number of the clock frequency. However, this increases the phase noise of the signal [13]. We purchased a DPG3 of Analog Devices, which is a digital pattern generator, with its evaluation board. It is DDS based signal generation solution proposed by Analog Devices. However its waveform length must be an integer multiple of 256 samples which is an important limitation for our application. For instance, a modulated signal with 2048 QPSK symbols and an oversampling ration of 6 filtered by a root raised cosine FIR filter and a roll-off factor of 0.35 has 12480 samples which is not an integer multiple of 256. Hence, we switched to arbitrary waveform generators (AWG) which give us more degrees of freedom.

1.2 Carrier Aggregation

One of the main parameters to increase the data throughput is the available bandwidth. The LTE-A standard increases the required available signal bandwidth to 100 MHz, which is a very large bandwidth in RF spectrum for mobile operators. This bandwidth is achievable via CA in which data are distributed over up to 5 modulated carriers of 20 MHz of bandwidth. The bandwidths of each modulated carrier can be chosen from

1.4 MHz, 3 MHz, 5 MHz, 10 MHz, 15 MHz and 20 MHz for different data rates. The number of up-link and down-link carriers can be different but there must be more carriers in down-link than up-link [14]. Three types of CA are proposed by release 10 of 3GPP; contiguous intra-band, non-contiguous intra-band and non-contiguous inter-band [15]. The first CA configuration places the carriers next to each other within the same band; the second configuration consists of distributing the data over different carriers which are placed separately over the same frequency band. The third CA configuration places the carriers far from each other over different bands. Figure 1.3 summarizes the three CA configurations.

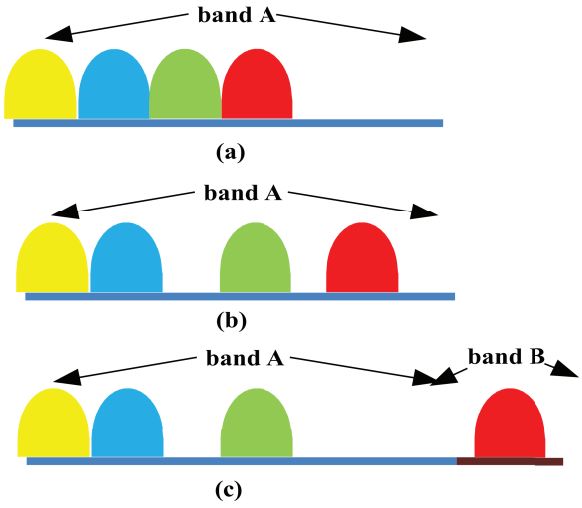

Figure 1.3: Carrier aggregation types. (a) Contiguous intra-band (b) Non-contiguous intra-band (c) Non-contiguous inter-band

At the receiver the aggregated signals should be down-converted. Down-conversion is feasible using several methods such as under-sampling, wave-correlator circuit (six-port junction) with diodes and down-conversion by mixers (three-phase demodulators). The aliasing effect due to under-sampling can be taken as an advantage in down conversion of a signal. When a signal at frequency f_1 is sampled at a lower frequency f_2 , a copy of the signal is placed at $f_1 - f_2$. For example, if a signal is transmitted at 40 MHz with a bandwidth (BW) of 2 MHz and sampled at 30 MHz then at the output of the

ADC, a copy of the signal, with a BW = 2 MHz, is centered at 10 MHz. This method is not practical for down-conversion of RF signals since an ADC which has a very high sampling rate (×10 Gbps), have huge power consumption and their dynamic range are not enough for the data processing of radio signals.

Down-conversion using a wave-correlator is also a method of interest in which the RF signal is injected to one port of the six-port circuit and the LO signal is fed to another port. The four other ports are terminated with power detectors[16]. The problem of this method is the high conversion loss of the down-converted signal. Besides, the dual-band signal is down-converted by two LOs at different frequencies, which means additional circuitry for each band. A dual-band RF signal with center frequencies at $f_1 = 2.5$ GHz and $f_2 = 3$ GHz at 0 dBm is down-converted at Zero-IF and LIF, as shown in Figure 1.4, with 43 dB of conversion loss. This loss is mainly due to the power detectors that are used at the four outputs of the six-port circuit. In [17], a three-component CA signal is demodulated using a ultra wide-band receiver which makes a demodulation of the 3 component carriers using a single data acquisition, feasible. However the receiver uses 3 LOs to down-convert the CA signals to LIF bands which increases the cost in terms of power consumption, area occupation and price. A good idea to solve the circuitry overuse of [16], [17] is to use a multi-tone signal as the LOs, which gives good degrees of freedom in terms of the frequency, power allocation for CA applications.

1.3 Multi-tone Local Oscillator Using a Single Signal Generator for Carrier Aggregation Receivers

There are several demodulation options for CA signals. The first option requires a mono-band receiver which down-converts each component carrier to zero intermediate frequency and demodulates them, sequentially. This clearly cannot be a suitable option for real time communications. The second option is constituted of N narrow-band receivers for N component carriers, which may perform in real-time applications at the expense of repetitive circuitry. Moreover, these receivers need to be synchronized. The third

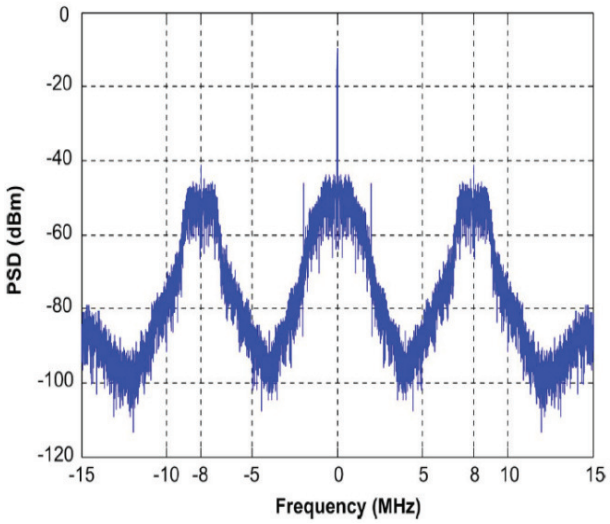

Figure 1.4: Zero-intermediate frequency down conversion using a six-port circuit with power detectors

option consists of a wide-band receiver with one LO signal. It can be a good option for contiguous and intra-band CA, but its impractical for inter-band CA since a strong ADC with a high clock frequency is needed to sample properly such a wide-band signal. The fourth option is using N LO signals for N component carriers, to down-convert them, simultaneously. These options are depicted in Figure 1.5.

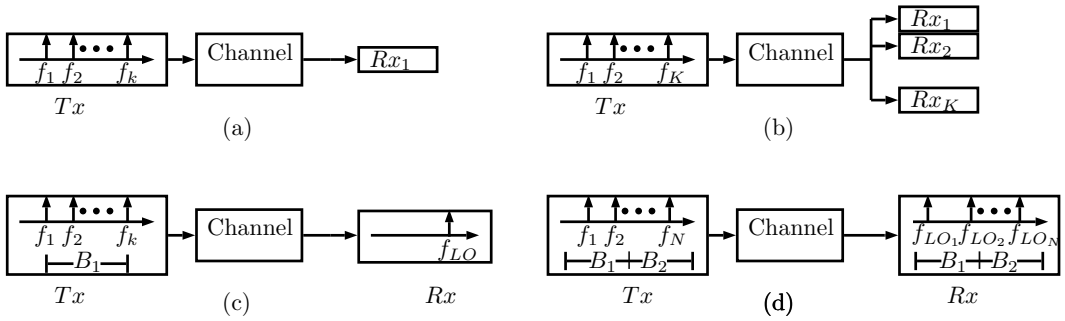

Figure 1.5: Different receiver possibilities. (a) Narrow and mono-band receiver. (b) Multiple narrow and mono-band receivers. (c) Wide and mono-band receiver. (d) Wide and multi-band receiver

Since the strategy (d) uses a single receiver for demodulation of n bands, simultaneously, it appears to be the best and will be detailed in the rest of this chapter.

1.3.1 M-Tone Signal Generation Method

We would like to replace N LOs that are used in Figure 1.5(d) by one LO to generate the same signal. One obvious way would be to synthesize directly the multi-tone signal which is not a good option since you would require a powerful DAC to generate such a signal. For example, to generate a multi-tone signal with the highest tone at 2.5 GHz and an OSR of 4, a DAC capable with a clock frequency of 10 GHz is required. Therefore, an option is to create the signals at LIF band and up-convert them using an RF modulator. N-tone signal can be written as :

$$x(t) = Re\{\sum_{k=1}^{N} \alpha_k e^{i(2\pi f_k t + \theta_k)}\} \tag{1.2}$$

where $x\,(t)$ is the RF multi-tone signal, $Re\{\}$ represents the real part, α_k, θ_k, f_k are amplitude, phase and RF frequency of the k^{th} tone, respectively. N is the number of tones and t is the time. It can be re-written as:

$$x(t) = Re\{(\sum_{k=1}^{N} \alpha_k e^{i(2\pi h_k t + \theta_k)}) e^{i2\pi f_c t}\} \tag{1.3}$$

where h_k are the frequencies of the LIF tones, f_c is the carrier frequency of the LO, θ_k, f_k are amplitude, phase and RF frequency of the k^{th} tone, respectively. N is the number of tones. We can extend the (1.3) as I/Q components of a baseband signal as following:

$$x\,(t) = Re\{(I\,(t) + jQ\,(t))\, e^{i2\pi f_c t}\} \tag{1.4}$$

With:

$$I\,(t) = \sum_{k=1}^{N} \alpha_k cos\{2\pi h_k t + \theta\}$$

$$Q\,(t) = \sum_{k=1}^{N} \alpha_k sin\{2\pi h_k t + \theta\}$$

In other words, the tones are distributed over the negative and positive low intermediate frequencies. This reduces the DAC sampling frequency because based on the Nyquist rate, the DAC sampling frequency must be at least twice the highest frequency component to avoid aliasing. The highest frequency, in absolute value, is reduced because the tones are not only generated on the positive frequencies but on the both sides. From (1.3) one can see that there are N equations and N+1 unknowns which lead to an infinite number of solutions so we need another condition to make a proper choice on h_n and f_c. Among all these frequency configurations there is one that can minimize the DAC sampling frequency.

Using (1.3) we can write the following:

$$f_k = h_k + f_c \qquad for \qquad k = 1, 2, ..., N \tag{1.5}$$

hence,

$$f_{DAC} > OSR * max\{\mid h_k \mid\} \tag{1.6}$$

where OSR is the oversampling ratio.

To minimize (1.6) we should minimize the highest frequency component in absolute value meaning that the highest frequency component at the positive or negative sides must be equidistant from the origin (0 Hz). Hence, if we consider $h_1 < h_2 < ... < h_N$ then:

$$\frac{h_1 + h_N}{2} = 0 \tag{1.7}$$

by replacing (1.5) in (1.7) one may obtain :

$$f_c = \frac{f_1 + f_N}{2} \tag{1.8}$$

Remark 1.1. Since the Nyquist criterion deals only with the highest frequency component, the DAC sampling frequency is minimized only by the position of the two extreme tones and the rest of the tones, in between, do not control it.

From (1.5) we can deduce the frequency configurations of the LIF components (h_k) which lead to the desired RF frequencies. An example of a three-tone LIF signal is given

in Table 1.1. Figure 1.6 shows the PSD of the LIF signals. The PSD is obtained using the *fft* and *fftshift* function of MATLAB® to calculate the fast Fourier transform (FFT) of the signal and to consider the 0 Hz as the center frequency, respectively. By (1.8), these signals can be up-converted using a carrier at $f_c = 2.35$ GHz to generate RF tones at 2.00 GHz, 2.3 GHz and 2.7 GHz. Figure 1.6(a) and (b) show the PSD of the in-phase ($I(t)$) and in quadrature ($Q(t)$) parts, respectively. There are six spectral components, three of which correspond to the LIF signals and three others correspond to their images. Since the image of the signal happens at the exact opposite position with respect to the origin, the image of the two extreme LIF signals overlap with LIF signals. Therefore, only the image of the middle LIF signal is visible. Figure 1.6(c) shows the PSD of the complex envelop where the images are removed because of the 90° phase difference between $I(t)$ and $Q(t)$

	h_1	h_{im1}	h_2	h_{im2}	h_3	h_{im3}
LIF (MHz)	-350	350	-50	50	350	-350

Table 1.1: LIF tones and corresponding images.

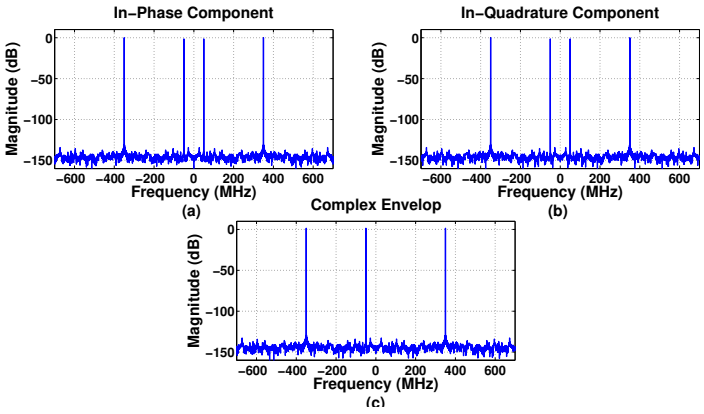

Figure 1.6: Three-tone LIF signals with h_1 @ -350 MHz, h_2 @ -50 MHz and h_3 @ 350 MHz (a) In-phase component ($I(t)$) (b) In-quadrature component ($Q(t)$) (c) Complex envelop ($I(t) + jQ(t)$).

Signal generation with practical modulators is not as perfect as it is on simulations where I/Q components are perfectly matched. Hence, we need to take into account the imperfections.

1.4 I/Q Mismatch Effect on Multi-tone Signal Generation

There are many source of imperfections which modify the transmission quality such as bit error rate (BER), error vector magnitude (EVM), spectral purity, etc. There are three main modulator imperfections.

- Gain imbalance
- Phase imbalance
- Offset imbalance

The gain imbalance can be originated from the gain imbalance of the DAC applied to the I and Q paths, the loss imbalance of the I and Q paths of the modulator or both of them. The phase imbalance occurs in the LO signal 90° phase split. The phase split is, mostly, performed by poly-phase filters or divide by two flip flops where imperfections may exist [18] [19]. The offset imbalance of the modulator is occurred, when DC voltage applied on I path is different than the one applied on the Q path. Let's analyze mathematically the effect of each imperfection. The in-phase ($I(t)$) and in-quadrature ($Q(t)$) component of the baseband signal become as follow:

$$\begin{aligned} I\left(t\right) &= \sum_{k=1}^{N} \alpha_k \beta_{k_I} cos\{2\pi h_k t + \theta + \phi_{k_I}\} + C_I \\ Q\left(t\right) &= \sum_{k=1}^{N} \alpha_k \beta_{k_Q} sin\{2\pi h_k t + \theta + \phi_{k_Q}\} + C_Q \end{aligned} \tag{1.9}$$

Where $G_k = 20log(\frac{\beta_{k_Q}}{\beta_{k_I}})$, $\Phi_k = \phi_{k_I} - \phi_{k_Q}$, C_I, C_Q are the gain of imbalance, the phase imbalance and the DC offset of the in phase and in quadrature components, respectively. Note that these parameters are not identical at different frequencies since the equipment

do not have the same frequency response at all the frequencies. By replacing (1.9) in (1.4) the output of the modulator can be written as:

$$x(t) = Re\Bigg(\sum_{k=1}^{N} \Big[\frac{\alpha_k}{2} \left(\beta_{k_i} e^{i\theta_{k_i}} + \beta_{k_Q} e^{i\theta_{k_Q}} \right) e^{i(2\pi h_k t + \theta_k)} + \frac{\alpha_k}{2} \left(\beta_{k_i} e^{-i\theta_{k_i}} - \beta_{k_Q} e^{-i\theta_{k_Q}} \right) e^{-i(2\pi h_k t + \theta_k)} + C \Big] e^{i(2\pi f_c t)} \Bigg) \quad (1.10)$$

These imbalances lead to different phenomena at the output of the modulator. In the context of multi-tone signaling, as shown in (1.10), the gain and the phase imbalances result to incomplete suppression of the side band signal (the image signal). The terms around the frequencies $-h_k$ vanishes only when there is no phase or gain imbalance. The offset imbalance represents itself as a frequency component at the LO frequency, the last term of (1.10), which is also called as carrier feed-through (CF). However, another source of CF can be the LO-RF leakage of the mixers of the modulator.

Based on the (1.7) and (1.8) the LIF signals are generated so that the two extreme tones are equidistant from the origin, hence, in case of I/Q imbalance the image of one coincides and interferes with the other one. In order to avoid such a problem, the signals are frequency shifted by a factor γ, hence:

$$f_c = \gamma + \frac{f_1 + f_3}{2} \quad (1.11)$$

This frequency shift increases, slightly, the DAC sampling frequency but removes the interference from the tones. Figure 1.7 show the PSD of a simulated signal with a DC offset and different phase imbalances for each tone.

In the following section the implementation of the described method for different cases and applications will be presented.

1.5 Method Implementation and Experimental Results

In the previous sections, a method for multi-tone signal generation was presented. In this part, we focus on the generation of such signals. Moreover, Implementation considerations, characteristics and limitations will be discussed.

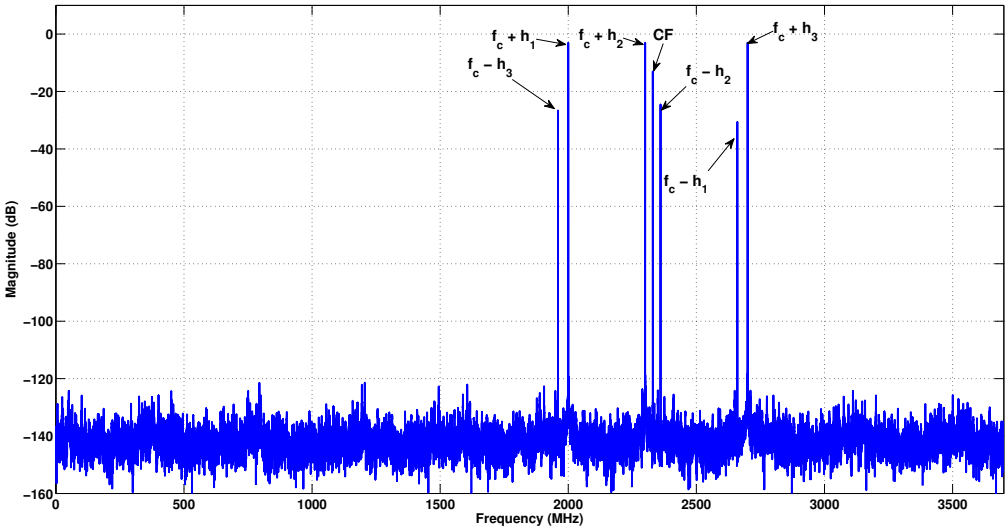

Figure 1.7: I/Q Imbalance effect on a three-tone signal with tones at 2.00 GHz, 2.3 GHz and 2.70 GHz with $\gamma = -20$ MHz. The images happen at 1.96 GHz, 2.36 GHz and 2.66 GHz and CF happens at 2.33 GHz (LO frequency).

1.5.1 Phase Continuity

One of the challenges of signal generation in the test environment is the phase continuity of the signal. The signal should not have any phase jump on its waveform. In test environment, signal is repeated when it ends, therefore, a phase discontinuity happens when the signal does not end where it begins. This phase discontinuity is observed as parasitic peaks and spectral regrowth on the signal. As shown in Figure 1.8(a) a three-tone signal does not end where it begins which results in the parasitic peaks and the spectral regrowth shown in Figure 1.8(b).

In order to make sure about the signal phase continuity, for periodic signals, the signal duration must be multiples of the signal period. In the case of multi-tone signaling the period of the signal is the least common multiple (LCM) of the period of each tone. For example, to have a three-tone signal with tones at 2.00 GHz, 2.03 GHz and 2.07 GHz, the LIF signals are generated at $h_1 = -25$ MHz, $h_2 = 5$ MHz, and $h_2 = 45$ MHz. Hence,

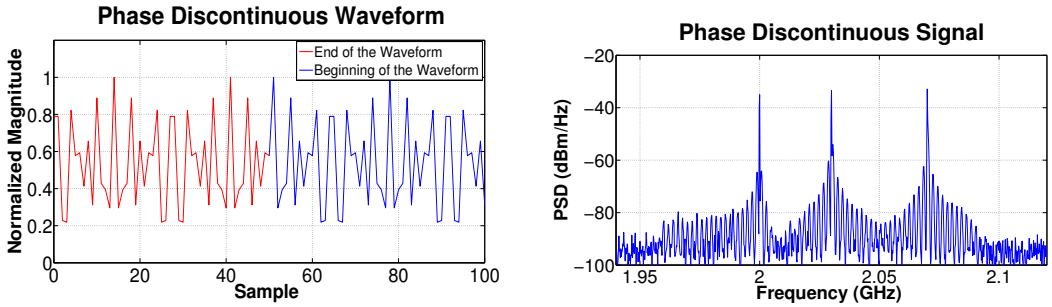

(a) (b)

Figure 1.8: Phase Discontinuity: (a) Time domain effect. (b) Frequency domain effect ($SFDR = 20dB$).

the period of the signal is the LCM of $1/h_1$,$1/h_2$,$1/h_3$ which is equal to 0.2 μs. As shown in Figure 1.9(a) the signal duration is a multiple of the period, which avoids any discontinuity. Moreover, Figure 1.9(b) corresponds to the PSD of the phase continuous signal which has no parasites or spectral regrowth

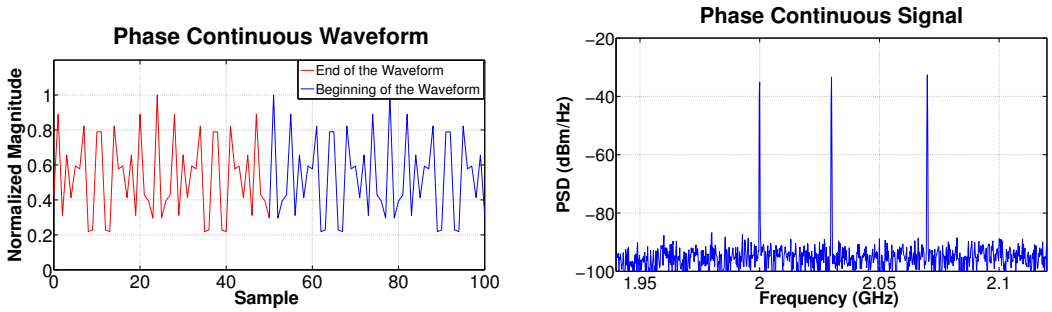

(a) (b)

Figure 1.9: Phase continuity: (a) Time domain effect. (b) Frequency domain effect ($SFDR = 55dB$).

1.5.2 Experimental Results and Application

Two practical cases were studied using which a three-tone and a four-tone signal are generated. In-phase and in-quadrature part of the signal (given in 1.4) are created by

MATLAB® and normalized data were loaded to Agilent EXG vector signal generator N5172B. The downloaded I/Q data were modulated using the I/Q modulator integrated in N5172B. The spectrums are depicted using the data obtained by the Rohde & Schwarz FSW spectrum and signal analyzer.

The maximum sampling rate of the N5172B DAC is 150 Ms/s which means that to create properly the signals, based on Nyquist criterion, the maximum baseband bandwidth is no more than half of DAC sampling rate 75 Ms/s. In other words, the highest LIF tone generated by our method will be at 75 MHz. In practice it is recommended to use an OSR higher than two, to ease the design of the post-DAC anti-aliasing filter [20].

Remark 1.2. In the proposed method, the tones are distributed over negative and positive frequencies, hence, the bandwidth of our signal can be nearly twice larger than the bandwidth given by Nyquist criterion!

Figure 1.10 shows the measured spectrum of the three tones as characterized in Table 1.2. The f_1 component is attenuated by a factor of 20 dB, with respect to others, to show the control over the amplitude of each tone. This control can be useful when the RF component carriers at the receiver does not have same power and the power difference can be compensated by the LO tones. Moreover, the control over the tones' amplitudes can control the gain of the mixers [21]. Comparing our method with tones distributed over negative and positive frequencies and the conventional method where all tones are generated at positive frequencies, we can notice that with an OSR of 3 and frequency separation of 70 MHz the conventional method requires $70 \times 3 = 210$ Ms/s but in our method we used sampling rate of 135 Ms/s ($h_3 \times 3 = 135$ Ms/s)

f_1	f_2	f_3	h_1	h_2	h_3	f_c	γ	*Sample Rate*
2.00 GHz	2.03 GHz	2.07 GHz	-25 MHz	5 MHz	45 MHz	2.025 GHz	10 MHz	135 Ms/s

Table 1.2: Three-tone intra-band CA signal characteristics

To show the higher degrees of this multi-tone signaling method, Figure 1.11 presents the PSD of a four-tone signal with the characteristics given in Table 1.3

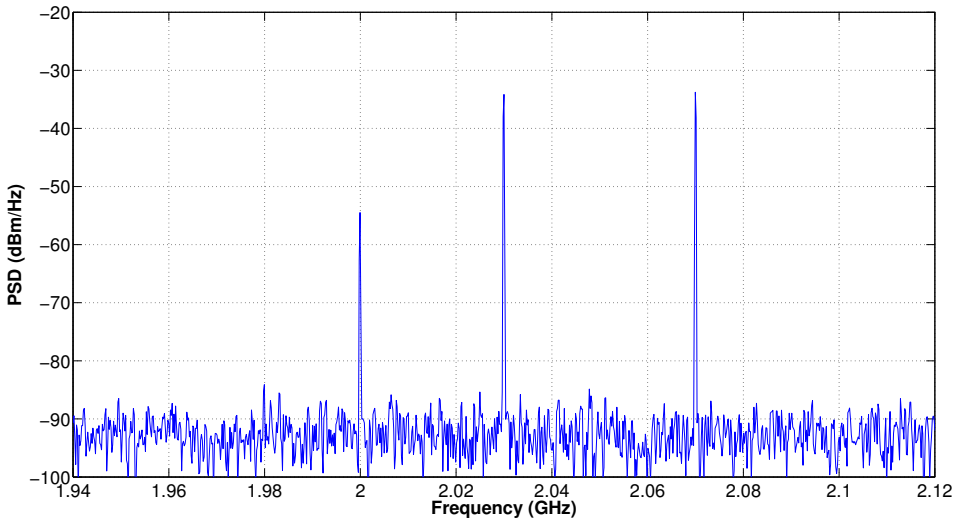

Figure 1.10: Measured PSD of a three-tone signal generated at 2.00 GHz, 2.03 GHz and 2.07 GHz with control over the amplitude of each tone (20 dB attenuation at 2.00 GHz).

f_1	f_2	f_3	f_4	h_1	h_2	h_3	h_4	f_c	γ	*Sample Rate*
2.00 GHz	2.02 GHz	2.05 GHz	2.07 GHz	-25 MHz	-5 MHz	25 MHz	45 MHz	2.025 GHz	10 MHz	135 Ms/s

Table 1.3: Four-tone intra-band CA signal characteristics

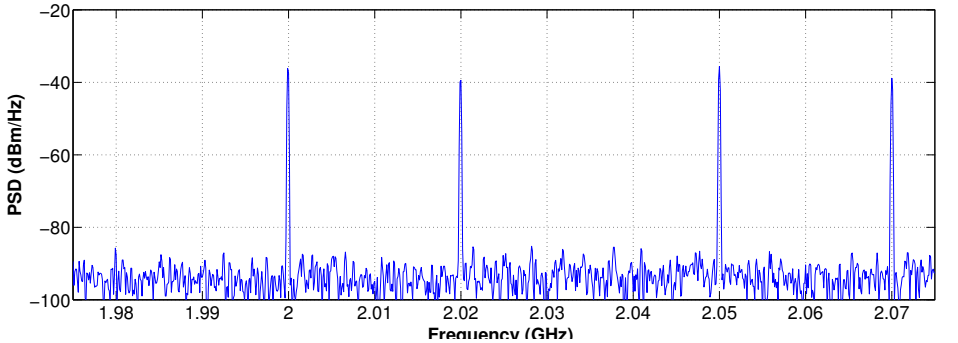

Figure 1.11: Four-tone signal generated at 2.00 GHz, 2.02 GHz, 2.05 GHz and 2.07 GHz.

The spectrums given in Figure (1.10), (1.11) show a clean, parasite-less signal. We observe an SFDR of 52 dB and 50 dB, respectively.

Now that we have seen how to generate such signals, let's try to apply them as local

oscillators for carrier aggregated receivers.

1.5.2.1 Multi-tone Signaling as LO in CA Receivers

There are many receivers that are designed and built for carrier aggregation and multi band communication purposes. In [22], a dual carrier aggregation receiver is proposed with a switched capacitor structure which makes the receiver front end operate as reconfigurable bandpass and notch filters. However, the receiver is designed for dual band applications and the distances between the component carriers are limited to slightly higher than 100 MHz. Moreover, it operates from 0.1 GHz to 1 GHz which makes it unsuitable fore LTE-A, since one of the operation band of LTE-A is around 2.5 GHz. Another receiver is proposed in [23], it uses N-path filters to enhance the frequency selectivity of the signal with the expense of using multiple identical receivers for component carriers. It follows the receiver structure of Figure 1.5(b). Another choice is the three-phase demodulator (TPD) receiver which is developed by the RF Laboratory of Télécom Paristech [24]. It is a super-heterodyne ultra-wideband (UWB) receiver based on 5-port technology. Basically, it down-converts N component carriers at LIF frequencies using N LOs. In this section, a brief analysis and example of how to down-convert the component carriers will be given. The analysis was proposed in [17] but some key points are re-stated here to help a better understanding of the multiple LO applications in receivers. RF component carriers can be shown as:

$$c_{RF}(t) = \sum_{k=1}^{N} Re\left[z_k(t)\, e^{i2\pi f_k t}\right] \tag{1.12}$$

where $c_{RF}(t)$, $z_k(t) = I_k(t) + jQ_k(t)$, N and f_k are carrier aggregated signal, complex envelope, number of component carriers and their corresponding frequencies, respectively. Each of these component carriers has a bandwidth of BW_k. On the other hand, the frequency of the local oscillators are chosen so that the component carriers are down-converted in a smaller band, called retrieval band B_r. The local oscillators are written as

$$x_{LO}(t) = \sum_{k=1}^{N} Re\left[V_{LO_k} e^{i2\pi(f_k - \Delta f_k)t}\right] \tag{1.13}$$

where $x_{LO}(t)$, V_{LO_k}, N and $f_k - \Delta f_k$ are the LO signals, their amplitude, total number of LOs and their frequencies, respectively. Using this combination of LOs, each component carrier is down-converted at its corresponding Δf_k. In order to avoid any overlap of the down-converted signals in B_r the following conditions must be met:

$$\begin{aligned} &\bullet \quad |f_d - f_q - f_{LO_k}| > B_r, \forall d \neq q \\ &\bullet \quad B_r \ll \textit{entire component carrier spectrum} \\ &\bullet \quad \Delta f_q > \Delta f_{q-1} + BW_{j-1}, 2 \leq q \leq N \end{aligned} \tag{1.14}$$

Once the conditions of (1.14) are met, by multiplying (mixing) (1.12) and (1.13) and applying a low-pass filter, the down-converted LIF signals are obtained:

$$\begin{aligned} V_{out} &= LPF\{c_{RF}(t)\, x_{LO}(t)\} \\ &= \sum_{k=1}^{N} V_{LO_k} z_k(t)\, cos(2\pi \Delta f_k t) \end{aligned} \tag{1.15}$$

The low pass filter should has a cutoff frequency of B_r. As an example, a 3-tone signal similar to Figure 1.9, with tones of 0 dBm output power, replaces the three LOs used in TPD receiver. The 3-tone signal is applied to the test bench depicted in Figure 1.12, as a LO signal. The 3-tone LO signal must down-convert the 3 QPSK modulated RF signals (yellow boxes), with bandwidths of 67.5 KHz at 2.8002 GHz, 2.8187 GHz and 2.8512 GHz to the baseband frequencies at 2.2 MHz, 2.7 MHz and 3.2 MHz, respectively, as shown in Figure 1.13. LIF signals are ready for sampling and further digital signal processing.

1.6 Conclusion

A multi-tone signaling method was proposed in this chapter which distributes the tones over positive and negative frequencies. This distribution reduces the highest frequency component value which results in reducing, significantly, the DAC sampling rate compared to the direct synthesizing methods. Furthermore, the amplitude of each tone is controllable which is very useful, since in practice, the received RF signals can be variable. The performance of the proposed method was shown by SFDR measurements, which were 52 dB and 50 dB for the cases 3-tone and 4-tone signals, respectively. Finally, an application of the proposed method was shown for a TPD receiver and the down-conversion procedure was discussed analytically. In the next chapter, this method will be developed to be used in RF transmitters as a frequency diversity and carrier aggregation solutions.

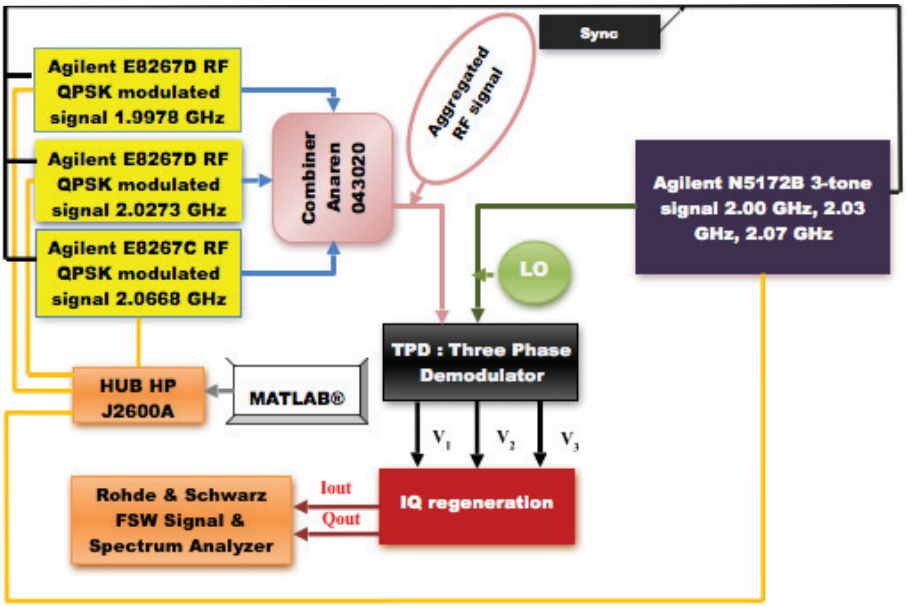

Figure 1.12: Carrier aggregation test bench: CA signals (yellow box) are received by the TPD (black box) and down-converted using the 3-tone signal (magenta box)

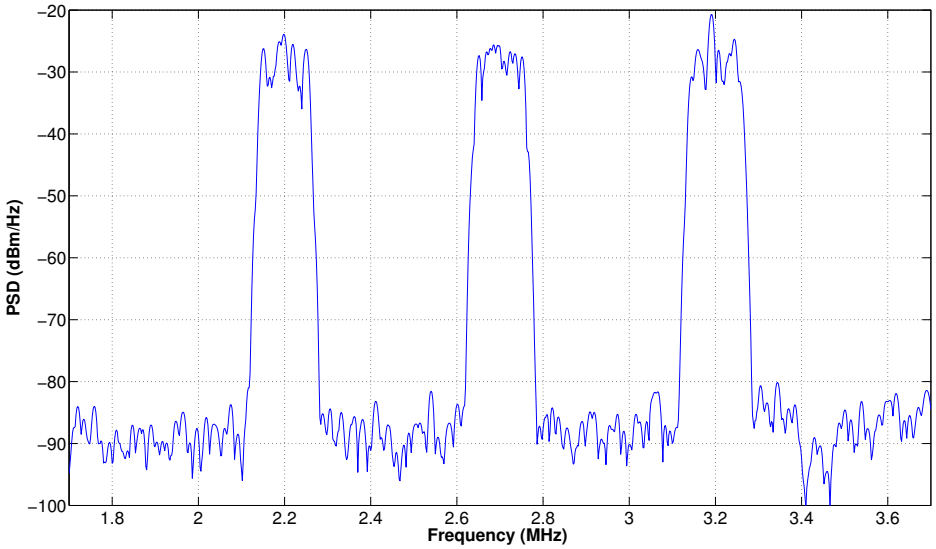

Figure 1.13: PSD of the down-converted component carriers

Chapter 2

Carrier Aggregation in LTE-A

Data consumption has exponentially grown up in mobile communications over the last two decades. First generation (1G) of the mobile phones was developed in 80s based on fully analog network. In 1991, the second generation (2G) or global system for mobile communications (GSM) was implemented based on a digital network. Voice call and short message service (SMS) were added to this generation. Two sub-generations of 2G, general packet radio service (GPRS) and enhanced data rates for GSM evolution (EDGE) introduced data transmission with a maximum data rate of 200 kbps. In early 2000s 3G was implemented as IMT-2000 standard of the International Telecommunications Union (ITU). It was based on wideband code division multiple access (WCDMA) mode. 3G led to two sub-generations which were high speed packet access (HSPA) and evolved HSPA (HSPA+) through which the data transmission rate increased to tens of Mbps. Furthermore, on December 2009, the fourth generation of mobile communications (known as LTE) was implemented in Finland [25] to obtain hundreds of Mbps of transmission rate. LTE and its sub-generation LTE-Advanced were standardized by 3rd Generation Partnership Project (3GPP) to answer the requirement of ITU in International Mobile Telecommunication-Advanced (IMT-Advanced).

2.1 Introduction

LTE-A is the next milestone in the evolution of LTE. It increases the data throughput to 1 Gbps on the down-link (DL) and 200 Mbps on the up-link (UL) because of multiple inputs multiple outputs (MIMO) structure and the CA added to LTE as release 10 of 3GPP [26]. LTE-A proposes a maximum DL data rate 10x higher than LTE and approximately 35x the download speed of HSPA+. Another improvement on LTE-A is its lower latency compared to preceding technologies, meaning that the delay between the click and download is reduced by more than 50%. Table 2.1 gives a summary of the performance of different technologies from 3G and 4G generations.

	WCDMA	**HSPA**	**HSPA+**	**LTE**	**LTE-A**
Max DL data rate	384 kbps	14.4 Mbps	28.8 Mbps	100Mbps	1.0 Gbps
Max UL data rate	128 kbps	5.7 Mbps	11 Mbps	50 Mbps	200 Mbps
Implemented DL data rate	100 kbps	500 kbps	1.5 Mbps	7 Mbps	14-21 Mbps
Latency	150 ms	100 ms	50 ms	10-15 ms	5 ms
3GPP Release	Rel 1999/4	Rel 5/6	Rel 7	Rel 8	Rel 10

Table 2.1: Performance evaluation of mobile technologies.

Several modulation schemes with different orders such as 4-quadrature amplitude modulation (QAM), 16-QAM, 64-QAM, etc. are utilized in LTE-A depending on the channel situations and available resources. The low order schemes (4-QAM), are preferred in low signal to noise ratio (SNR) conditions because the symbols on the constellation are more distant and decision making is easier. On the other hand, when SNR is high, the symbol detection problem is less, hence, data rate and spectral efficiency can be increased using higher order schemes (128-QAM). These data are accessed using orthogonal frequency division multiple-access (OFDMA) and single carrier FDMA (SC-FDMA) methods, in DL and UL transmissions, respectively . OFDMA is chosen for its robustness against inter symbol interference (ISI). Besides, OFDMA has a high peak to average power ratio (PAPR) which makes the power amplifier (PA) consumption very

high, hence SC-FDMA is used on UL, which has a lower PAPR, to relax the battery requirements of the user [27] [28]. Both access methods are based on the basic OFDM with small modifications. In OFDMA access mode, each subcarrier is modulated by different relatively long symbols, in contrast to SC-FDMA where all subcarriers are modulated by a symbol (where the term single carrier comes from, in Figure 2.1 all the subcarriers of SC-FDMA have the same color for a short time) with a relatively short duration, as shown in Figure 2.1. 3GPP proposed several bands for LTE-A service providers which

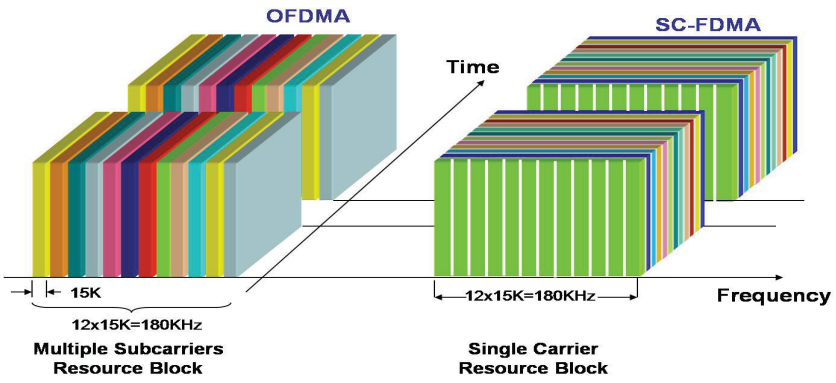

Figure 2.1: OFDMA: Different long symbols on each subcarrier. SC-FDMA: Identical short symbol on all the subcarriers . Courtesy of www.exploregate.com .

are given in Table 2.2 [29]. In France, The French authorities [in French: *Autorité de Régulation des Communications électroniques et des Postes*(ARCEP)] attributed the LTE-A bands to mobile operators as depicted in Figure 2.2 [30][31][32][33][34][35][36]. Carrier aggregation principle of LTE-A was explained in the previous chapter, therefore in the next section, a brief explanation of MIMO in LTE-A is given.

2.1.1 Multiple Inputs Multiple Outputs (MIMO)

MIMO structure exploits the spatial characteristics of the propagation medium to increase the throughput and the reliability. In the spatial multiplexing scenario, data are sent through different streams over different antennas. Moreover, the antennas radiation

Operating Band	Uplink Band	Downlink Band	Duplex Mode
	Low - High	Low - High	
1	1920 MHz - 1980 MHz	2110 MHz - 2170 MHz	FDD
2	1850 MHz - 1910 MHz	1930 MHz - 1990 MHz	FDD
3	1710 MHz - 1785 MHz	1805 MHz - 1880 MHz	FDD
4	1710 MHz - 1755 MHz	2110 MHz - 2155 MHz	FDD
5	824 MHz - 849 MHz	869 MHz - 894 MHz	FDD
6	830 MHz - 840 MHz	865 MHz - 875 MHz	FDD
7	2500 MHz - 2570 MHz	2620 MHz - 2690 MHz	FDD
8	880 MHz - 915 MHz	925 MHz - 960 MHz	FDD
9	1749.9 MHz - 1784.9 MHz	1844.9 MHz - 1879.9 MHz	FDD
10	1710 MHz - 1770 MHz	2110 MHz - 2170 MHz	FDD
11	1427.9 MHz - 1447.9 MHz	1475.9 MHz - 1495.9 MHz	FDD
12	698 MHz - 716 MHz	728 MHz - 746 MHz	FDD
13	777 MHz - 787 MHz	746 MHz - 766 MHz	FDD
14	788 MHz - 798 MHz	758 MHz - 768 MHz	FDD
15	Reserved	Reserved	-
16	Reserved	Reserved	-
17	704 MHz - 716 MHz	734 MHz - 746 MHz	FDD
18	815 MHz - 830 MHz	860 MHz - 875 MHz	FDD
19	830 MHz - 845 MHz	875 MHz - 890 MHz	FDD
20	832 MHz - 862 MHz	791 MHz - 821 MHz	FDD
21	1447.9 MHz - 1462.9 MHz	1495.9 MHz - 1510.9 MHz	FDD
22	3410 MHz - 3500 MHz	3510 MHz - 3600 MHz	FDD
...			
33	1900 MHz - 1920 MHz	1900 MHz - 1920 MHz	TDD
34	2010 MHz - 2025 MHz	2010 MHz - 2025 MHz	TDD
35	1850 MHz - 1910 MHz	1850 MHz - 1910 MHz	TDD
36	1930 MHz - 1990 MHz	1930 MHz - 1990 MHz	TDD
37	1910 MHz - 1930 MHz	1910 MHz - 1930 MHz	TDD
38	2570 MHz - 2620 MHz	2570 MHz - 2620 MHz	TDD
39	1880 MHz - 1920 MHz	1880 MHz - 1920 MHz	TDD
40	2300 MHz - 2400 MHz	2300 MHz - 2400 MHz	TDD
41	3400 MHz - 3600 MHz	3400 MHz - 3600 MHz	TDD

Table 2.2: LTE/LTE-A bands proposed by 3GPP.

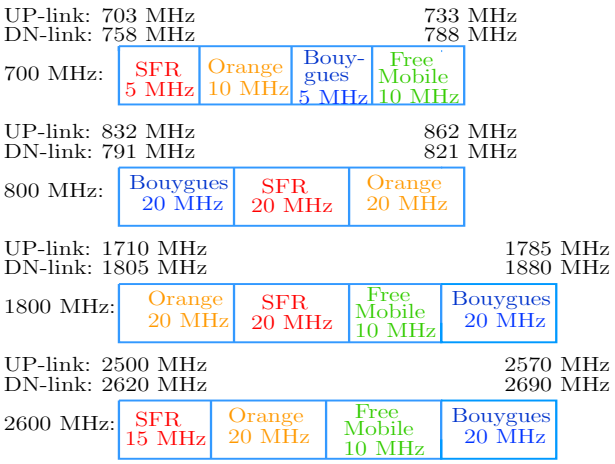

Figure 2.2: LTE/LTE-A allocated frequency bands to service providers in France

patterns are controlled by phase shifting the signals of different antennas of the array. This method is called beam-forming which allows us to radiate and receive in a high interference medium using a very directive beam pointing at the user [37]. Beamforming and spatial multiplexing of MIMO increase spectral efficiency, average cell performance and edge cell performance. LTE-A uses multiple-user MIMO that gives the freedom to multiple users to use the same channel. It follows a transparent policy in which different users are unaware of the frequency-time resource allocation of other users [38]. MIMO structures have many advantages and few drawbacks. They have higher data rate, higher network coverage and more robustness with respect to single input single output (SISO) structures. On the other hand, the use of multiple antennas requires miniaturized antennas, to be suitable for mobile applications. Another issue can be the overall cost, since many antennas and high calculation power are required in this structure, fortunately, the production cost reduces significantly, on mass production. Also, power consumption is a great deal in MIMO based mobile systems since many antennas and stronger CPUs are needed. An idea to mitigate this problem is to use a SISO structure when the mobile device is on standby and a MIMO structure when the device receives the "wake-up" signal [39]. LTE-A has up to 8×8 MIMO structure in DL and a 4×4 structure in UL as shown in Figure 2.3[40].

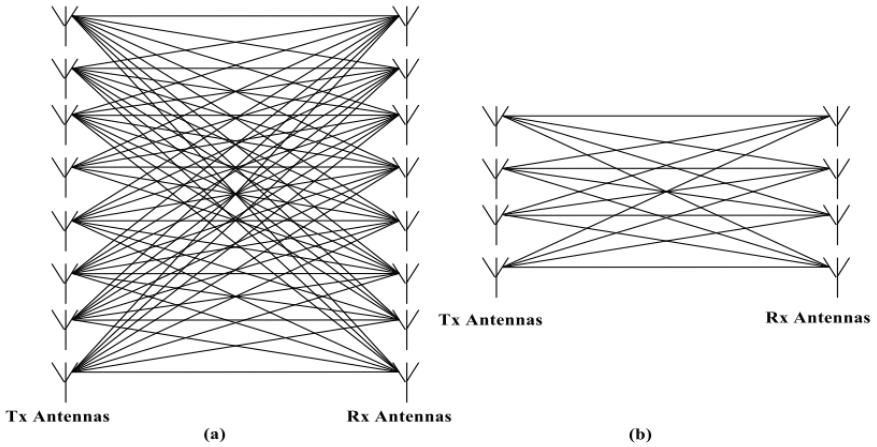

Figure 2.3: LTE MIMO structures: (a) 8×8 configuration in DL. (b) 4×4 configuration in UL.

Now that we have a general information about LTE-A, we need to focus on the generation, transmission and reception of such signals. In the following sections, firstly, OFDM principle, its generation, as well as its applications and imperfections will be discussed. Secondly, a method for signal generation as a frequency diversity solution is proposed. Thirdly, OFDM based carrier aggregated signal generation is proposed. In the 4th section, the special demodulation process at the receiver will be explained. Moreover, experimental results of the frequency diversity method and OFDM based carrier aggregated method will be given in section 5. Finally, the conclusion will be given in the last section of this chapter.

2.2 Inter Symbol Interference (ISI)

In high data rate communications, the propagation channel plays a significant role. The channels may have variations in time domain or in frequency domain. These variations can be fast or slow depending on the propagating signal. For any channel, the period of time at which the impulse response of the channel is invariant is called, the coherence time (t_c). In a system where the baseband symbol duration is less than the coherence time, the symbols are uncorrelated. On the other hand, the objects within the propagation

medium between the transmitter and the receiver can reflect copies of the signal to the receiver. These reflection effects are called, multi-path effect. These reflections, as well as, the channel physical characteristics can generate fading effect on the signal. If the symbol duration (T) is higher than the coherence time of the channel, fast fading occurs. Frequency domain speaking, there is a time difference between the first and the last arriving signal from different paths which is called delay spread (D). Delay spread is inversely proportional to coherence bandwidth (BW_c) that shows the channel bandwidth at which the channel is relatively invariant (flat fading). On the other hand, if the signal bandwidth (BW) is higher than the coherence bandwidth, selective fading happens. To recapitulate:

$$\begin{aligned} BW < BW_c &\Rightarrow flat\ fading \\ BW > BW_c &\Rightarrow selective\ fading \end{aligned} \tag{2.1}$$

Selective fading results in ISI. It happens when the symbol duration is not relatively long with respect to the channel delay spread. There are many methods to overcome ISI. The first one gives the optimal performance which is called Viterbi algorithm. This algorithm is a block decoding algorithm to reduce the complexity of a maximum likelihood (ML) decoding. Lets $x\,(n)$, $y\,(n)$ be the the transmitted and received symbols. Hence, a block of them are used to perform the decoding:

$$\boldsymbol{x} : [x\,(0)\,, ..., x\,(N)]^T$$
$$\boldsymbol{y} : [y\,(0)\,, ..., y\,(N)]^T$$

the ML decoding is to minimize quadratic difference equation between the received symbol and the ideal one as follows:

$$[\hat{x}\,(0)\,, ..., \hat{x}\,(N)] = arg \quad min \sum_{n=0}^{N} |y(n) - \sum_{l=0}^{L} h(l)s(l-n)|^2 \tag{2.2}$$

Where $h(n)$ and $s(n)$ are the channel model filter and transmitted signal, respectively. Viterbi defined a cost function and a trellis structure to determine the least costly path in a recursive way.

$$C_N(\boldsymbol{x}^{(N)}) = C_{N-1}(\boldsymbol{x}^{(N-1)} + \Delta C(x(N)) \tag{2.3}$$

with

$$\Delta C(x(N)) = |y(N) - \sum_{l=0}^{L} h(l)s_{N-l}|^2$$

where $C_N(\boldsymbol{x}^{(N)})$ is the cost vector. Detailed explanation and examples are given in [41]. Viterbi algorithm complexity increases linearly with the time instances (n), polynomialy with modulation order and exponentially with L [42]. When the data rate increases, the Viterbi complexity does not make it a good choice. Hence, other sub-optimal solutions must be considered. Another solution is to cancel out the ISI effects at the receiver by using linear and nonlinear equalizers such as zero-forcing (ZF) equalizer, minimum mean squared error (MMSE) equalizer and decision-feedback equalizer (DFE) (nonlinear) [43]. ZF equalization consists of applying the inverse of the channel model to remove its effects. Its application is simple, but increases the noise of the signal due to the fact that theoretically ZF model has infinite taps, but a finite length of it is applied. MMSE equalization performance in high SNR equalization regime is similar to ZF, but in low SNR regime, it is similar to adaptive filters. DFE is based on ZF equalization scheme where a feedback is added after the ZF structure [44]. The feedback induces some delays to take into account the taps that were excluded in ZF equalization. Hence, it has a good performance and the noise enhancement is much better than ZF, but the complexity is increased. Another method to overcome ISI is OFDM which is proposed in LTE-A.

2.3 Orthogonal Frequency Division Multiplexing (OFDM)

As stated earlier, when the signal bandwidth is larger than the coherence bandwidth, selective fading happens. A multi-carrier signal with narrow bandwidths at each carrier (also known as subcarrier) can replace the single wide-band signal, hence the channel behaves as a flat channel for each of the subcarriers, as shown in Figure 2.4. On the other hand, the channel equalization is simpler for a narrow-band subcarrier in a flat channel rather than a wide-band signal in a frequency selective channel[45].

The subcarriers need to be orthogonal and to ensure that there will not be any Inter Carrier Interference (ICI) between them.

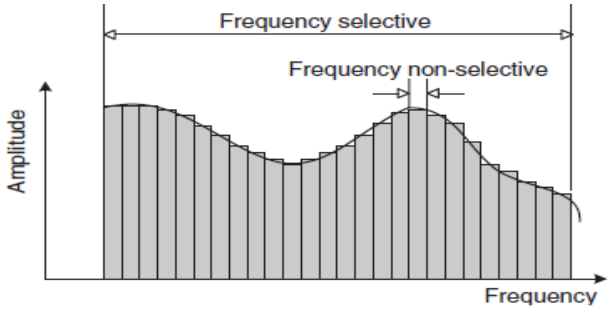

Figure 2.4: Multicarrier frequency response

2.3.1 Orthogonality

Two signals are said to be orthogonal when the integral of their product over a period is null. A subcarrier among N subcarriers is represented by: $e^{j2\pi f_k t} \quad for \quad k = \{1, ..., N\}$ where $f_k = \dfrac{k}{T}$ is the frequency of each subcarrier. In discrete time, the signal is sampled at Ts meaning $t = nT_s = nT/N$ for $n = 0, ..., N-1$. Let's see if these signals are orthogonal or not:

$$\begin{aligned} \frac{1}{N}\sum_{0}^{N-1} e^{j2\pi\frac{k}{T}\frac{nT}{N}} e^{-j2\pi\frac{l}{T}\frac{nT}{N}} &= \frac{1}{N}\sum_{0}^{N-1} e^{j2\pi\frac{k-l}{N}n} \\ &= \begin{cases} 1 & for \; \forall \; integer \; k = l \\ 0 & otherwise \end{cases} \end{aligned} \tag{2.4}$$

To ensure an ICI-free transmission, this condition must be fulfilled.

2.3.2 OFDM Modulation

The Idea is to use multicarriers with shorter bandwidths (longer symbol durations). Imagine symbol $X_q(k)$ is the q^{th} symbol among an infinite number of symbols transmitted on the k^{th} subcarrier ($k = 1, ..., N$). These symbols pass through a serial-to-parallel step to be transmitted over N subcarriers. The overall duration of the symbol becomes $T + NT_s$. An OFDM baseband signal can be written as:

$$x_q(t) = \sum_{q=0}^{\infty}\sum_{k=0}^{N-1} X_q(k) e^{j2\pi f_k (t - qT)} \tag{2.5}$$

Where $e^{j2\pi f_k(t-qT)}$ represents the k^{th} OFDM symbol transmitting q^{th} symbol. In discrete-time (2.5) is sampled at $t = qT + nT_s$ and $f_k = k/T$, hence it becomes:

$$x_q(n) = \sum_{k=0}^{N-1} X_q(k) e^{j2\pi k \frac{n}{N}} \quad for\ n = 0, ..., N-1 \tag{2.6}$$

This is known as the N-point inverse discrete fourier transform (IDFT) and it can be calculated in digital signal processing via inverse-FFT (IFFT) algorithm. Now that we have an OFDM symbol, lets try to demodulate it.

2.3.3 OFDM Demodulation

Let's imagine the baseband OFDM signal given in (2.6). At the receiver, the signal can be written as:

$$y_q(n) = \sum_{k=0}^{N-1} X_q(k) e^{j2\pi k \frac{n}{N}} \quad for\ n = 0, ..., N-1$$

Its frequency domain Fourier transform counter part becomes:

$$\begin{aligned} Y_q(k) &= \sum_{n=0}^{N-1} y_q(n) e^{-j2\pi k \frac{n}{N}} \\ &= \sum_{n=0}^{N-1} \left\{ \frac{1}{N} \sum_{l=0}^{N-1} X_q[l] e^{j2\pi l \frac{n}{N}} \right\} e^{-j2\pi k \frac{n}{N}} \\ &= \sum_{n=0}^{N-1} \sum_{l=0}^{N-1} \frac{1}{N} X_q[l] e^{j2\pi (l-k) \frac{n}{N}} = X_q[k] \end{aligned} \tag{2.7}$$

The last part of (2.7) is only valid if the subcarriers are orthogonal as shown in (2.4). In (2.7), a discrete Fourier transform (DFT) was applied which can be computed using FFT algorithm. ISI occurs due to frequency selective fading of the channel. It is prevented by OFDM structure where narrow band subcarriers are used. On the other hand, to overcome ISI caused by the multi-path effect, we need to modify the OFDM structure to make this source of ISI ineffective, which is explained in the next section.

2.3.4 Cyclic Prefix (CP)

Due to the Multi-path effect of the channels, some symbols arrive at different instants. Hence, symbols face interference as depicted in Figure 2.5. To overcome this problem, a

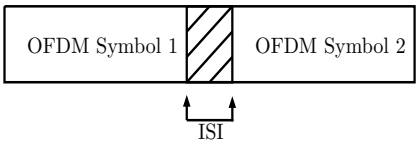

Figure 2.5: ISI between two OFDM symbols

guard interval is used between each two OFDM symbols. To avoid ISI the length of the guard band (L) must be longer than the channel delay spread. The guard interval does not carry any useful data which reduces the spectral efficiency. There are two types of guard bands:

- Zero Padding (ZP)
- Cyclic Prefix (CP)

Zero padding fills the guard band with zeros. Its disadvantage is power variation in the OFDM symbol between the zero-padded part and the useful data. On the other hand, CP is a good choice to implement. Basically, L symbols are taken from the end of OFDM symbol and added to the beginning. Since CP contains the same symbols as OFDM symbol, it does not make the power variation as in ZP. Figure 2.6 shows the structure of the OFDM symbol with CP. As it is shown (in red) the delay spread is shorter than the CP length, hence the ISI does not disturb the useful part of the OFDM symbols. Now

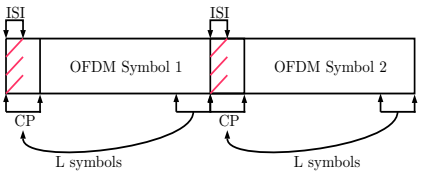

Figure 2.6: OFDM symbols with CP: robust against ISI

that the main body of the OFDM transmission is explained, we need to see its generation with practical considerations.

2.3.5 OFDM Signal Generation

OFDM signal needs to be adapted to transmission, therefore couple of steps must be added to the general OFDM modulation. Firstly, a synchronization procedure needs to be applied to ensure frequency and time synchronization. Basically, transmitters and receivers have different time and frequency references which cause symbol timing offset (STO), and carrier frequency offset (CFO), respectively. STO represents itself in symbol constellation as symbols going away from their original position as shown in Figure 5.(b) in [46] which is depicted here as Figure 2.7(a). CFO represents a phase rotation in the symbol constellation, since the frequency offset induces an additional phase ($2\pi f_{cfo}t$) as shown in Figure 2.7(b).

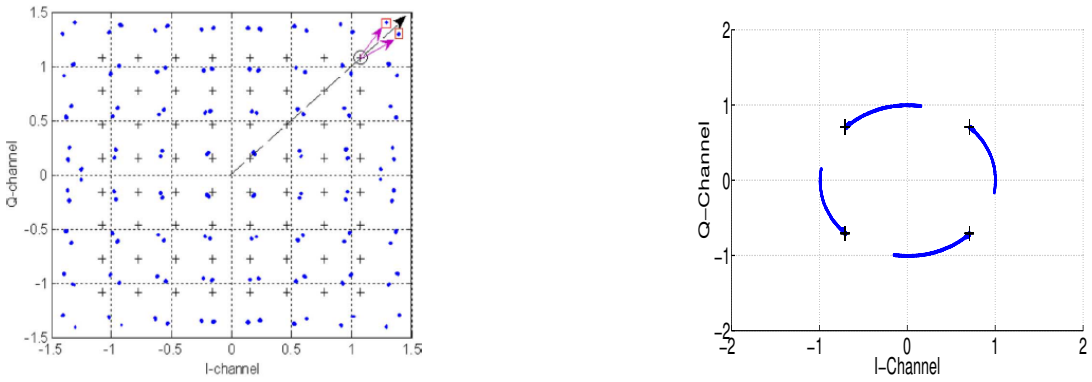

(a) (b)

Figure 2.7: (a) STO effect on the signal constellation: symbols (blue dots) going away from the ideal positions (black crosses). (b) CFO Effect on the constellation: symbols (blue dots) rotate around the constellation center from their ideal positions (black crosses).

There are three main synchronization methods:

- CP Synchronization
- Pilot Tone Synchronization

- Training Sequence (TS) Synchronization

CP synchronization uses the fact that CP is a copy of a part of the OFDM symbol and by correlating these two parts the STO and CFO can be estimated [47][48]. This method is well suited for fast varying channels, because at each OFDM symbol synchronization it can be updated, however it is sensitive to noise and ISI. The ISI corrupts CP and the correlation does not yield to good estimation.

Pilot tone synchronization method uses some of the subcarriers as tones which are separated depending on the channel overhead and the coherence bandwidth of the channel. In [49], a pilot based synchronization method is proposed where the synchronization is made at the down-link and the synchronized reference time is used for the up-link. Moreover, in [50], pilot tones are used in every OFDM symbol and CFO is estimated in two steps ; acquisition and tracking mode where the large CFO is estimated in the first step and fine CFO is estimated in second one. Then, they are added to make the complete estimation of the CFO.

TS synchronization uses two identical predefined OFDM symbols which are transmitted consecutively. In [51], the first half of each TS OFDM symbol is identical to its second half. STO is estimated by using an MMSE algorithm between the ideal TS and the received symbols . Moreover, CFO is estimated by finding the phase difference between the two identical halves. If CFO is larger than π, then the second OFDM symbols is used to find the precise OFDM symbol. In another work, [52] proposes a method which is based on the same principle of a TS with two identical halves which are constituted of constant amplitude zero auto correlation (CAZAC) that are weighed by a pseudo random sequence. The weighted CAZAC TS helps to increase the precision of the correlation function between the received symbols and the TS, which leads to a better estimation of STO.

In a part of this work, a hybrid method was used to ensure the feasibility of CFO estimation in our communication system. It consists of using two identical CAZAC sequences transmitted as the first and the second OFDM symbols, as shown in Figure 2.8. Since the two TS are identical, CFO shows itself as a phase change between the

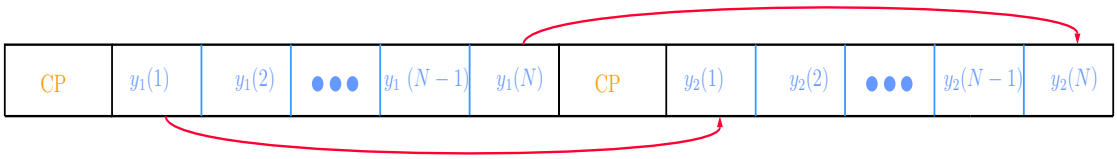

Figure 2.8: ISI between two OFDM symbols

symbols of the subcarriers as shown in (2.9).

$$y_2(k) = y_1(k)e^{j2\pi f_{CFO}\Delta T} \quad for\ k = 1, ..., N \tag{2.8}$$

where $y_1(k)$, $y_2(k)$, f_{CFO}, ΔT are the first and the second TS, CFO and the correponding time difference between the two subcarrier symbols ($\Delta T = (N + L)T$). Therefore, by multiplying the subcarrier symbols of the second TS to the conjugate of the first TS, an estimation of the CFO is obtainable:

$$y_2(k)y_1^*(k) = |y_1(k)|^2 e^{j2\pi f_{CFO}\Delta T} \quad for\ k = 1, ..., N \tag{2.9}$$

Extend it over all of the subcarrier symbols, yields to the CFO estimation:

$$f_{CFO} = \frac{1}{2\pi\Delta T} arg\left(\sum_{k=1}^{N} y_2(k)y_1^*(k)\right) \tag{2.10}$$

CFO estimation was applied to a practical OFDM signal with 32 subcarriers ($N = 32$) with a CP of length 8 ($L = 8$) for a QPSK signal. The received signal constellation was shown in Figure 2.7(b). CFO of the measured signal was estimated using (2.10) about 69 Hz. The compensated constellation of the received symbols is shown in Figure 2.9.

On the other hand, in test environment transmitters and receivers time reference can be synchronized using a 10 MHz clock signal that is generated, in our case, by one of the signal generators (as master) and is followed by other devices (as slaves). This avoids the CFO problem, but STO can still be a challenge. The detection of the first symbol of the transmitted signal is explained in section 2.6.1. In LTE the OFDM modulation has a DC null carrier meaning that the middle subcarrier is set to zero and does not transmit anything. This is proposed directly in Figure 5.4.2-1 of ESTI TS.36.101 [53]

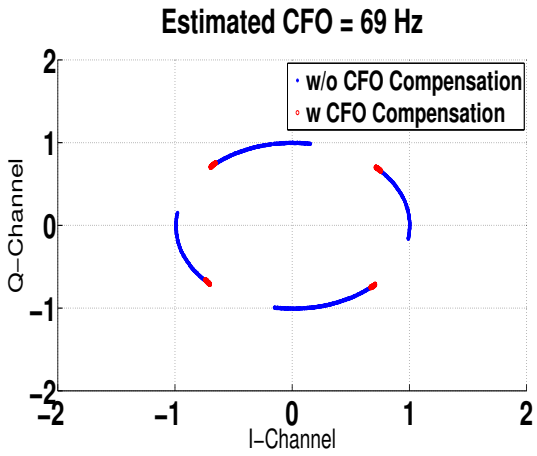

Figure 2.9: CFO compensation using the hybrid method

and indirectly in the section 6.12 TS.36.211 [26], where the OFDM baseband symbol formula is given without a subcarrier zero.

In short, the OFDM signal is generated as shown in Figure 2.10 (a). First, the symbols with different or similar modulation types (QPSK, 16QAM,...) are generated. Second, they are passed through a serial to parallel step. Third, the IFFT process of length N is applied to attribute each symbol to its corresponding subcarrier. Fourth, the symbols are put in series. Fifth, CP is added to avoid ISI. Sixth, pulse shaping filter is applied to the OFDM signal to enhance the spectral properties. Then, the signal is modulated over a carrier and amplified with a PA to be transmitted through an antenna in the medium. At the receiver, as shown in Figure 2.10 (b) the signal passes through a low noise amplifier (LNA). Next, the signal baseband component of the signal is extracted, then, a pulse shaping filter is applied to remove its effect at the transmitter. In the next step, the CP is removed and the symbols are put in parallel to apply the FFT process. Finally the demodulated symbols are put in series.

In the next section, we will try to use carrier aggregation with identicals OFDM symbols as a frequency diversity solution.

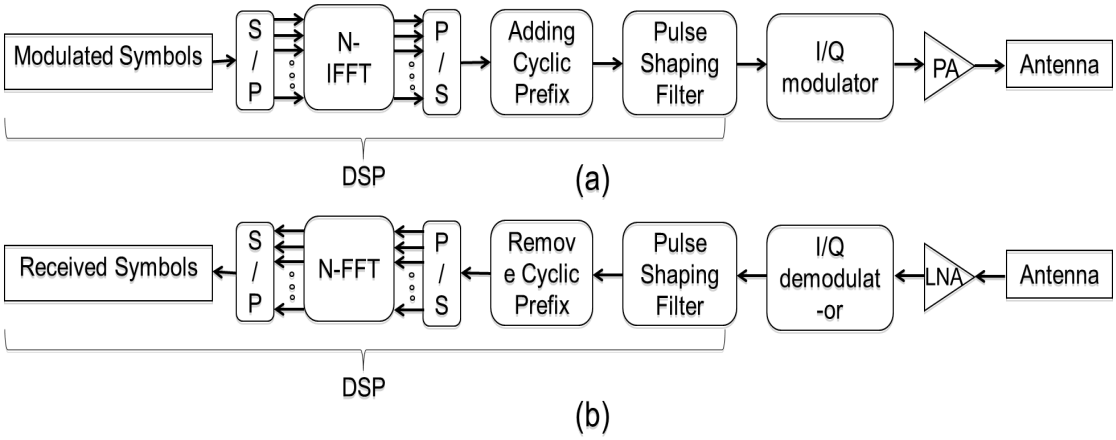

Figure 2.10: OFDM:(a) trasmission . (b) reception

2.4 Frequency Diversity With QPSK-OFDM Carrier Aggregation Using a Single Transmission Chain

Several architectures for CA have been proposed in literature, in [54], three transmitter architectures are mentioned. Two of the architectures consist of having a transmitter chain by frequency band. The third one supposed to generate two frequency bands, by one transmission chain, which is suitable for continuous band CA. In another approach, a method based on zero padding between symbols is used to generate signals at two frequency bands, which requires a long FFT when frequency bands are far from each other [55]. Moreover, a direct baseband to RF synthesis method for generation of ten component carriers is proposed in [56], where a different DAC structure is used. Instead of coding the amplitude of the signal, the slope of the signal is coded into N bits. Using this method, the bit length of the DAC is reduced, but the sampling rate is still high. They show an SFDR of 33 dB using a 3-bit DAC and a sampling frequency of 25 GHz. Kaissoine *et al.* use a CA method, based on using a transmitter chain per frequency band, for more than two frequency bands dedicated to modulation and demodulation of QPSK modulated signals. In other words, in order to have three frequency aggregated bands, Kaissoine *et al.* use three RF transmitters and three Local Oscillators (LO) for

a complete modulation and demodulation process [17]. This equipment design increases the energy consumption and the production cost of the system. This section presents the frequency diversity that can be used in CA communication using a single transmission chain which consists of one I/Q modulator, one DAC, one power amplifier, etc.

2.4.1 QPSK-OFDM Carrier Aggregation

Carrier aggregation can also be used as a frequency diversity solution. The signals are transmitted over frequency bands which can ensure the proper transmissions where the communication reliability is critical. The proposed CA method is applicable to all three modes of CA (Contiguous, non-contiguous intra-band and non-contiguous inter-band) depending on the transmission equipment that are used. One can generate several CW signals using the method we proposed in [57]. Hence, the three-tone signal is written as:

$$\begin{aligned} x(t) &= e^{i2\pi f_1} + e^{i2\pi f_2} + e^{i2\pi f_3} \qquad where\ f_1 < f_2 < f_3 \\ &= \left(I_3(t) + jQ_3(t)\right) e^{2\pi f_c t} \\ &= \left(1 + 2\cos\left(2\pi\frac{f_1 - f_2}{2}t\right)\right)\cos\left(2\pi\frac{f_1 + f_2 - 2f_3}{4}t\right) \\ &+ j\left(-1 + 2\cos\left(2\pi\frac{f_1 - f_2}{2}t\right)\right)\sin\left(2\pi\frac{f_1 + f_2 - 2f_3}{4}t\right) e^{i2\pi\frac{f_1+f_2+2f_3}{4}t} \end{aligned} \tag{2.11}$$

where $I_3(t)$, $Q_3(t)$ are the in-phase, in-quadrature component of the 3-tone signal, respectively, and f_c is the frequency of the carrier signal. This configuration of I(t) and Q(t) is less optimal than the one proposed in the previous chapter in the sense that the DAC sampling rate is higher, since the LIF components are not distributed in a symmetrical manner. Nevertheless, it is described as stated in our work presented at IMS2015 conference [58].

By modulating the CW signals with the OFDM signal presented in 2.3.2 CA is achievable. The baseband form of the overall signal can be written as:

$$I(t) + jQ(t) = \left(I_{OFDM}(t) + jQ_{OFDM}(t)\right)\left(\left(I_3(t) + jQ_3(t)\right)\right) \tag{2.12}$$

where $I_{OFDM}(t)$, $Q_{OFDM}(t)$ are the in-phase and in-quadrature component of (2.6).

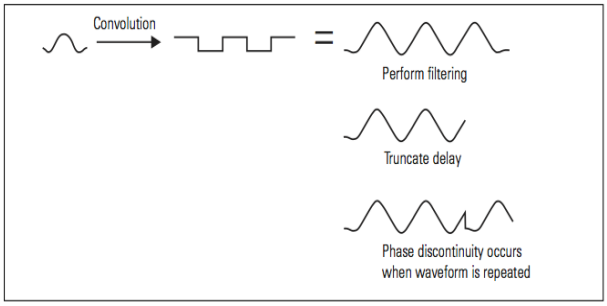

(a)

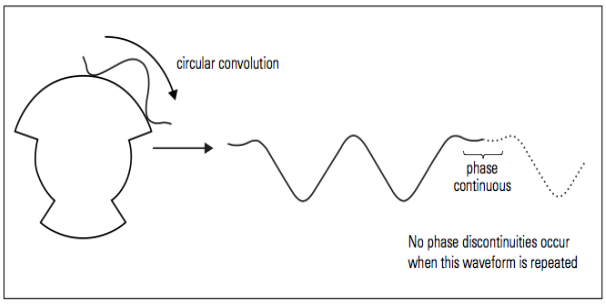

(b)

Figure 2.11: Phase Discontinuity: (a) normal convolution. (b) circular convolution

Here the same OFDM symbol is modulated over three component carriers which can be used as a frequency diversity solution. Moreover, in this case, no control over the amplitude of the component carriers is proposed.

There are couple of modifications and remarks that need to be taken into account here. Firstly, the periodicity of the multi-tone signal is broken since they are modulated in OFDM, meaning that the signal length does not need to be an integer duration of the period to avoid phase discontinuity. Here, the phase discontinuity is avoidable by using the pulse shaping filters which make the gradual transition between the last sample and the first sample of the signal feasible. This transition happens swiftly, if a circular convolution is applied when filtering instead of a regular convolution [59]. It removes the filter delay which may cause phase discontinuity, as presented in Figure 2.11(a). The circular convolution process is shown in Figure 2.11(b). Secondly, the TS used in these CA signals is based on the TS proposed in [51]. It consists of a TS with two identical

halves, where QPSK symbols are transmitted over odd numbered subcarriers and zeros are transmitted over even numbered subcarriers as shown in Table 2.3 for a case with 9 subcarriers. This TS does not have the constant amplitude property of CAZAC but is easily detectable from other data, since non-zeros symbols are transmitted on even subcarriers of the data.

Subcarrier Number	**Training Sequence**
1	-0.707 -i 0.707
2	0
3	-0.707 +i 0.707
4	0
5	0.707 +i 0.707
6	0
7	-0.707 +i 0.707
8	0
9	-0.707 -i 0.707

Table 2.3: Training sequence illustration

Thirdly, the sampling rate of the CA signal is higher than the OFDM signal, hence the OFDM signal must be oversampled to have the same sampling rate for both of them.

$$R_{CA} = OSR * R_{OFDM} \tag{2.13}$$

where $R_{multi-tone}$ and R_{OFDM} are the sampling rate of the multi-tone and OFDM signal, respectively. OSR is the oversampling ratio.

The method was implemented using the Agilent N5172B AWG where the baseband signal of (2.12) is generated via MATLAB® [1] and sent to the AWG over a local area network (LAN) connection. A QPSK-OFDM signal with 32 subcarriers ($N = 32$) and a CP length of 8 ($L = 8$) with a symbol rate of 1 MS/s, and filtered by a root raised cosine

[1] the signal Generation program is on Appendix I

filter with a roll-off factor (α) of 0.35 (the overall signal bandwidth becomes 1.35 MHz) and modulated over component carriers generated by (2.11) at 2.8, 2.82 and 2.86 GHz. The DAC sampling rate (f_{DAC}) is chosen so that it is higher than the twice the difference between the highest and the lowest component carrier ($f_{DAC}>$ 2 (2.86 GHz - 2.8 GHz) = 120 MHz). Hence, sampling rate 120.15 Ms/s is a suitable choice which makes an OSR of 89 for the OFDM signal. The spectrum of the three identical CA signals are shown in Figure 2.12, where the SFDR is about 35 dB and is limited by the noise floor of spectrum analyzer. There is an anomaly on the component carrier at 2.86 GHz that was captured by the spectrum analyzer, due to the sweeping rate of the signal analyzer, and is not a made by our method. The demodulation of such signal will be explained in

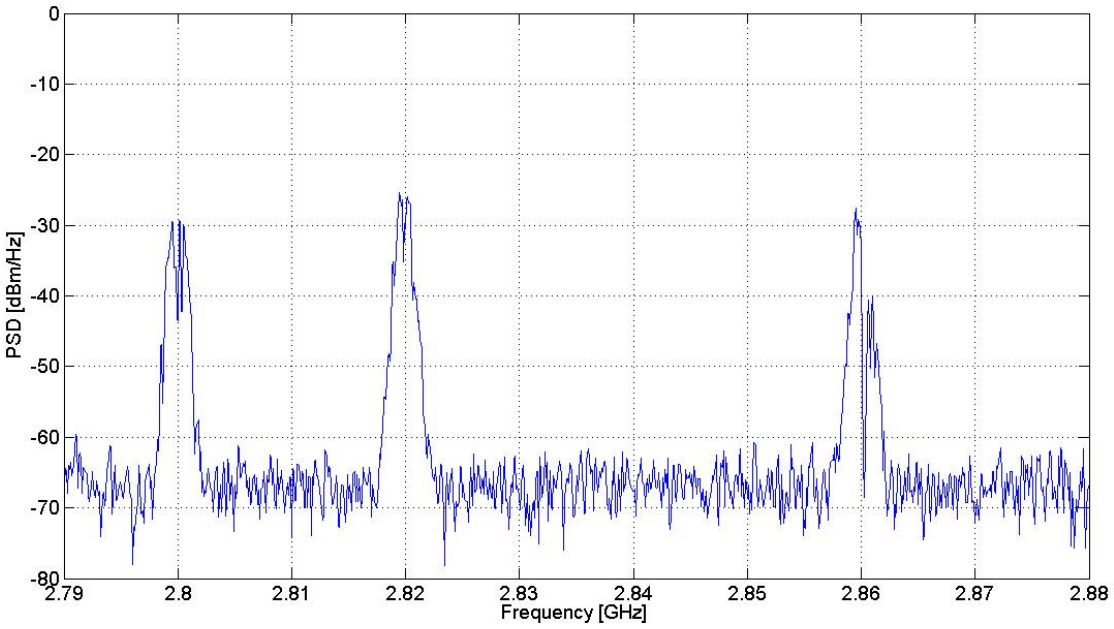

Figure 2.12: Three OFDM aggregated bands of 1.35 MHz at 2.8 GHz, 2.82 GHz and 2.86 GHz

section 2.6.1. In the next section a CA method with different OFDM signal at different component carriers using commercially available equipment is presented. The amplitude of the component carriers is also controllable. Moreover, due to the usage of commercial equipment, an analysis of the modulator imbalance and its compensation method is

proposed.

2.5 CA of Three OFDM Signals Using a Single Oscillator and I/Q Modulator

In this section a novel method is presented, which makes CA using a single LO and an I/Q modulator, possible. Three component carriers with OFDM symbols are generated at 2.2 GHz, 2.5 GHz and 2.9 GHz to show the feasibility of the method for the worst-case scenario that is the inter-band carrier aggregation. A special procedure to compensate the IQ imbalances specific to this method is explained as well. Moreover, according to Nyquist criterion, the signal should have a sampling rate of at least twice of the signal highest frequency. In this method the sampling rate of the DAC is significantly reduced, since the baseband signal is distributed over negative and positive frequencies.

Different methods have been proposed in literature for creating frequency aggregated signals. In [60] a dual-band CA architecture based on two separate signal generation chains was introduced, where the combiner is replaced by transistors to provide dynamic RF path for CA among different channels and bands. This method is costly when five component carriers are used. A sigma delta design is proposed in [61]. It consists of two band-pass delta-sigma modulators (BP-DSM) that share a portion of feedback loop to generate two stop-bands to suppress the quantization noise in the dual-band , while keeping the stability after the combination of the BP-DSMs. The adjacent channel leakage ratio (ACLR) is high (50 dB) for the bands close to the useful bands but the noise level is only 10 dB under useful signal (Fig. 8.). Moreover, a 6th order Chebyshev digital band pass filter is suggested which could cause instability in the system after several hours of operation. In addition, the system operates at 3.9 GS/s, which makes a very high power consumption.

In [62] an inter band CA method is proposed, which uses out-phased multi-level RF pulse width modulated signals to create two component carriers at 874 MHz and 1501 MHz using a class D power amplifier and an RF filter. The paper focuses on the power code

efficiency while its proposed method requires a very high sampling frequency (25 GS/s) since the component carriers are directly generated, digitally, on RF frequencies. ACLR is around 40 dB for the frequency bands close to both useful bands but large out-of-band (OOB) leakages are only 10 dB under the power levels of useful bands (Fig. 5.) that can potentially interfere with existing neighboring transmissions.

Software defined radio (SDR) can be used in intra-band CA. A CA based on IFFT pruning is proposed in [63] .The method describes how to create non-contiguous OFDM signals using FFT with zero-padding. In other words, to create two non-contiguous component carriers a FFT process is used where zeros are placed at the subcarriers that are between these two component carriers. In a similar work, [64] uses a universal software radio peripheral (USRP) to generate directly RF signal in 3 non-contiguous bands. The OFDM signal of 170 kHz bandwidth was generated at 2.4 GHz, then, by deactivating 40 subcarriers, 3 bands with bandwidths of 20 kHz and 60 kHz are created. These zero-padding IFFT techniques require long IFFT processes when component carriers are far from each other. This last problem is solved in the SDR proposed by [65] by using digital up-converter (DUC). The data is spread over N OFDM signals of moderate bandwidths, then up-converted by N DUC and digitally added before analogical conversion using high resolution DACs (14 bits) and high sampling frequency (2.4 GS/s) [65]. In this chapter, the same method of spreading the data over N OFDM signals will be used, but using the multiplication by a particular processing technique, which will be explained later, the requirement on the performance of the DAC will be relaxed.

2.5.1 CA of Three OFDM Signals Method

In this part, transmission of 3 different OFDM symbols over 3 component carriers will be explained. Moreover, it gives control over the amplitude of the component carriers which was not introduced in section 2.4. Mathematically three component carriers at RF frequencies f_1, f_2, f_3 ($f_1 < f_2 < f_3$) , as was shown in (1.2), can be written as:

$$x(t) = Re\left\{\alpha e^{i2\pi f_1 t} + \beta e^{i2\pi f_2 t} + \gamma e^{i2\pi f_3 t}\right\} \tag{2.14}$$

It can be rewritten as:

$$x(t) = Re\left\{\left(\alpha e^{i2\pi h_1 t} + \beta e^{i2\pi h_2 t} + \gamma e^{i2\pi h_3 t}\right) e^{i2\pi f_c t}\right\} \tag{2.15}$$

where:

$$\begin{aligned} h_1 &= f_1 - f_c & h_2 &= f_2 - f_c \\ h_3 &= f_3 - f_c & f_c &= \frac{f_1 + f_3}{2} \end{aligned} \tag{2.16}$$

α, β,γ are the amplitude of each component carriers.

The OFDM baseband signals at each carrier is defined as:

$$x_{OFDM_k}(t) = I_k(t) + jQ_k(t)t \quad k \in \{1, 2, 3\} \tag{2.17}$$

Where $I_k(t)$ and $Q_k(t)$ are the baseband in-phase and in-quadrature components of the OFDM signal.

By combining (2.16) and (2.17) symbols are modulated over component carriers by :

$$\begin{aligned} x(t) = Re\{&(\alpha\,(I_1(t) + jQ_1(t))\,e^{i2\pi h_1 t} + \beta\,(I_2(t) + jQ_2(t))\,e^{i2\pi h_2 t} \\ &+ \gamma\,(I_3(t) + jQ_3(t))\,e^{i2\pi h_3 t})e^{i2\pi f_c t}\} \\ = Re&\left\{(I(t) + jQ(t))\,e^{i2\pi f_c t}\right\} \end{aligned} \tag{2.18}$$

where the baseband in-phase and in-quadrature components are:

$$\begin{aligned} I(t) = &\alpha\,(I_1\cos(2\pi h_1 t) - Q_1\sin(2\pi h_1 t)) \\ &+ \beta\,(I_2\cos(2\pi h_2 t) - Q_2\sin(2\pi h_2 t)) \\ &+ \gamma\,(I_3\cos(2\pi h_3 t) - Q_3\sin(2\pi h_3 t)) \end{aligned} \tag{2.19}$$

$$\begin{aligned} Q(t) = &\alpha\,(I_1\sin(2\pi h_1 t) + Q_1\cos(2\pi h_1 t)) \\ &+ \beta\,(I_2\sin(2\pi h_2 t) + Q_2\cos(2\pi h_2 t)) \\ &+ \gamma\,(I_3\sin(2\pi h_3 t) + Q_3\cos(2\pi h_3 t)) \end{aligned}$$

There are couple of important implementation remarks. Firstly, as was mentioned in 2.4.1 the phase continuity is ensured by applying pulse shaping filter via the circular convolution. Secondly, in contrast to 2.4 where CA is used for frequency diversity, a

CAZAC training sequence is used in this section, since it is required in LTE/LTE-A [66]. Identical CAZAC training sequences are used for the OFDM signals transmitted by each component carrier to be conform with LTE/LTE-A. These identical TSs make no correlation because they are transmitted at different frequencies. Thirdly, based on Nyquist criterion the DAC sampling frequency must be at least twice of the highest frequency component of the signal. Moreover, the two extreme intermediate carrier frequencies (h_1 and h_3) are chosen to be equidistant from the origin, which minimizes the highest frequency component, hence :

$$f_{s_{carrier}} > 2|h_3| \tag{2.20}$$

where $f_{s_{carrier}}$ is the carrier sampling rate and h_3 is given in (2.16).

On the other hand, it is important to emphasize that the symmetrical distribution of the lowest and highest LIF components around 0 Hz was not applied in the case of generation of the frequency diversity CA signal, hence this method requires lower DAC sampling rate. Fourthly, the sampling rate of each OFDM signal must be equal to the sampling rate of the three component carriers. Hence, the OFDM symbols must be over sampled with the following ratio:

$$OSR_k = \frac{f_{s_{carrier}}}{R_{OFDM_k}} \quad k \in \{1, 2, 3\} \tag{2.21}$$

where R_{OFDM_k} and OSR_k represent the sampling rate of each OFDM signal and the corresponding oversampling ratio, respectively.

In practice, there are imperfections in all the stages of the transmitter. For instance, some errors are induced to the data because of the DSP precision, DAC quantification, post-DAC anti-aliasing filter, modulator I/Q imbalances, etc. There are two main I/Q imbalance parameters: phase imbalance and gain imbalance. They happen due to length difference and the phase response difference between the I and Q paths and these two parameters are dependent. In single carrier systems a factory calibration procedure is applied to the system to compensate these imperfections [67]. However, in our case, the modulator has to operate over three different frequencies, which make the usual

factory calibration ineffective. In the following sub-section this problem is analyzed and a practical compensation solution is proposed.

2.5.1.1 I/Q Imbalance Analysis

An ideal I/Q modulator has a phase difference of 90° between the paths I and Q, however, the systems have imperfections that make few degrees of phase difference from 90°. Hence (2.18) can be re-written as:

$$\begin{aligned} x(t) &= Re\left\{ (I(t) + jQ(t))\, e^{i2\pi f_c t} \right\} \\ I(t) &= \alpha \left(I_1 \cos(2\pi h_1 t + \phi_1) - Q_1 \sin(2\pi h_1 t + \phi_1) \right) \\ &\quad + \beta \left(I_2 \cos(2\pi h_2 t + \phi_2) - Q_2 \sin(2\pi h_2 t + \phi_2) \right) \\ &\quad + \gamma \left(I_3 \cos(2\pi h_3 t + \phi_3) - Q_3 \sin(2\pi h_3 t + \phi_3) \right) \\ Q(t) &= \alpha \left(I_1 \sin(2\pi h_1 t) + Q_1 \cos(2\pi h_1 t) \right) \\ &\quad + \beta \left(I_2 \sin(2\pi h_2 t) + Q_2 \cos(2\pi h_2 t) \right) \\ &\quad + \gamma \left(I_3 \sin(2\pi h_3 t) + Q_3 \cos(2\pi h_3 t) \right) \end{aligned} \tag{2.22}$$

Where ϕ_1 , ϕ_2, ϕ_3 are phase imbalances, induced by the modulator impairments, on the component carrier 1, 2, 3, respectively. One should pay attention that ϕ_1 , ϕ_2, ϕ_3 are different because the I/Q modulator components (mixer, combiner) have different phase responses at the three component carrier frequencies, hence each of them should be processed separately.

Another possible I/Q imbalance happens when a DC voltage is added on one of the paths which represents itself as carrier feed–through. Carrier feed-through can, also, happen due LO-IF leakage of the mixers. On should pay attention to the fact that the image of the one of the extreme intermediate frequencies coincides with the other one meaning that h_3 is equal to $-h_1$ or is in its close vicinity. In order to overcome this problem we can add a frequency offset to the carrier frequency so that the signals and the images do not coincide in expense of increasing a little the DAC sampling frequency. The difference between this case and the multi-tone case is the fact that, the overlap can happen because

of the large bandwidths of the component carriers. Hence, the carrier frequency of 2.16 becomes:

$$f_c = -\eta + \frac{f_1 + f_3}{2} \tag{2.23}$$

Where η is positive carrier offset.

In order to avoid any overlap of the extreme signals with their images η should be conditioned. Figure 2.13 depicts the case where the extreme signals and their images are close to overlap. Hence:

$$h_3 - \frac{BW3}{2} \geq -h_1 + \frac{BW1}{2} \Rightarrow \eta \geq \frac{BW1 + BW2}{4} \tag{2.24}$$

Where $BW1$ and $BW3$ are the bandwidths of the signal at h_1 and h_3, respectively. Second condition concerns aliasing of h_2 components:

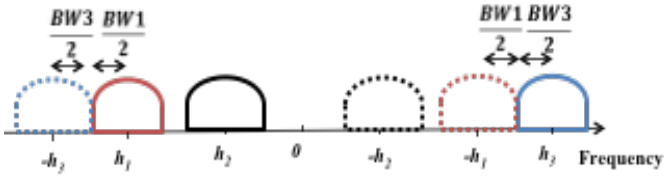

Figure 2.13: Combination of intermediate frequency signals and their images

$$|h_2| + \frac{BW2}{2} \geqslant \eta \tag{2.25}$$

Last condition is the overlap between h_2 and image of h_1 if $h_2 > 0$.

$$\begin{aligned} h_1 + h_2 &< \frac{BW1 + BW2}{2} \\ &\Rightarrow f_3 - f_2 > 2\eta + \frac{BW1 + BW2}{2} \end{aligned} \tag{2.26}$$

This condition is always fulfilled, since we are dealing with the case of inter-band carrier aggregation. In that case we can consider the 2$^{\text{nd}}$ component carrier far from the two other which avoids any overlap with others.

Figure 2.14 [2]shows the effect of these impairments on the spectrum of the carrier aggregated signals given in (7). $f1$, $f2$ and $f3$ are the desired component carriers but $Image1$,

[2]The spectrum is obtained from the measurement explained in 2.5.1.3

$Image2$ and $Image3$ are the corresponding image signals, respectively. Also the carrier feed-through represents itself as the strong signal at -40 dBm. In the case of generation of n bands, f_1, f_2,..., f_n are obtained similar to (2.16), (2.23) and (2.25). The value of the f_c is chosen as:

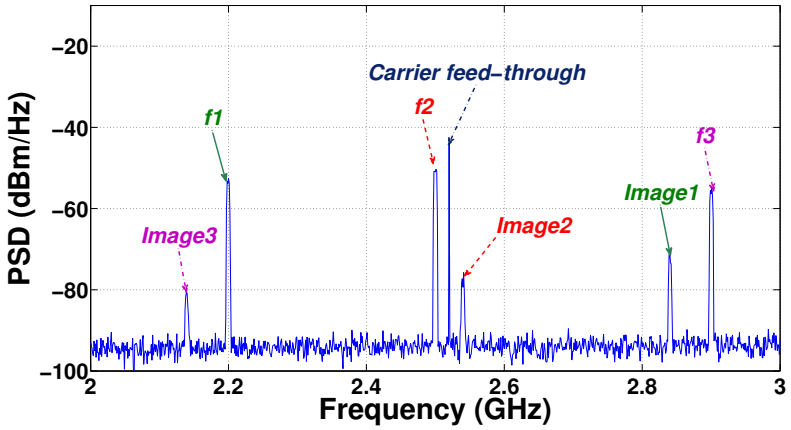

Figure 2.14: I/Q imbalance effect on the spectrum

$$f_c = -\eta + \frac{f_1 + f_n}{2} \quad with \quad \eta \geqslant \frac{BW1 + BWn}{4} \tag{2.27}$$

And if n is an odd number:

$$|h_g| + \frac{BWg}{2} \geqslant \eta \ , \ g = \frac{n+1}{2} \tag{2.28}$$

In the next section the compensation procedure for each of impairments is explained.

2.5.1.2 I/Q Imbalance Compensation

The mathematical analysis of I/Q imbalance of modulator is similar to the multi-tone signal generation, given in 1.4. A small phase imbalance in (2.22) may cause the images of component carriers appear on the spectrum as shown in Figure 2.14. To compensate, one should first analyze each component carrier and its image, separately, to obtain the corresponding phase difference. In another word, to find out the phase imbalance at the given component carrier frequency, a single carrier signal can be used to, manually, find

the phase that has the maximum reduction of the image signal. Once it happened the required phase can be used in (2.22) to mitigate, and in some cases to remove, the image signal. In the next section, the feasibility of the proposed method and the IQ calibration process are presented.

2.5.1.3 Signal Generation

Using the proposed method, a three-component carrier QPSK-OFDM signal, with different data over each of the component carriers, is generated with specifications given in Table 2.4. It is suitable for inter-band carrier aggergation because of the 100s of MHZ of difference between component carriers. Hence the test bench of Figure 1.13 is modified. A passive modulator was built by the commercially available equipment of the laboratory instead of the internal modulator of the Agilent N5172B. Moreover, a DAC (Tektronix AWG7122b) with a sampling rate up to 12 Gs/s was used and a series of anti-aliasing filters [3] fabricated for this purpose. Firstly, I and Q signals, given in (2.22),

RF Frequency	$f_1 = 2.2$ GHz	$f_2 = 2.5$ GHz	$f_3 = 2.9$ GHz	$f_c = 2.52$ GHz
LI Frequency	$h_1 = -320$ MHz	$h_2 = -20$ MHz	$h_3 = 380$ MHz	$\eta = 30$ MHz
Power	-42 dBm	-42 dBm	-42 dBm	10 dBm
Bandwidth	5 MHz	5 MHz	5 MHz	–
Sampling rate	1.14 GHz	1.14 GHz	1.14 GHz	–
Modulation	QPSK-OFDM			CW
N	32			–
L	8			–
DC-Null Subcarrier	✓			–
TS	CAZAC			–

Table 2.4: Specification of the carrier aggregated signal

are created using MATLAB® and transmitted through a general purpose interface bus (GPIB) connection to AWG7122b Tektronix arbitrary waveform generator. AWG7122b

[3] The design and layout is given Appendix II

creates the signal with a sampling frequency of 1.14 GHz, which is three times higher than $|h_3|$ as required in (2.20). It was chosen to be three times higher to avoid high order anti-aliasing filters (in our case order 2 passive LPF filters were used). As shown in the block diagram of Figure 2.15 (a), at the output of AWG7122b, I and Q signals are filtered using two Low pass anti-aliasing filters (LPF), fabricated in the laboratory, with a cut-off frequency of 500 MHz. Next, the signals are fed to the I/Q modulator (with passive mixers Avantek DBX-72-L1) through two bias tees (Picosecond 5575A). At the modulator, I and Q signals modulate the central carrier (f_c). The modulator consists of a two-way 90° power splitter (MCL ZAPDQ-4) and a two-way 0° power combiner (MCL ZAPD-4). Figure 2.15 (b) shows the photo of the test bench. As previously mentioned, an I/Q modulator calibration is needed to remove the spurs and the image signals. Figure 2.14 shows the output spectrum of the uncalibrated I/Q modulator (the signals are modulated on QPSK-OFDM which is not visible due to the large spectrum span of the figure). The calibration process was performed as described on 2.5.1.1. Each pair of signal and its image was studied, separately, to find the optimum phase compensation values that should be used in (2.20). The phase compensation values are given in Table 2.5. Since the transmissions in practical systems of the operators are done over a well-known series of configuration, a look-up table with different calibration parameters can be saved in a read only memories (ROM). Moreover pre-distortion methods can be used to compensate for IQ imbalances [68].

Figure 2.16 (a) represents the signal spectrum at the output of the modulator, when the calibration procedure is applied. Image2, Image3 are completely removed, when Image1 and carrier feed-through are mitigated by 15 dB and 49 dB, respectively. Theses mitigations can be improved by using components (power splitter, power combiner and precise DC power source to add in some cases tens or hundreds of microvolts) with higher precisions.

The method also gives a control over the transmitted power of the component carriers using α, β, γ parameters. For instance by choosing $\alpha = 0.1$ the component carrier at 2.2 GHz is attenuated by 20 dB, as shown in Figure 2.16 (b). These parameters enable the

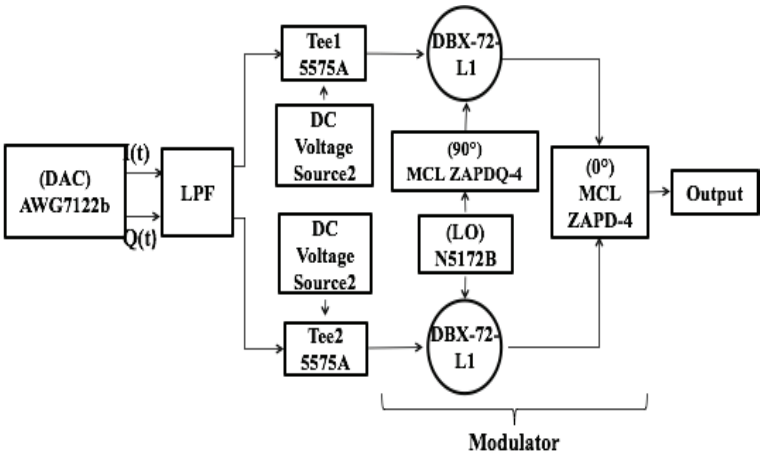

(a)

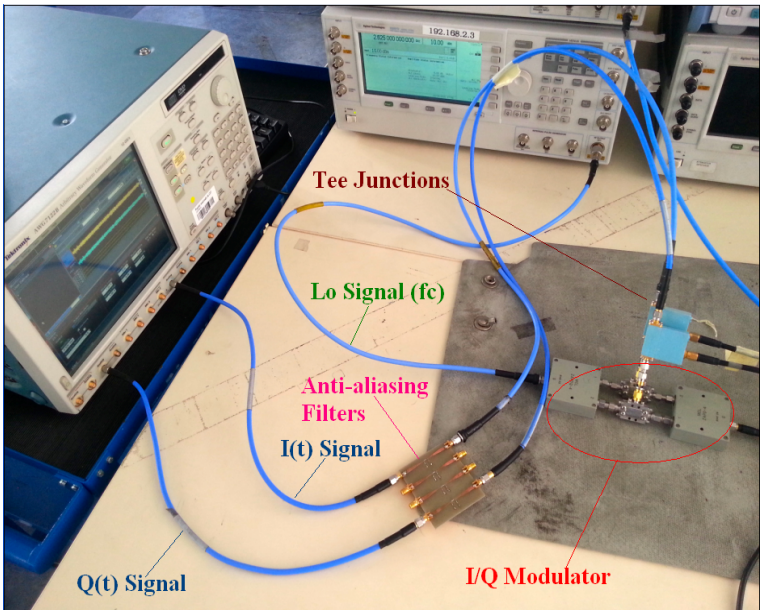

(b)

Figure 2.15: (a) Block diagram of the transmitter with passive modulator. (b) Photo of the test bench

user to adjust the signal as low as possible (till noise floor), which in the presented case means a dynamic range of 42 dB. One should pay attention that gain imbalance may be included in our compensation process but, since the images are well rejected, it is not included to reduce compensation process duration.

Component Carriers	**Images**	**Phase Compensation**
$f_1 = 2.2$ GHz	$Imag1 = 2.84$ GHz	$\phi_1 = 9.5\ ^\circ$
$f_2 = 2.5$ GHz	$Imag2 = 2.54$ GHz	$\phi_2 = 5\ ^\circ$
$f_3 = 2.9$ GHz	$Imag3 = 2.14$ GHz	$\phi_3 = -4\ ^\circ$

Table 2.5: Phase compensation

ACLR is an important parameter for transmitters to make sure not to disturb the adjacent channels. Table 2.6 presents the good quality of ACLR values of our transmitter for the three component carriers in the case of 5 MHz and 10 MHz of bandwidth. In this section, the generation of three-component carrier aggregated signal with QPSK-OFDM modulation was proposed and its feasibility was shown through experimental results. In the next section, the demodulation of such signal using a TPD and a vector signal analyzer (VSA) is discussed.

		$f_1 = 2.2$ GHz	$f_2 = 2.5$ GHz	$f_3 = 2.9$ GHz
$BW = 5$ MHz	Upper	-44.2 dBc	-45.5 dBc	-44.7 dBc
	Lower	-44.3 dBc	-45.8 dBc	-44.7 dBc
$BW = 10$ MHz	Upper	-42.6 dBc	-44.1 dBc	-43.1 dBc
	Lower	-42.6 dBc	-44.1 dBc	-43.1 dBc

Table 2.6: Measured ACLR for component carriers with BW of 5 MHz and 10 MHz.

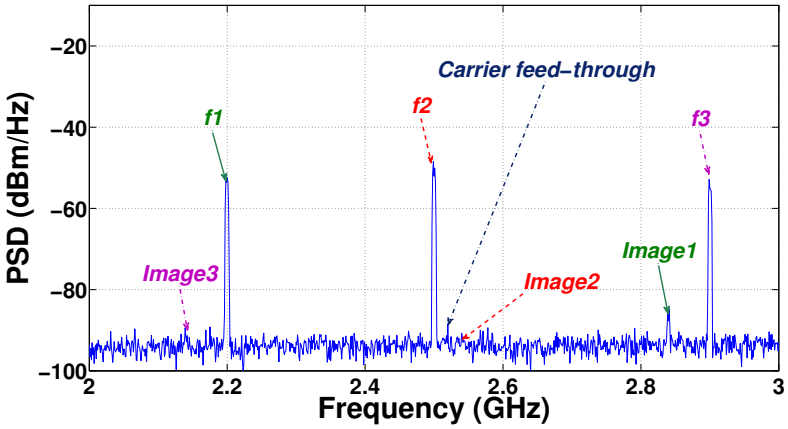

(a)

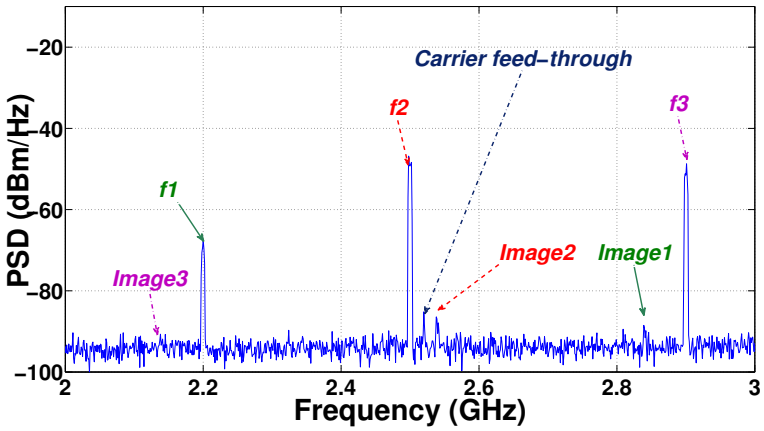

(b)

Figure 2.16: Spectrum of the output of I/Q modulator: (a) after calibration. (b) Transmission power control of each component carrier

2.6 CA signal demodulation

To demodulate CA signals couple of topology can be used, as is described in Figure 1.5. Two receivers were used to perform the demodulation. Firstly a TPD was used which which down converts, simultaneously, the wide band component carriers as LIF signal to reduce the DAC sampling frequency, as was explained in 1.5.2.1. Secondly, a Rhode & Schwarz VSA (FSW40) was used which down-converts each component carrier separately (not simultaneously) to baseband. FSW40 uses an internal ADC to sample the data which are extracted and processed digitally by PC.

2.6.1 Digital Signal Processing of CA Signal Demodulation

In TPD, component carriers are down-converted and sampled using a data acquisition board. The sampling frequency (*term used as sampling rate*) needs to be higher than retrieval band (B_r) that was explained in 1.5.2.1. Assume that N_{Tx} symbols are transmitted, including TS and data:

$$N_{Tx} = N_{TS} + N_{Data} \tag{2.29}$$

where N_{TS} and N_{Data} are the number of transmitted TS and data symbols. At the reception, using TPD, the number of recorded samples N_{Rx} must be at least twice the number of the transmitted symbols, to make sure that we acquire at least a complete set of TS and data, as depicted in Figure 2.17.

The signals are sampled with a sampling frequency higher than the $2 * B_r$ to validate

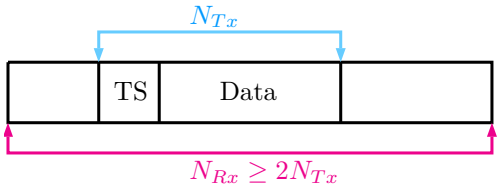

Figure 2.17: I/Q imbalance effect on the spectrum

the Nyquist criterion. Hence the received signal is sampled with an OSR given at (2.30).

This means at least $2 * OSR_{Rx} * N_{Tx}$ samples are required to be stored.

$$OSR_{Rx} = \frac{f_{s_{Rx}}}{R_{Tx}} \tag{2.30}$$

Where OSR_{Rx} is the OSR at the reception. $f_{s_{Rx}}$ is the acquisition board (or ADC) sampling frequency and R_{Tx} is the symbol rate. The in-phase and in-quadrature paths of the TPD are sampled at $T_{s_{Rx}}$ (where $T_{s_{Rx}} = \frac{1}{f_{s_{Rx}}}$) with an acquisition board, therefore:

$$\begin{aligned} P_I(t) &\Rightarrow P_I(nT_{s_{Rx}}) \\ P_Q(t) &\Rightarrow P_Q(nT_{s_{Rx}}) \end{aligned} \tag{2.31}$$

Where $P_I(nT_{s_{Rx}})$ and $P_Q(nT_{s_{Rx}})$ are the sampled in-phase, in-quadrature components of the TPD. Next, the DC component of the sampled $P_I(nT_{s_{Rx}})$ and $P_Q(nT_{s_{Rx}})$ are removed by subtracting their corresponding mean value from them. These two components can be written in terms of in-phase and in quadrature component of the transmitted symbols [69]

$$\begin{aligned} P_I(nT_{s_{Rx}}) &= x.I(nT_{s_{Rx}}) + jy.Q(nT_{s_{Rx}}) \\ P_Q(nT_{s_{Rx}}) &= z.I(nT_{s_{Rx}}) + jr.Q(nT_{s_{Rx}}) \end{aligned} \tag{2.32}$$

where x, y, z, r are real value parameters which show the imperfections induced by the receiver. A complex envelop is defined as:

$$e(nT_{s_{Rx}}) = P_I(nT_{s_{Rx}}) + j.P_Q(nT_{s_{Rx}}) \tag{2.33}$$

by combining (2.32) and (2.34):

$$e(nT_{s_{Rx}}) = (x + jy).I(nT_{s_{Rx}}) + (z + jr).Q(nT_{s_{Rx}}) \tag{2.34}$$

We define a vector of the complex envelop E_n:

$$E_n = \begin{bmatrix} e(nT_{s_{Rx}}) \\ e\left([n + OSR_{Rx}]T_{s_{Rx}}\right) \\ e\left([n + 2.OSR_{Rx}]T_{s_{Rx}}\right) \\ \vdots \\ e\left([n + (N_{TS} - 1).OSR_{Rx}]T_{s_{Rx}}\right) \end{bmatrix} \tag{2.35}$$

Among all the stored samples there is at least one series of samples that represents the TS of the transmitted signal, hence, time-domain synchronization can be established. This series is found by correlating the ideal TS symbols with $e(nT_{s_{Rx}})$, via MMSE algorithm. Lets B denote the vector of an ideal TS, hence:

$$E_n = B. \begin{bmatrix} x + jy \\ z + jr \end{bmatrix} \tag{2.36}$$

where

$$B = \begin{bmatrix} I(1) & \dots & I(N_{TS}) \\ Q(1) & \dots & Q(N_{TS}) \end{bmatrix}$$

x, y, z, r can be estimated using the MMSE algorithm:

$$\begin{bmatrix} \hat{x} + j\hat{y} \\ \hat{z} + j\hat{r} \end{bmatrix} = (B^T.B)^{-1}.B.E_n \tag{2.37}$$

Moreover an estimation of the vector E_n is obtained by combining (2.36) and (2.37):

$$\hat{E_n} = B.(B^T.B)^{-1}.B.E_n \tag{2.38}$$

Hence the beginning of the TS is where the quadratic error between E_n and $\hat{E_n}$ is minimum:

$$e(n) = (E_n - \hat{E_n})^H.(E_n - \hat{E_n}) \tag{2.39}$$

where $e(n)$ is the quadratic error, and $(.)^H$ is the Hermitian operator. Moreover, (2.39) can be simplified as :

$$e(n) = \hat{E_n}^H.C.E_n \tag{2.40}$$

with $C = Id(N_{TS}) - B.(B^T.B)^{-1}.B^T)$ where $Id(N_{TS})$ is an $N_{TS} * N_{TS}$ identity matrix. Finally, $e(n)$ is calculated over $n = \{0, \dots, (N_{Rx} - N_{TS} + 1)OSR - 1\}$ the instant n_{opt} locates when $e(n)$ is minimized.

On the other hand, the TS gives us the estimation of x, y, z, r which can help extract from the received $P_I(nT_{s_{Rx}})$ and $P_Q(nT_{s_{Rx}})$. By combining (2.32) and (2.37), one can

obtain:

$$\begin{bmatrix} P_I(nT_{s_{Rx}}) \\ P_Q(nT_{s_{Rx}}) \end{bmatrix} = \begin{bmatrix} x & y \\ z & r \end{bmatrix} \begin{bmatrix} I(nT_{s_{Rx}}) \\ Q(nT_{s_{Rx}}) \end{bmatrix} \tag{2.41}$$

Hence by multiplying both sides by inverse of the parameters matrix we obtain:

$$\begin{bmatrix} I(nT_{s_{Rx}}) \\ Q(nT_{s_{Rx}}) \end{bmatrix} = \begin{bmatrix} x & y \\ z & r \end{bmatrix}^{-1} \begin{bmatrix} P_I(nT_{s_{Rx}}) \\ P_Q(nT_{s_{Rx}} \end{bmatrix} \tag{2.42}$$

The estimations of x, y, z, r are available from (2.37), which lead us to the I/Q data. Now that the IQ data are available, the OFDM baseband signal must be demodulated to recover the transmitted symbols, as it is shown in Figure 2.10(b). The steps shown in Figure 2.10(b) needs to be completed to be conform with a complete demodulation process, as depicted in Figure 2.18. If a root raised cosine filter is used as pulse-shaping method at the transmitter, the pulse-shaping filter effect is removed at the receiver from ($P_I(nT_{s_{Rx}})$, $P_Q(nT_{s_{Rx}})$) by applying the same filter. On the other hand if only, raised cosine filter is used, no pulse shaping effect removal is necessary. Next, the time synchronization is performed using the methods that was explained earlier. Furthermore, the recovered baseband ($I(nT_{s_{Rx}})$, $Q(nT_{s_{Rx}})$) signals are obtained using (2.42). The next step is to remove the CP to eliminate ISI effect. Then, the symbols pass through a serial to parallel step. Next the N-FFT operation is applied to remove the N-IFFT effect of the transmitter (the symbols are transformed in frequency domain). The following step is to put the symbols in series and apply channel equalization, if necessary, to the frequency domain symbols. Finally, the transmitted symbols are recovered.

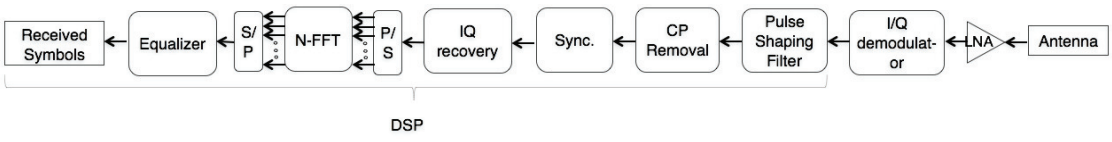

Figure 2.18: Demodulation process

Remark 2.1. The DSP of demodulation process using VSA is similar to the TPD receiver, hence it is not re-stated here.

2.7 Experimental Results

In this section, the frequency diversity CA OFDM signal presented in 2.4.1 and the three OFDM CA signal presented in 2.5.1.3 are demodulated using TPD and VSA. The experiment conditions are explained, the results are analyzed and compared to the state of the art.

2.7.1 Demodulation of Frequency Diversity CA OFDM Signal

The overall system test bench is depicted in Figure 2.19. At the transmitter side, the CA signal with component carriers at 2.8 GHz, 2.82 GHz and 2.86 GHz are created using Agilent N5172B (right side magenta box) with an output power of -30 dBm. The spectrum of the CA signal is given in Figure 2.12. The signal is injected to the TPD where it receives the 3 LO signals (left side blue boxes) at 2.797 GHz, 2.813 GHz and 2.847 GHz with an output power of -10 dBm. LOs are combined using Anaren 043020 combiner and injected in TPD. Hence, the CA signal is down-converted to 3 MHz, 7 MHz, and 13 MHz. At the output of the I/Q regeneration board of the TPD[4], in-phase and in-quadrature paths are sampled at 100 Ms/s using Spectrum Instrument M3i21 acquisition board. Finally the sampled data are processed as explained in 2.6.1.

Figure 2.20 depicts QPSK constellations of our received symbols. The dispersion in the constellations (red stars) (a), (b) and (c) are due to the nonlinearity of the TPD mixer (harmonics and spurs) that happen when the transmitter LIF signals are not far away from each other. Here the LIF signal separation is limited by the sampling frequency of the DAC available on Agilent N5172B, which is 150 MS/s. According to the Nyquist criterion, the used DAC can generate CA signals with a separation up to 75 MHz. By turning off two of the LOs, the harmonics and nonlinearities are reduced, however, two undesired LIFs still, happen due to the mixing process of the three RF bands with the unique LO signal. The blue circles of Figure 2.20 (a), (b) and (c) represent the constellation of RF bands at 2.8 GHz, 2.82 GHz and 2.86 GHz down-converted, by sequentially

[4] A brief introduction to TPD is given in Appendix III

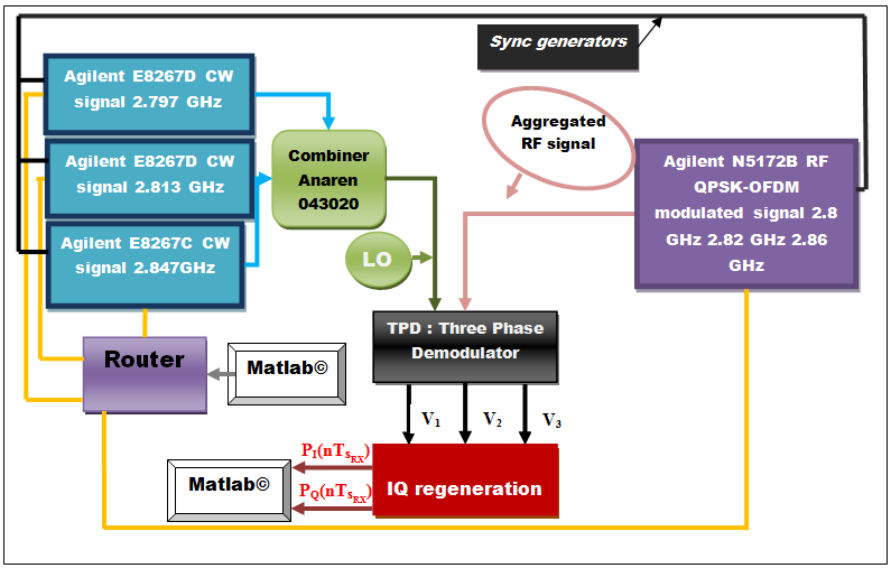

Figure 2.19: Measurement test bench

changing the frequency of the LO signal, to LIF centered at 13 MHz, respectively. The comparison with previous results, constellation (a) and (b), demonstrates the distortion reduction which is expected since less Intermodulation components and spurs happen close to the LIF band.

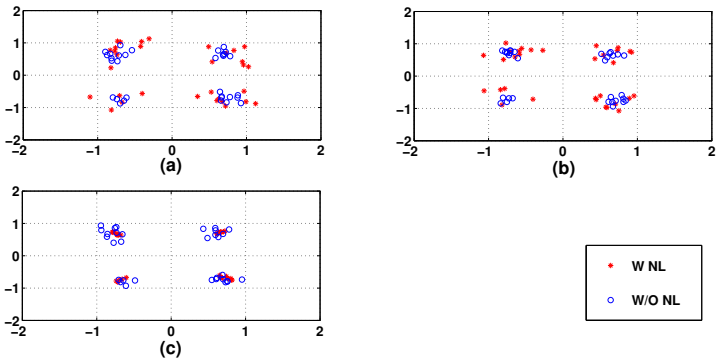

Figure 2.20: Symbol constelation with (red stars) and without (blue circles) non-linearity (a) QPSK, LIF centered at 3 MHz, (b) QPSK, LIF centered at 7 MHz, (c) QPSK, LIF centered at 13 MHz

2.7.2 Demodulation of CA OFDM Signals

In this section, the signals, shown in Figure 2.16(a) are demodulated using the test bench depicted in Figure 2.21, where the transmitter equipment were changed to have a higher bandwidth (right side of the figure). The signals are down-converted using three local oscillators, set at 2.17 GHz, 2.488 GHz and 2.895 GHz to low intermediate frequencies of 5 MHz, 12 MHz and 30 MHz, as shown in Figure 2.22. These LIF signals are sampled at 100 MS/s using Spectrum Instrument M3i21 acquisition board. After applying the low pass filter, the TS is estimated using the MMSE algorithm. As an example, in one of the signals, the TS start at 1430_{th} sample, as shown in Figure 2.23. The rest of the demodulation is performed as explained in 2.6.1. On the other hand, VSA is a single band receiver which down converts the RF signal to baseband and samples it. In this work the data are sampled at 100 MS/s. Figure 2.24 presents the demodulated (sampled by VSA) symbol phase constellations for 4-QAM, 16-QAM and 64-QAM modulations of the component carrier at 2.5 GHz (the middle component carrier of the aforementioned 3 component carrier signal) over three different transmissions.

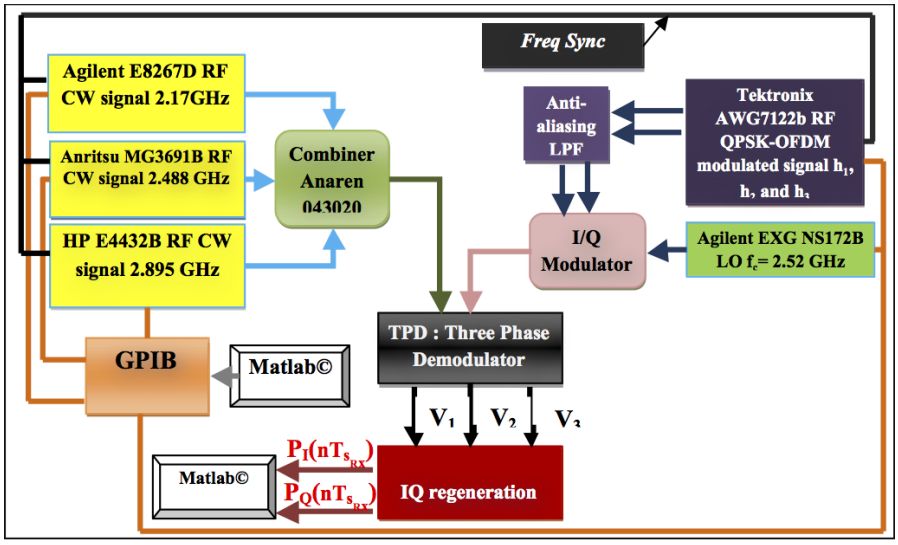

Figure 2.21: Carrier aggregation transmitter (right side blocks) and the reception structure with a TPD receiver (left side blocks)

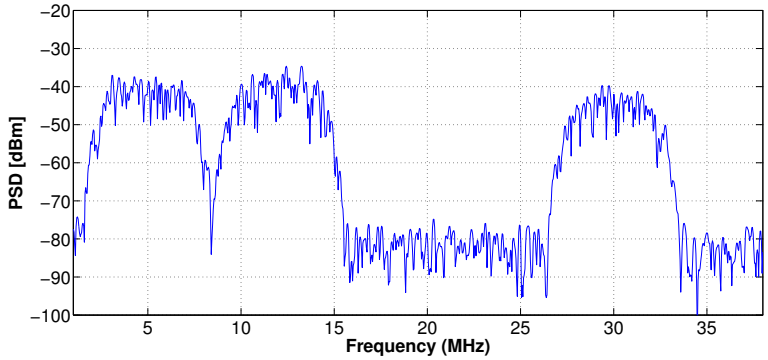

Figure 2.22: RF signals @ 2.2 GHz, 2.5 GHz, 2.9 GHz translated to LIF @ 5 MHz, 12 MHz and 30 MHz

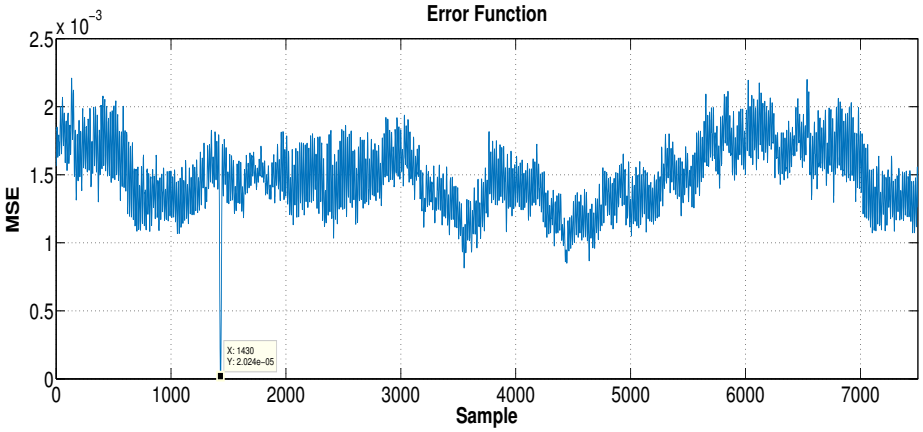

Figure 2.23: MSE in function of the sample number

To estimate the performance of the signal at the receiver, the EVM measurements for each component carrier are performed, as shown in Figure 2.25 (a) The EVM curves show a demodulation quality of the TPD for the component carriers at 5 MHz, 12 MHz and 30 MHz. Moreover, the EVM performance was tested for a case, as shown in Figure 2.25 (b), where the component carriers occupy a bandwidth of 10 MHz and they are down-converted at 10 MHz, 30 MHz and 50 MHz. Figure 2.25 (c), (d) show the EVM performance with the VSA for different modulation orders which shows an improvement of 15 dB with respect to TPD at received power of -42 dBm, which is maybe due to the

fact that VSA is designed as a high performance measurement instrument. Moreover, in 4-QAM with a BW of 5 MHz (Figure 2.25 (a) -(c)) around -60 dBm reception power, TPD and VSA have the relatively same values, but in low reception powers (around -70 dBm) TPD has higher performance on the component carrier at 2.9 GHz by factor of 5 dB and an equal performance for two other component carriers are observed for TPD and VSA. In the case of 4-QAM with a BW of 10 MHz (2.25 (b) -(d)), we observe a similar behavior. At reception power around -42 dBm the VSA is better with a factor of 15 dB but this difference is reduced when the reception signal is weak. Around -66 dBm of the reception power the VSA is better about 2 dB in average of the three component carriers. In both cases with TPD, we observe a good EVM performance even at low power signals below -60 dBm. As a comparison, in [70] a carrier aggregated communication with three component carriers generated by three different signal generators were demodulated using TPD. For a QPSK signals with 200 KHz of bandwidth the EVM performance is lower than our method. For instance at input power of -60 dBm our EVM in the case of Figure 2.25 (a) values are improved by 9 dB and 1 dB for the first and the second component carrier, respectively. In the case of Figure 2.25 (b) values are improved by 9 dB, 5 dB and 7 dB for the first and the second component carrier, respectively.

The previous comparison is partially right since the signal bandwidth, the LIF signal locations and the mixers are not the same, but despite the large bandwidth used in this work the EVM performance is enhanced. This might, also, be due to the fact that our signals have high oversampling factor at the transmitter ($OSR = \frac{1140MHz}{5MHz} = 228$).

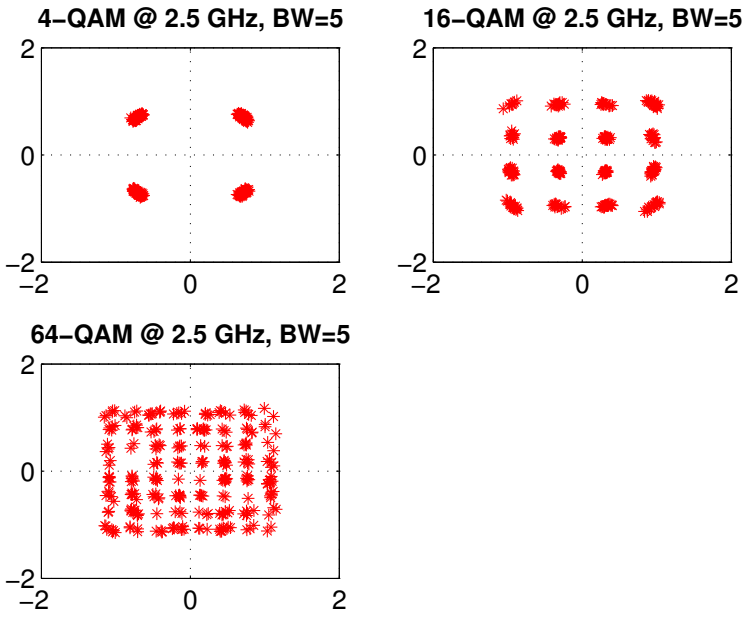

Figure 2.24: RF signals @ 2.2 GHz, 2.5 GHz, 2.9 GHz translated to LIF @ 5 MHz, 12 MHz and 30 MHz

Table 4 gives a comparison between this work and some similar works. First column gives the used techniques: $\Delta\Sigma$ [61], $\Delta\Sigma$ + Out Phased Multi-level RF Pruning [62], IFFT Pruning URSP2 [64], DUC [65] and our method. Second column gives the maximum and minimum frequencies, and the bandwidth of each modulated signal; generally in the range [0.8 2.4] GHz and 10 MHz, respectively, except [65] where the values are [6.15 - 6.6] GHz and 122 MHz. The third column gives the value in dBc of the rejection of the spurious signals and the dynamic range of components carriers. The techniques using DUC [65] and ours show a rejection better than 35 dB instead of 10 and 20 dB demonstrated by [61], [62], [64]. In this work in contrast to others, there is control of 42 dB over each component carrier frequency. Last column gives the sampling frequency of the DAC, the ACLR and EVM. The DAC in our method has the lower frequency sampling 1.14 GS/s, except [64] where the signals are narrowband and suitable for intra-band carrier aggregation. That why the EVM performance, -44 dB, given in [64] is better than in

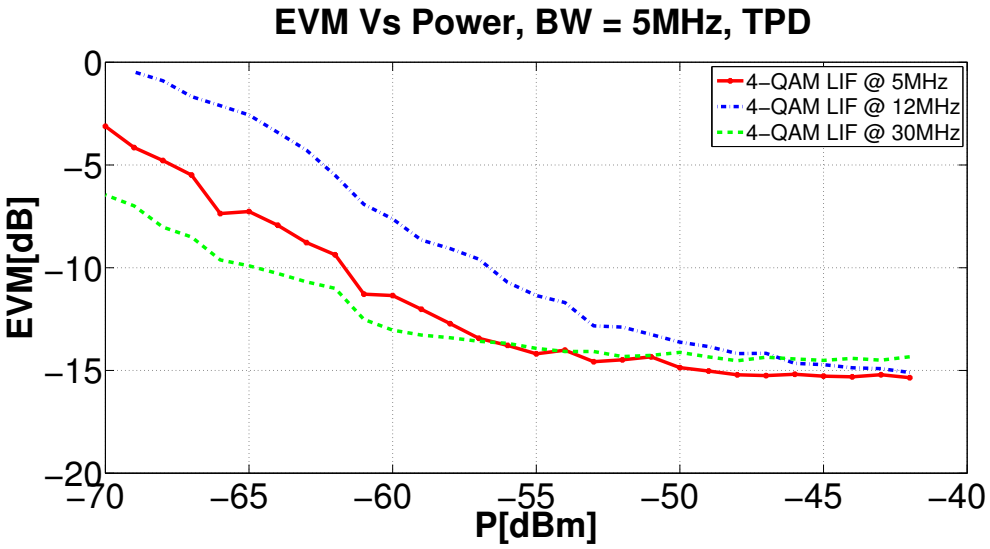
EVM Vs Power, BW = 5MHz, TPD
EVM[dB]
P[dBm]
4−QAM LIF @ 5MHz
4−QAM LIF @ 12MHz
4−QAM LIF @ 30MHz
0
−5
−10
−15
−20
−70
−65
−60
−55
−50
−45
−40

(a)

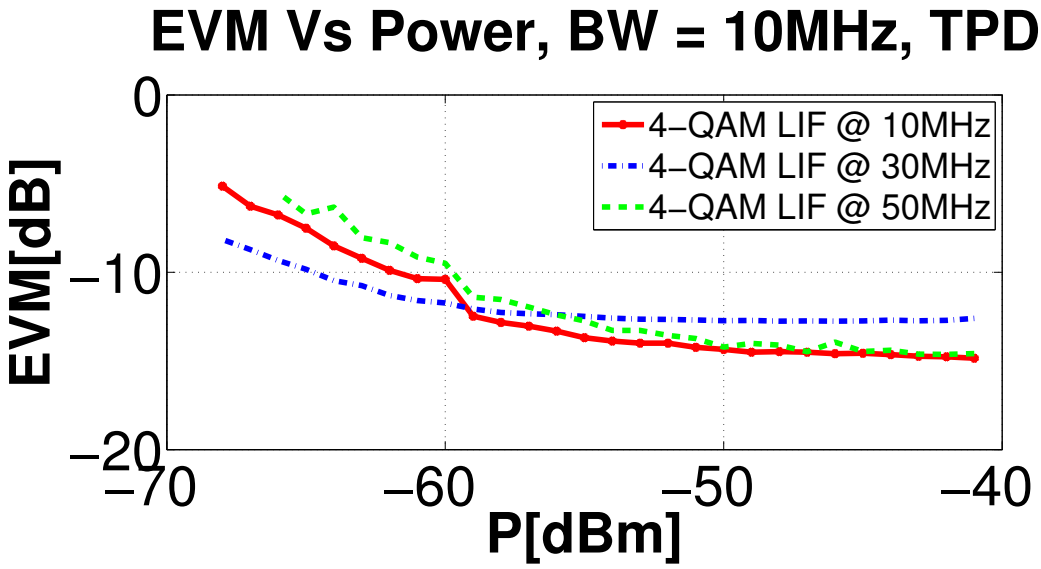
EVM Vs Power, BW = 10MHz, TPD
EVM[dB]
P[dBm]
4−QAM LIF @ 10MHz
4−QAM LIF @ 30MHz
4−QAM LIF @ 50MHz
0
−10
−20
−70
−60
−50
−40

(b)

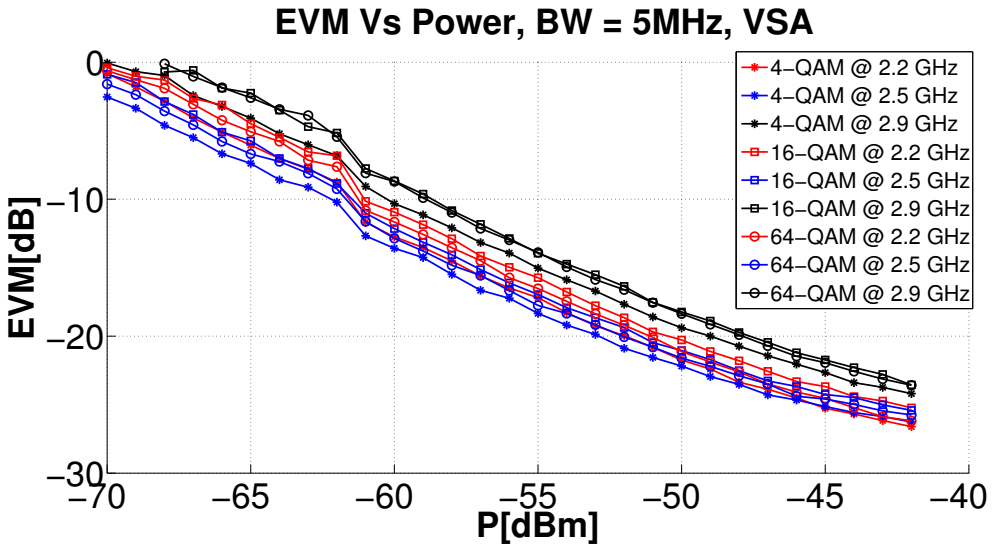

(c)

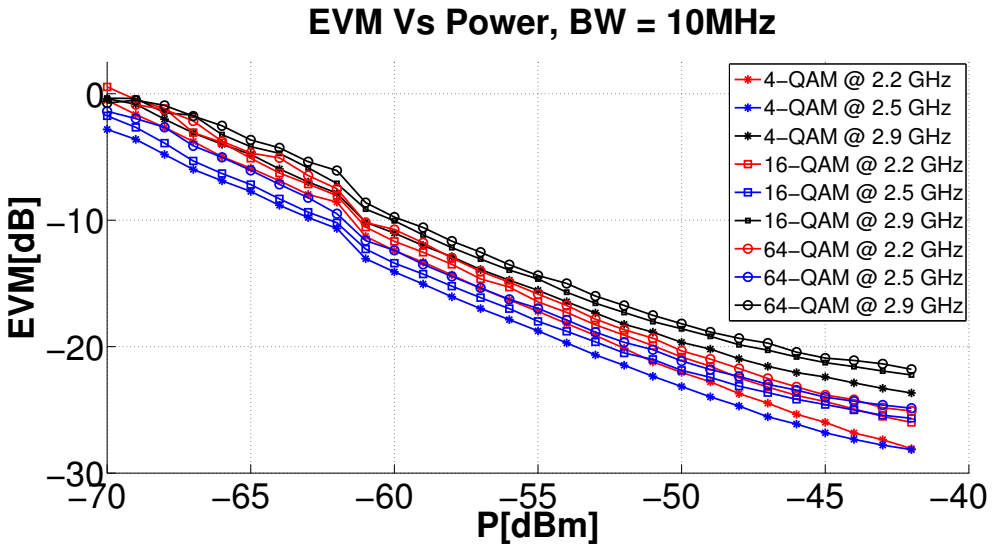

(d)

Figure 2.25: (a) EVM measurement using TPD for LIF 4-QAM signals with 5 MHz of bandwidth @ 5 MHz, 12 MHz and 30 MHz. (b) EVM measurement using TPD for LIF 4-QAM signals with 10 MHz of bandwidth @ 10 MHz, 30 MHz and 50 MHz (c) EVM measurement using FSW R&S VSA for 4-QAM, 16-QAM, 64-QAM signals with 5 MHz of bandwidth. (d) EVM measurement using FSW R&S VSA for 4-QAM, 16-QAM and 64-QAM signals with 10 MHz of bandwidth.

this work, -28 dB. Finally the obtained ACLR value 43 dB is lower the 50 dB shown by $\Delta\Sigma$ technique, but in this last case at the expense of low rejection of the spurious signals [61].

Techniques	$[f_{min}\ f_{max}]$	**Spurs and/or intermodulation component (dBc)**	**Sampling frequency GS/s**
	Bandwidth	**Component carrier**	**ACLR (dB)**
	Component carriers	**dynamic range**	**EVM [dB]**
$\Delta\ \Sigma$ [61]	[0.8 1.5] GHz	-10	3.9
	5 MHz	N.A.	50
	2		N.A.
$\Delta\ \Sigma$ **+Out Phased Multi-level RF Pruning [62]**	[0.87 1.5] GHz	-10	25
	10 & 20 MHz	N.A.	40
	2		N.A.
IFFT Pruning URSP2 [64]	2.4 GHz + [-80 80] KHz	-20	0.1
	20&60 MHz	N.A.	N.A.
	2		-44
DUC [65]	[6.15 6.6] GHz	45	2.4
	14 & 122 MHz	N.A.	N.A.
	4		N.A.
CA OFDM Signals (This Work)	[2.2 2.9] GHz	35	1.14
	5 & 10 MHz	42	43
	3		-28

Table 2.7: Characteristics comparison

2.8 Conclusion

In this chapter, Firstly, an introduction about LTE-A was given. Secondly, OFDM signal modulation and demodulation and their application in LTE-A were demonstrated. Thirdly, CA aggregation as a frequency diversity solution, using a single transmission chain, was proposed, which makes a trade off between the transmission efficiency and robustness, because identical data are transmitted over 3 component carriers. Fourthly, a method to generate a carrier-aggregated signal with three component carriers with OFDM modulation is presented. These signals are created using a single classical I/Q modulator and a single LO. Moreover, it can be adapted to a case with n component carriers by modifying the mathematical development. The proposed method uses a single transmission chain instead of three, hence a significant reduction in cost and energy consumption. Moreover, the sampling rate of the transmitter DAC is significantly reduced. In the example given in 2.5.1.3, the DAC has a sampling frequency of 1.14 GHz, which can be lowered to 760 MHz by using a higher order anti-aliasing filter, while for direct generation of these RF signals, as Nyquist criterion requires, a sampling frequency, at least twice the highest frequency, is needed, which would need a DAC with a sampling frequency of at least 5.8 GHz (2 x 2.9 GHz). Also, an I/Q calibration method specific to our method is proposed to mitigate the I/Q imbalances of the modulator. Once the calibration parameters are obtained, they can be stored in a look-up table to use them when the frequency configuration of the transmitter is changed.

In the last part, the demodulation process of such a signal using a three-phase demodulator and FSW40 R&S VSA was described. Experimental results such as demodulated symbol phase constellations and the EVM versus the input power of the receiver were given. The EVM performance was enhanced with respect to a similar work. There are some challenges for this system, which mainly concerns power amplifiers. The PA should be able to amplify over a wide frequency band, which is a hard task. Many solutions, using digital pre-distorters [71]-[72], give good results to fit PA to wideband or multiband signals. In the next chapter the nonlinearity behavior exhibited in this chapter will be

discussed and behavioral modeling will be used to overcome this issue.

Chapter 3

Behavioral Modeling for Multi-band Modulator Correction

High data rate transmissions require wideband signal. The signal faces different sources of imperfection before being transmitted by the antenna. First, quantization error, gain imbalance, phase imbalance, etc. can occurs because of the DAC imperfections. Second, carrier feed through and low nonlinear behavior may happen at the mixers of the modulator, as mentioned in chapter 2. Moreover, gain and phase imbalances can also occur due to small differences in I/Q paths of the modulator. Third, power amplifier (PA), which is placed before the antenna, add strong nonlinearities which manifest themselves as inter-modulation and harmonic components. In this chapter, we focus on the nonlinearities (in the presence of phase and gain imbalance) due to multi-band I/Q modulator and PAs, its impact on the transmission and how to fight these effects using behavioral modeling and DPD techniques.

3.1 Introduction

In communication transmitters, nonlinear behaviors are rarely, useful. Introduction of variable amplitude modulated signals, such as OFDM signaling, triggers more nonlinear effect on the transmitters than before. Moreover, PAs are operated near to their saturation region, to have the maximum efficiency. Peak to Average Power Ratio (PAPR) is a major problem for PA. It is inversely proportional to the efficiency. For instance, a signal with a PAPR of 10 dB may have an efficiency of only 5 % in a class-A PA and an efficiency of 28 % in a class-B PA [73]. There are three main methods for PA linearization:

- feed-forward linearization
- feed-back linearization
- predistortion linearization
- DPD linearization

There are different methods proposed for feed-forward linearization. In [74], a class-F PA is loaded with another class-E PA. The output of the class-F PA is captured. A portion of the captured signal is attenuated and compared with the RF input of the PA. Once the distortion is calculated, it gets amplified by class-E PA and the output of the class-E amplifier (pure distortion signal) is subtracted from the class-F amplifier (signal + distortion) to obtain a distortion-less signal. Another feed-forward method is to use band-pass filters to choose the higher harmonics (3^{rd}, 5^{th}, etc.) and down-convert them to the fundamental frequency where they are subtracted from the output of the PA. Hence their direct effect is removed from PA output. Feed-forward methods have good stability and high inter-modulation suppression, however they are sensitive to environmental changes and they have high implementation cost.

Feed-back methods, also called Cartesian feed-back methods, down-convert the output of the PA to I/Q components (Cartesian components). These I/Q components are subtracted with the input I/Q components. Then the corrected I/Q components are up-

converted and sent over PA [75].

RF/IF analog predistorters are also used to compensate the nonlinearities. In [76], a simple method is proposed where the signal is split into a linear path and a nonlinear path. They are subtracted before being transmitted through PA. For instance, to compensate 2^{nd} nonlinearity, the signal passes through a diode (because of the quadratic nature of the diode) in the nonlinear path, then nonlinear signal is subtracted from the linear signal and used as a predistorted signal. Analog predistortion is good for multi-carrier wide-band applications but it is very costly and complex when nonlinearity order is high. DPD linearization is extensively used in the modern communications. First the system model (I/Q modulator, PA, etc.) must be known. Then an inverse of such model is applied to predistort the system input signal. The problem is that the detailed model of each component of the transmitter might not be available or the overall model might be very complex, hence one approach is to replace the electrical model with the behavioral model of the signal [77]. Using behavioral modeling the functionality of the system is studied through analyzing input and output signals and adapting a proper model to them. Once the behavioral model is obtained, the baseband signal is digitally pre-distorted to manifest an inverse behavior of the model.

3.1.1 Mono-Band Digital Pre-Distorter (DPD)

In this part, firstly, couple of state of the art behavioral models are presented and then the DPD functions are described. In behavioral modeling of the RF systems, two factors are important which are the memory effect and the order of nonlinearity. Memory effect means that the output sample depends not only on the current input sample but also on the previous ones. There are two mains types of memory effects which are, electro-thermal memory effect and electrical memory effect [78]-[79]. Electro-thermal memory is due to the temperature variations at the junction levels of the PA transistors, but electrical memory relates to the signal bandwidth at RF frequencies and baseband level. For wideband signals (higher than 1 MHz) the electrical memory is the dominant type. It can also be considered as main memory factor in wideband I/Q Modulators, too. In

[80], a measurement method of memory effect intensity is proposed. It is based on the fact that the memory effect on the memoryless DPDs has a residual spectral regrowth effect and measurement is performed by calculating the ratio of the out-of-band spectrum power and the in-band spectrum power.

Now that the importance of memory effect in wideband systems is clear, any effective behavioral model should consist of memory effects and nonlinearities. The most comprehensive and exact form of nonlinear system model is proposed by discrete time Volterra series as shown in :

$$y(n) = \sum_{k=1}^{N} \sum_{m_1=0}^{M} ... \sum_{m_p=0}^{M} h_p\left(m_1, ..., m_p\right) \prod_{j=1}^{k} x(n - m_j) \tag{3.1}$$

where $x(n)$, $y(n)$, $h_p\left(m_1, ..., m_p\right)$, M, N are the input signal, output signal, Volterra parameters function (also called Voltera kernel), the memory depth and the order of nonlinearity. For high orders of nonlinearity and memory length, Volterra model becomes very complex which limits its usage in practical situations. Nevertheless, some methods are proposed to reduce its complexity in [81]- [82].

Remark 3.1. Any transform T is an integral transform when it can be written as :

$$Ty(u) = \int_{t_{1_{min}}}^{t_{1_{max}}} \int_{t_{2_{min}}}^{t_{2_{max}}} ... \int_{t_{n_{min}}}^{t_{n_{max}}} K(t_1, t_2, ..., t_n) x(u - t_1) x(u - t_2) ... x(u - t_n) dt_1 dt_2 ... dt_n$$

where $K(t_1, t_2, ..., t_n)$ is known as the kernel of the integral transform. The same transform is valid for discrete variable where integrals are replaced by summations

Another model is Hammerstein model which breaks down the model into two parts [83]-[84]. It is composed of a memory-less nonlinear system for modeling the nonlinearities and a time invariant system for modeling the memory effect (the system delay models the memory effect) as depicted in Figure 3.1(a). The first step is written as:

$$w(n) = \sum_{k=1}^{N} \gamma_k x(n) |x(n)|^k \tag{3.2}$$

where $w\left(n\right)$ represents the memory-less nonlinear system based on power series of order N. The second step is to convolve $w\left(n\right)$ with the time invariant system (IIR filter), as

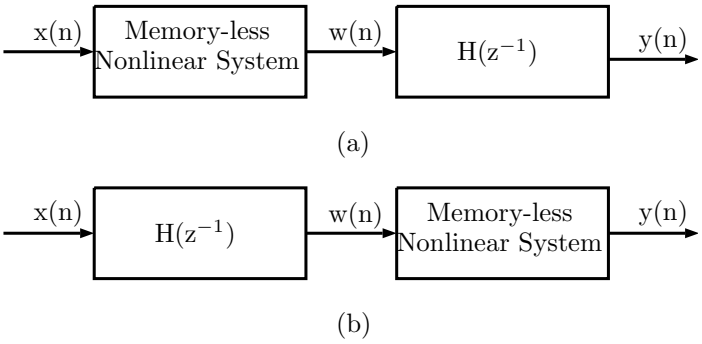

Figure 3.1: PA Models: (a) Hammerstein, (b) Wiener

shown:

$$y(n) = \sum_{p=0}^{P} \alpha_p y(n-p) + \sum_{z=0}^{Z} \beta_z w(n-z) \tag{3.3}$$

where $y(n)$ is the output, P is the pole order and Z is the zero order.

Wiener model is the reciprocal form of Hammertien model[83]. The signal, first, passes through a time invariant system, then nonlinear memory-less step is applied as shown in Figure 3.1(b). The first step is written as:

$$w(n) = \sum_{z=0}^{Z} \beta_z x(n-z) \tag{3.4}$$

where $w(n)$ is the convolution of the input signal and the time invariant system (Z-tap FIR filter). In the second step, $w(n)$ passes through a memory-less nonlinear model as given:

$$y(n) = \sum_{k=1}^{N} \gamma_k w(n)|w(n)|^k \tag{3.5}$$

Where $y(n)$ is the output and N is the order of nonlinearity. Both Hammerstein and Wiener model can be written in matrix form for easier estimation of the model coefficients (α_p, β_z,γ_k) using linear regression [83].

Memory polynomial model is a simplified model of Volterra series where only diagonal terms are used. It was proposed in [85] as:

$$y(n) = \sum_{m=0}^{M} \sum_{k=1}^{N} \beta_{mk} x(n-m)|x(n-m)|^{k-1} \tag{3.6}$$

Where $y(n)$, $x(n)$, β_{mk},N, M are the output signal, input signal, the model coefficients, the nonlinearity order and the memory depth, respectively. The memory polynomial in (3.6) may suffer from instability when the inverse of the PA model is calculated, therefore, in [86], a set of orthogonal polynomials is proposed to increase the inversion stability. The modified model can be written as:

$$y(n) = \sum_{m=0}^{M} \sum_{k=1}^{N} \sum_{l=0}^{k} \beta_{mk} \, (-1)^{l+k} \, \frac{(k+l)!}{(l-1)!(l+1)!(k-l)!} x(n-m)|x(n-m)|^{l-1} \tag{3.7}$$

Moreover in [87], an improved method called generalized memory polynomial was introduced where positive and negative time-shifts of the signal envelopes are also taken into account as shown in

$$\begin{aligned} y(n) = & \sum_{m=0}^{M} \sum_{k=1}^{N} \alpha_{mk} x(n-m)|x(n-m)|^{k-1} \\ & + \sum_{m=0}^{M_{lag}} \sum_{q=1}^{Q_{lag}} \sum_{k=1}^{N_{lag}} \beta_{mqk} x(n-m)|x(n-m-q)|^{k} \\ & + \sum_{m=0}^{M_{lead}} \sum_{q=1}^{Q_{lead}} \sum_{k=1}^{N_{lead}} \gamma_{mqk} x(n-m)|x(n-m+q)|^{k} \end{aligned} \tag{3.8}$$

where first set of summations correspond to the case of memory polynomial, the second set corresponds to the lagging envelope and the third set shows the leading envelope. There are some other behavioral models such as augmented Hammerstien, augmented Wiener and twin nonlinear box mode [88]- [89]- [90], which are used for mono-band PA modeling. Among all the mono-band models presented in this section, memory polynomial (3.6) is the most suitable one in terms of complexity and performance based on the Figure 11 of [84]. In [91] the baseband and RF nonlinear effects are modeled for wideband direct conversion receivers in the presence of I/Q imbalances where the analysis can be adapted to study mono-band DPDs with I/Q imbalances at the transmitter. In another work [92], a model for a quasi memory-less weakly nonlinear polyphase mixer is proposed, which takes intro account the harmonics and intermodulation products. In the next part, some state of the art multi-band DPDs are described.

3.1.2 Multi-band Band Digital Pre-Distorter (DPD)

In multi-band transmissions PAs nonlinearities and memory effect can be more severe. Due to the presence of other component carriers, inter-modulation products as well as harmonics are expected at the PA output. One proposal could be to consider mono-band DPD for each band which lacks the information about the interaction between the component carriers. Another solution can be considering the whole signal as a wideband signal which is also costly in terms of DAC sampling rate, ADC sampling rate and required memory space. A dual-band memory polynomial DPD is proposed in [93] where PA is linearized around component carriers that are well separated (100 MHz of distance between the component carriers). It takes into account the effects of one component carrier on another but not the intermodulation terms (intermodulation terms are RF filtered in this paper), as shown in (3.9). It shows an ACPR improvment of 13.7 dB with respect to a no-DPD situation for a dual band WCDMA signal of 3.84 MHz. Moreover it was shown that the model reduces the sampling rate by a factor of 27 with respect to a case of conventional mono-band DPD.

$$\begin{aligned} y_1(n) &= \sum_{m=0}^{M}\sum_{k=1}^{N}\sum_{l=1}^{k} \alpha_{mkl} x_1(n-m)|x_1(n-m)|^{k-l}|x_2(n-m)|^{l} \\ y_2(n) &= \sum_{m=0}^{M}\sum_{k=1}^{N}\sum_{l=1}^{k} \beta_{mkl} x_2(n-m)|x_1(n-m)|^{k-l}|x_2(n-m)|^{l} \end{aligned} \tag{3.9}$$

In [94], another dual band model is proposed for the case of closely spaced component carriers (component carriers are 40 MHz apart). It takes into account, for a case of 5^{th} order nonlinearity, in-band intermodulation, cross-term and inter-band intermodulation. These products are strong in the case of closely spaced component carriers. The model

is given in (3.10).

$$\begin{aligned} y_1(n) &= y_1^{(1)}(n) + y_1^{(3)}(n)e^{-j\omega_\Delta nT_s} + y_1^{(5)}(n)e^{-j2\omega_\Delta nT_s} \\ &= \sum_{m=0}^{M-1} x_1(n-m) f_1^{(1)}\left(|x_1(n-m)|, |x_2(n-m)|^2\right) \\ &+ e^{-j\omega_\Delta nT_s} \sum_{m=0}^{M-1} x_1^2(n-m)x_2^*(n-m) f_1^{(3)}\left(|x_1(n-m)|, |x_2(n-m)|^2\right) \\ &+ e^{-j2\omega_\Delta nT_s} \sum_{m=0}^{M-1} x_1^3(n-m)x_2^{*2}(n-m) f_1^{(5)}\left(|x_1(n-m)|, |x_2(n-m)|^2\right) \end{aligned} \tag{3.10}$$

$$\begin{aligned} y_2(n) &= y_2^{(1)}(n) + y_2^{(3)}(n)e^{-j\omega_\Delta nT_s} + y_2^{(5)}(n)e^{-j2\omega_\Delta nT_s} \\ &= \sum_{m=0}^{M-1} x_2(n-m) f_2^{(1)}\left(|x_2(n-m)|, |x_1(n-m)|^2\right) \\ &+ e^{-j\omega_\Delta nT_s} \sum_{m=0}^{M-1} x_2^2(n-m)x_1^*(n-m) f_2^{(3)}\left(|x_2(n-m)|, |x_1(n-m)|^2\right) \\ &+ e^{-j2\omega_\Delta nT_s} \sum_{m=0}^{M-1} x_2^3(n-m)x_1^{*2}(n-m) f_2^{(5)}\left(|x_2(n-m)|, |x_1(n-m)|^2\right) \end{aligned}$$

where:

$$f_1^{(q)}\left(|x_1(n-m)|, |x_2(n-m)|^2\right) = \sum_{k=0}^{N-q}\sum_{l=0}^{k} \alpha_{q,k,l}|x_1(n-m)^{k-l}||x_2(n-m)|^l \ for\ q = \{1,3,5\}$$

$$f_2^{(q)}\left(|x_2(n-m)|, |x_1(n-m)|^2\right) = \sum_{k=0}^{N-q}\sum_{l=0}^{k} \beta_{q,k,l}|x_2(n-m)^{k-l}||x_1(n-m)|^l \ for\ q = \{1,3,5\}$$

$y_1(n)$, $y_2(n)$, $x_1(n)$, $x_2(n)$ are the output and input signals of the first and second component carriers, respectively. Moreover, $y_1^{(1)}$, $y_2^{(1)}$ represent the in-band intermodulation terms and $y_1^{(3)}$, $y_1^{(5)}$, $y_2^{(3)}$, $y_2^{(5)}$ are the inter-band modulation terms for both component carriers. Also $f_1^{(q)}\left(|x_1(n-m)|, |x_2(n-m)|^2\right)$ and $f_2^{(q)}\left(|x_2(n-m)|, |x_1(n-m)|^2\right)$ are the gain functions of the first and second component carriers, respectively. ω_Δ shows the frequency separation between the two component carriers and $()^*$ means the complex conjugate.

The proposed method in (3.10) improves the ACPR of the PA output spectrum by 16

dB compared to the case that no DPD was used. Also it is stated that in closely spaced configurations the proposed model in (3.9) fails to perform properly.

In [95], a dual-band transmitter is linearized in the presence of hardware impairments, such as amplitude and phase imbalance (I/Q imbalance). It proposes a truncated Volterra model and memory polynomial model. The dual-band memory polynomial model with IQ imbalance uses some complex conjugate terms to take into account the image signals due to the imbalances, the model is as follows:

$$\begin{aligned} y_1(n) = &\sum_{m=0}^{M}\left(\sum_{k=0}^{N_1}\sum_{j=0}^{k}\alpha_{q,k,l}^{(1)}x_1(n-m)|x_1(n-m)^{k-j}||x_2(n-m)|^j\right. \\ &\left.+\sum_{k=0}^{N_2}\sum_{j=0}^{k}\beta_{q,k,l}^{(1)}x_1^*(n-m)|x_1(n-m)^{k-j}||x_2(n-m)|^j\right)+d_1 \\ y_2(n) = &\sum_{m=0}^{M}\left(\sum_{k=0}^{N_1}\sum_{j=0}^{k}\alpha_{q,k,l}^{(2)}x_2(n-m)|x_2(n-m)^{k-j}||x_1(n-m)|^j\right. \\ &\left.+\sum_{k=0}^{N_2}\sum_{j=0}^{k}\beta_{q,k,l}^{(2)}x_2^*(n-m)|x_2n-m)^{k-j}||x_1(n-m)|^j\right)+d_2 \end{aligned} \tag{3.11}$$

where $\alpha_{q,k,l}^{(1)}$, $\alpha_{q,k,l}^{(2)}$ are the model coefficients for the component carriers 1 and 2 (the main signals), respectively, and $\beta_{q,k,l}^{(1)}$,$\beta_{q,k,l}^{(2)}$ are the model coefficients for the images of the component carriers 1 and 2. N_1, N_2 and M are the order of nonlinearity for the main and image component carriers and the memory depth, respectively. This model is interesting because it deals with the case of dual-band transmission with I/Q imbalances which can be adapted to our case where we deal with 3 component carriers in the presence of I/Q imbalances. Three component carriers scenario is what we need to focus on. In [96] a three-band PA behavioral model and DPD are proposed that deals with overlap of the intermodulation byproducts with the in-band distortion. Using this model a reduction of more than 15 dB on intermodulation products power level was obtained. In [71], a model is proposed for linearization of a PA with three component carriers without any impairments. It is obtained by development of the three baseband component carriers in

power series of order N. The model is as follows:

$$y_l(n) = \sum_{m=0}^{M}\sum_{i=0}^{N}\sum_{s=0}^{i}\sum_{k=0}^{s} \alpha_{misk}^{(l)} x_l(n-m)|x_1(n-m)^{i-s}| \\ .|x_2(n-m)|^{s-k}|x_3(n-m)|^k \; for\; l = \{1,2,3\} \tag{3.12}$$

Using this model an ACPR improvement of at least of 8.2 dB is obtained for a WCDMA signal of 5 MHz of bandwidth compared to the conventional mono-band memory polynomial (3.6).

The model (3.12) includes only the effect of amplitude of the other component carriers and does take intro consideration the phase variations between the component carriers. Therefore, in [97], a phase aligned-pruned Volterra model is proposed which requires more model coefficients but it shows an ACPR improvement of 2 dB (in average) compared to (3.12).

In normal PAs the bias voltage is fixed but in envelop tracking PA the bias voltage is controlled by an envelop amplifier. This increases the power efficiency for signal with high crest factor. This comes with inherent in-band and cross-band distortions in multi component carrier transmission. Hence the proposed model in [97], is modified to take into account the in-band and cross-band distortions in the case of envelop tracking PA [98]. Moreover, different envelop combinations and envelop mapping are studied where an efficiency improvement as well as lower out-of-band spectral regrowth are reported for average envelop, comparing to the peak envelop, in the case that the envelop is constituted of low-frequency envelops. These enhancements are obtained in the expense of degradation in EVM performance.

In another work [99], a DPD for 3 component carriers is proposed in the case of transmitter leakage in the duplexer of the tranceiver. It suppresses the inter-modulation product for tri-band communications by dividing the model to two basis. The first basis considers a nonlinear function that chooses the frequency band where the inter-modulation products are to be canceled. The second basis considers the envelop dependent nonlinearities. Using this model an IM3 reduction of 20 dB and 25 dB are reported.

3.1.3 DPD Structure

Now that we have seen different behavioral models, we need to find the corresponding DPD to predistort the signal. First option is to find the inverse of the model. In [100] a method, called *pth-order inverse*, is used to find the inverse of a Volterra based model. Unfortunately in the case of high order nonlinearities and wideband signals, the computational cost of this method is very high. A second option is to find the inverse of the signal using a structure which is explained in [101]-[102]. The structure is depicted in Figure 3.2(a) where the DPD coefficients are obtained using an adaptive filter that modifies the values of the DPD to obtain the minimum error ($e(n)$) between the estimated input $\widehat{x(n)}$,which is obtained by the division of the output signal ($y(n)$) by the gain of the PA (G), and the input signal $x(n)$. A third option is to use, so called indirect learning, Figure 3.2(b), because the predistortion coefficients are obtained for a training sequence (it is shown in the figure as post distortion because this step is done after PA) then these coefficients are copied to be used in the DPD [103]-[87].

Another important part of the DPD structure is the estimation algorithm. The mono and multi-band models explained earlier should be written in matrix form to be able to estimate the DPD coefficients properly[1]. Hence N samples of the output signal $\boldsymbol{y(n)}$ are put in a vector of size $P \times 1$ to be used as the training sequence. The estimated coefficient models $\boldsymbol{\omega}$ are stored in another vector of size $R \times 1$. Moreover, the input samples are saved in a matrix $\boldsymbol{Z}$ of size $P \times R$. Output and input samples should be synchronized meaning that the output sample number 1 ($y(1)$) should correspond to the input sample number 1 ($z(1)$) in order to be able to find a proper estimation of the DPD coefficients. The overall model can be written in matrix form as:

$$\hat{\boldsymbol{y}} = \boldsymbol{Z\omega} \tag{3.13}$$

To find the inverse of the model indirectly, Figure 3.2(b), the input and output samples must be swapped ($z(n) \rightleftarrows y(n)$) [87]. Hence, the inverse model can be written as:

$$\hat{\boldsymbol{z}} = \boldsymbol{Y\omega} \tag{3.14}$$

[1]Only indirect learning is explained here because it will be used in our case

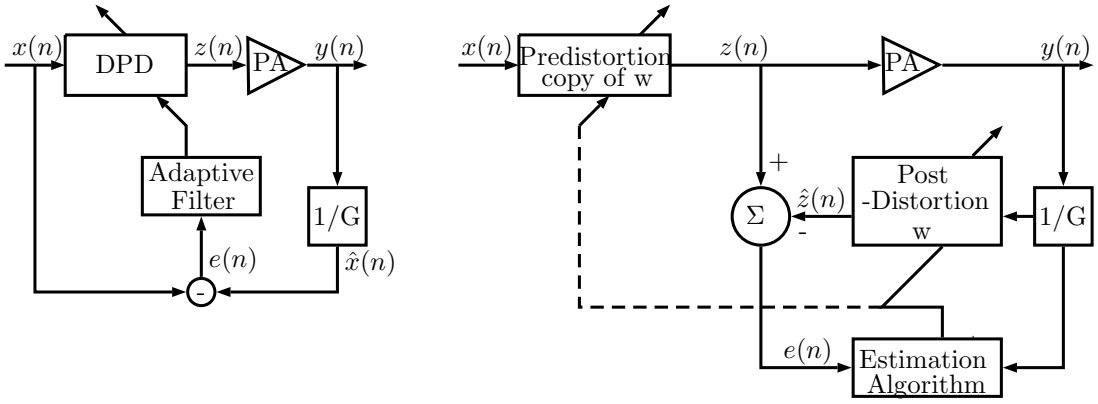

(a) (b)

Figure 3.2: (a) direct learning structure. (b) indirect learning structure

Now we need to minimize the estimation error ($e(n)$), hence:

$$min\left\{e(n)\right\} = min\left\{z(n) - \widehat{z(n)}\right\} \tag{3.15}$$

The error can be minimized using least square (LS) solution, hence the DPD coefficients $\boldsymbol{\omega}$ can be obtained as follows:

$$\boldsymbol{\omega} = \left(\boldsymbol{Y}^H\boldsymbol{Y}\right)^{-1}\boldsymbol{Y}^H\boldsymbol{z} \tag{3.16}$$

where $()^H$ is called Hermetian operator or conjugate transpose. There are many ways to LS solutions, singular value decomposition is used to calculate the LS solution in [104], moreover, MATLAB® uses QR decomposition for linear LS solution [105]. There are two other DPD coefficient estimation algorithms that are proposed in literature, least mean squared (LMS) and recursive least square (RLS). They are both stochastic gradient descent algorithms meaning that they work in a sample by sample basis in each iteration. On the contrary, gradient descent algorithms update the whole training sequence at each iteration, which increases the convergence time. In LMS, an arbitrary initial set for the DPD coefficients is chosen and the algorithm updates it till the estimation error is minimized. LMS uses a single step size parameter for the updates which controls the convergence time of the algorithm, if the parameter is large it converges faster in expense of stability. The detailed conditions on LMS and step size parameter values are given in

[106]. To increase the convergence of the LMS algorithm, RLS algorithm was proposed where it uses same number of parameters (called Kolman gains) as DPD coefficients. It has higher computational compexilty than LMS algorithm because the auto-correlation matrix ($\boldsymbol{Z}$) must be inverted and there are more terms to calculate. The details of RLS algorithms is given in [107].

Now that we saw different models proposed in literature and the algorithms to find DPD coefficients a model is proposed, in the next section, to linearize a tri-band I/Q modulator and compensate its hardware impairments.

3.2 Impairment Compensation of an I/Q Modulator in 3 Component Carrier Transmission Using DPD

The models explained in the introduction section consists of a PA which is used in its nonlinear mode, in contrast to our case where we only use a single I/Q modulator (without PA) to generate carrier aggregated signal. Despite the fact that I/Q modulators are known to be linear, they use mixers to up-convert the signals which have some nonlinear behaviors. Moreover, I/Q imbalances also need to be compensated. These effects are combined and manifest themselves in the form of image signal as was shown in Figure 2.14.

3.2.1 Behavioral Model

In our case, a wide baseband signal is generated, given in (2.19), which consists of three modulated signals at three LIF component carriers (h_1, h_2 and h_3). Then, the baseband signal is up-converted using the carrier signal at f_c. We consider that the in-phase and in-quadrature components of the complex envelop are correctly generated by the DAC and the errors occur in the modulator. Due to the cross modulation terms between the component carriers, a linear model is not suitable and a nonlinear model is needed. Since the LIF signals are superposed to create a single complex envelop, as shown in (2.18), the transmission chain can be modeled using three independent modulators as shown in

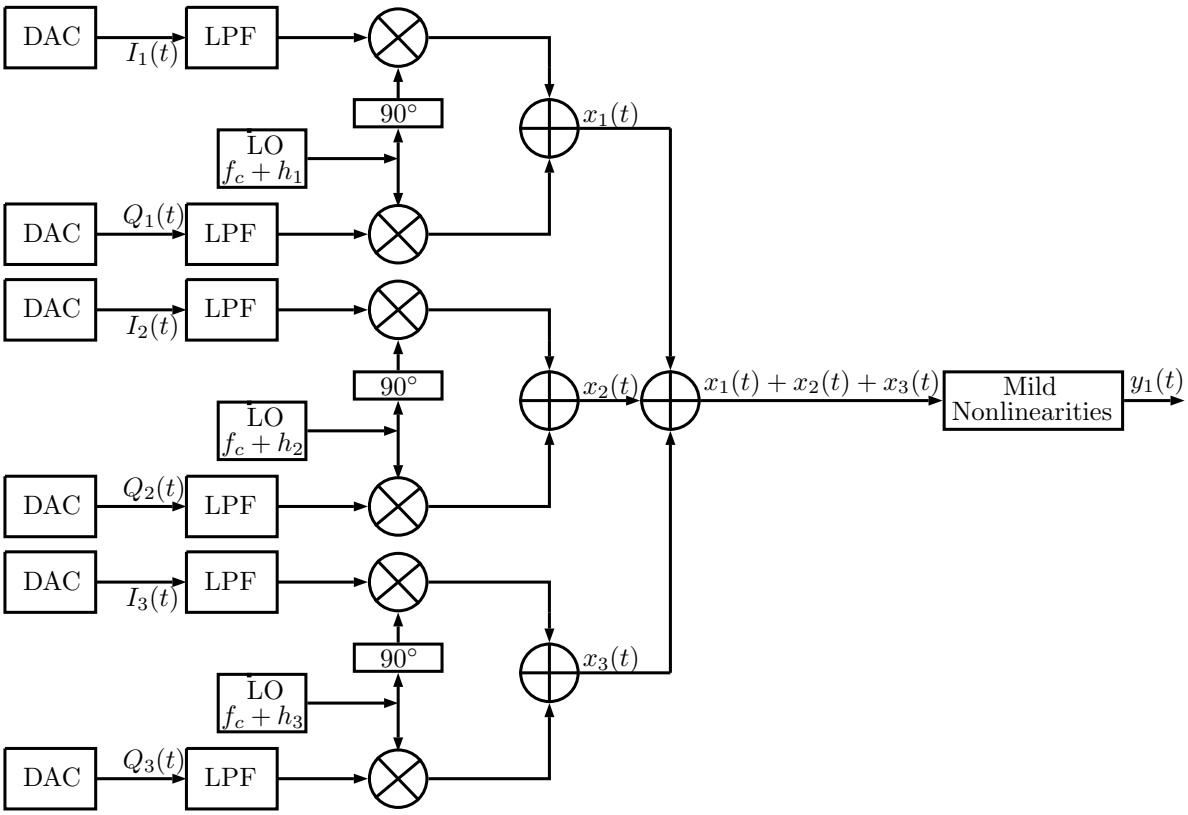

Figure 3.3: I/Q modulator tri-band model structure

Figure 3.3. This model is valid because the components of the I/Q modulator (mixers, phase and power combiner) have different frequency responses at different LIFs. In the presence of I/Q imbalance, the output of each modulator of the model can be written as:

$$x_{cc_k}(t) = Re\left\{ \underbrace{\left[\left(g_k I_k(t) e^{j\theta_k}\right) + j\left(g_{k+1} Q_k(t) e^{j\theta k+1}\right)\right]}_{\widetilde{x_{cc_k}}(t)} e^{2\pi f_k t} \right\} \tag{3.17}$$

$$= g_k I_k(t) cos(2\pi f_k t + \theta_k) - g_{k+1} Q_k(t) sin(2\pi f_k t + \theta_{k+1}) \; for \; k = \{1, 2, 3\}$$

where g_k, g_{k+1}, θ_k and θ_{k+1} are real valued in-phase gain, in-quadrature gain, and phases of the signal in in-phase and in-quadrature paths, respectively. $I_k(t)$ and $Q_k(t)$ are also the in-phase and in-quadrature component of the complex envelop of the baseband signal. Moreover, $\widetilde{x_{cc_k}}(t)$ represents the complex envelop of the signal at the k^{th} component

carrier.

On the other hand, the complex envelop of the k^{th} component carrier $\widetilde{x_{cc_k}}(t)$ can be written in terms of the complex envelop of its corresponding baseband signal $\widetilde{x_k}(t)$, where $\widetilde{x_k}(t) = I_k(t) + jQ_k(t)$, as shown in the following:

$$\begin{aligned}
\widetilde{x_{cc_k}}(t) &= \left(g_k I_k(t) e^{j\theta_k}\right) + j\left(g_{k+1} Q_k(t) e^{j\theta k+1}\right) \\
&= g_k I_k(t) cos(\theta_k) - g_{k+1} Q_k(t) sin(\theta_{k+1}) \\
&+ j\Big(g_k I_k\,(t)\, sin\,(\theta_k) + g_{k+1} Q_k\,(t)\, cos\,(\theta_{k+1})\Big) \\
&= \underbrace{[g_k cos(\theta_k) + g_{k+1} cos(\theta_{k+1})] + j[g_k sin(\theta_k) + g_{k+1} sin(\theta_{k+1})]}_{\beta_k} \widetilde{x_k}(t) \\
&+ \underbrace{[g_k cos(\theta_k) - g_{k+1} cos(\theta_{k+1})] + j[g_k sin(\theta_k) - g_{k+1} sin(\theta_{k+1})]}_{\gamma_k} \widetilde{x_k^*}(t) \\
&= \beta_k \widetilde{x_k}(t) + \gamma_k \widetilde{x_k^*}(t)
\end{aligned} \tag{3.18}$$

Where $()^*$ is the conjugate operator.

A PA behavioral model for communication of 3 concurrent component carriers is proposed in [71], which does not include the I/Q imbalances of the modulator. The model is given in (3.12). However, the model presented in that paper needs to be modified since only even exponents are taken into account in their calculations that are not reflected in their model. Hence, the corrected model is written as:

$$\begin{aligned}
y_l(n) = \sum_{m=0}^{M} \sum_{\substack{i=0 \\ even}}^{N} \sum_{\substack{s=0 \\ even}}^{i} \sum_{\substack{k=0 \\ even}}^{s} \alpha_{misk}^{(l)} x_l(n-m) |x_1(n-m)|^{i-s} \\
.|x_2(n-m)|^{s-k} |x_3(n-m)|^k \; for \; l = \{1,2,3\}
\end{aligned} \tag{3.19}$$

Since we model our system as 3 independent I/Q modulators, Figure 3.3, the model (3.19) can be used to represent the complex envelop of the first component carrier at the output of the I/Q modulator, as shown in the following[2]:

$$\begin{aligned}
\widetilde{y_1}(n) = \sum_{m=0}^{M} \sum_{\substack{i=0 \\ even}}^{N} \sum_{\substack{s=0 \\ even}}^{i} \sum_{\substack{l=0 \\ even}}^{s} \alpha_{misl}^{(1)} \widetilde{x_{cc_1}}(n-m) |\widetilde{x_{cc_1}}(n-m)|^{i-s} \\
.|\widetilde{x_{cc_2}}(n-m)|^{s-l} |\widetilde{x_{cc_3}}(n-m)|^l
\end{aligned} \tag{3.20}$$

[2]The variable k is replaced by l since in our notation we use k as the number of component carrier

where $\alpha_{misk}^{(1)}$ are complex-valued model coefficients of the first component carrier and $\widetilde{x_{cc_k}}(n-m)$ is sampled ($t = nT_s$) complex envelops of the k^{th} component carriers.

By replacing (3.18) in (3.20) we can write:

$$\begin{aligned}
\widetilde{y_1}(n) =& \alpha_{m000}^{(1)}\beta_1\widetilde{x_1}(n) + \alpha_{m000}^{(1)}\gamma_1\widetilde{x_1}^*(n) + \alpha_{m200}^{(1)}\beta_1^2\gamma_1^*\widetilde{x_1}^3(n) + \alpha_{m200}^{(1)}\beta_1^*\gamma_1^2\widetilde{x_1}^{*3}(n) \\
&+ \alpha_{m200}^{(1)}\{\beta_1|\beta_1|^2 + 2\beta_1|\gamma_1|^2\}\widetilde{x_1}(n)|\widetilde{x_1}(n)|^2 + \alpha_{m200}^{(1)}\{\gamma_1|\gamma_1|^2 + 2\gamma_1|\beta_1|^2\}\widetilde{x_1}^*(n)|\widetilde{x_1}(n)|^2 \\
&+ \alpha_{m220}^{(1)}\beta_1\{|\beta_2|^2 + |\gamma_2|^2\}\widetilde{x_1}(n)|\widetilde{x_2}(n)|^2 + \alpha_{m220}^{(1)}\gamma_1\{|\beta_2|^2 + |\gamma_2|^2\}\widetilde{x_1}^*(n)|\widetilde{x_2}(n)|^2 \\
&+ \alpha_{m222}^{(1)}\beta_1\{|\beta_3|^2 + |\gamma_3|^2\}\widetilde{x_1}(n)|\widetilde{x_3}(n)|^2 + \alpha_{m222}^{(1)}\gamma_1\{|\beta_3|^2 + |\gamma_3|^2\}\widetilde{x_1}^*(n)|\widetilde{x_3}(n)|^2 \\
&+ \alpha_{m400}^{(1)}\beta_1^3\gamma_1^{*^2}\{\widetilde{x_1}^5(n) + \alpha_{m400}^{(1)}\gamma_1^3\beta_1^{*^2}\}\widetilde{x_1}^{*^5}(n) \\
&+ \alpha_{m400}^{(1)}\{\beta_1\ |\beta_1|^4 + 6\beta_1\ |\beta_1|^2|\gamma_1|^2 + 3\beta_1|\gamma_1|^4\}\widetilde{x_1}(n)|\widetilde{x_1}(n)|^4 \\
&+ \alpha_{m400}^{(1)}\{\gamma_1|\gamma_1|^4 + 6\gamma_1\ |\gamma_1|^2|\beta_1|^2 + 3\gamma_1|\beta_1|^4\}\widetilde{x_1}^*(n)|\widetilde{x_1}(n)|^4 \\
&+ \alpha_{m400}^{(1)}\{2\beta_1^2\gamma^*|\beta_1|^2 + 3\beta_1^2|\gamma_1|^2\gamma_1^*\}\widetilde{x_1}^3(n)|\widetilde{x_1}(n)|^2 \\
&+ \alpha_{m400}^{(1)}\{2\gamma_1^2\beta^*|\gamma_1|^2 + 3\gamma_1^2|\beta_1|^2\beta_1^*\}\widetilde{x_1}^{*^3}(n)|\widetilde{x_1}(n)|^2 \\
&+ \alpha_{m420}^{(1)}\beta_1^2\gamma_1^*\{|\beta_2|^2 + |\gamma_2|^2\}\widetilde{x_1}^3(n)|\widetilde{x_2}(n)|^2 \\
&+ \alpha_{m420}^{(1)}\gamma_1^2\beta_1^*\{|\beta_2|^2 + |\gamma_2|^2\}\widetilde{x_1}^{*^3}(n)|\widetilde{x_2}(n)|^2 \\
&+ \alpha_{m442}^{(1)}\beta_1\{|\beta_2|^2 + |\gamma_2|^2\}\{|\beta_3|^2 + |\gamma_3|^2\}\widetilde{x_1}(n)|\widetilde{x_2}(n)|^2|\widetilde{x_3}(n)|^2 \\
&+ \alpha_{m442}^{(1)}\gamma_1\{|\beta_2|^2 + |\gamma_2|^2\}\{|\beta_3|^2 + |\gamma_3|^2\}\widetilde{x_1^*}(n)|\widetilde{x_2}(n)|^2|\widetilde{x_3}(n)|^2 + \dots
\end{aligned} \tag{3.21}$$

The sequence in (3.21) can be rewritten intuitively in (3.22) to show the complex envelop output model of the tri-band I/Q modulator in the presence of I/Q imbalances.

$$\begin{aligned}
\widetilde{y_1}(n) = \sum_{m=0}^{M}\sum_{i=0}^{N_1}\sum_{s=0}^{i}\sum_{l=0}^{s}\Big(& h_{misl}^{(1)}\widetilde{x_1}(n)|\widetilde{x_1}(n)|^{i-s}|\widetilde{x_2}(n)|^{s-l}|\widetilde{x_3}(n)|^l \\
&+ q_{misl}^{(1)}\widetilde{x_1}^*(n)|\widetilde{x_1}(n)|^{i-s}|\widetilde{x_2}(n)|^{s-l}|\widetilde{x_3}(n)|^l\Big) + C_1
\end{aligned} \tag{3.22}$$

The complex envelop around the two other component carriers are deduced in the same way and are presented as follows:

$$\widetilde{y_2}(n) = \sum_{m=0}^{M}\sum_{i=0}^{N_1}\sum_{s=0}^{i}\sum_{l=0}^{s}\Big(h_{misl}^{(2)}\widetilde{x_2}(n)|\widetilde{x_2}(n)|^{i-s}|\widetilde{x_1}(n)|^{s-l}|\widetilde{x_3}(n)|^{l} + q_{misl}^{(2)}\widetilde{x_2}^{*}(n)|\widetilde{x_2}(n)|^{i-s}|\widetilde{x_1}(n)|^{s-l}|\widetilde{x_3}(n)|^{l}\Big) + C_2 \tag{3.23}$$

$$\widetilde{y_3}(n) = \sum_{m=0}^{M}\sum_{i=0}^{N_1}\sum_{s=0}^{i}\sum_{l=0}^{s}\Big(h_{misl}^{(3)}\widetilde{x_3}(n)|\widetilde{x_3}(n)|^{i-s}|\widetilde{x_1}(n)|^{s-l}|\widetilde{x_2}(n)|^{l} + q_{misl}^{(3)}\widetilde{x_3}^{*}(n)|\widetilde{x_3}(n)|^{i-s}|\widetilde{x_1}(n)|^{s-l}|\widetilde{x_2}(n)|^{l}\Big) + C_3 \tag{3.24}$$

In (3.22), (3.23) and (3.24) $h_{misl}^{(k)}$, $q_{misl}^{(k)}$ and C_k, for $k = \{1, 2, 3\}$, are the coefficient of the model, the coefficient of the conjugate part of the model and the DC values, respectively. The proposed model does not include intermodulation terms because our system is mildly nonlinear where these terms do not have any sensible effect.

Now that we obtained the behavioral model of the I/Q modulator, in the next section, we estimate the DPD coefficient of this model.

3.2.2 DPD Design

Indirect learning was used as depicted in Figure 3.4(b). The samples of the output complex envelop $\widetilde{y_k}(n)$ are stored in a $P \times 1$ vector $\hat{\tilde{\boldsymbol{y}}}$. The input terms of the model and their conjugates are stored in two $P \times R$ matrices $\widetilde{\boldsymbol{X_{in}}}$ and $\widetilde{\boldsymbol{X_{in}}}^{*}$. Finally, their corresponding model coefficients are stored in two $R \times 1$ vectors $\boldsymbol{h}$, $\boldsymbol{q}$, respectively. (3.22) can be written in matrix form as shown in (3.25). (3.23) and (3.24) matrix forms are similar.

$$\begin{aligned}\hat{\boldsymbol{y}} &= \boldsymbol{h}\widetilde{\boldsymbol{X_{in}}} + \boldsymbol{q}\widetilde{\boldsymbol{X_{in}}}^{*} \\ &= \underbrace{\begin{bmatrix}\widetilde{\boldsymbol{X_{in}}} & \widetilde{\boldsymbol{X_{in}}}^{*}\end{bmatrix}}_{\widetilde{\boldsymbol{X}}} \underbrace{\begin{bmatrix}\boldsymbol{h} \\ \boldsymbol{q}\end{bmatrix}}_{\boldsymbol{\omega}} \\ \hat{\tilde{\boldsymbol{y}}} &= \widetilde{\boldsymbol{X}}\boldsymbol{\omega}\end{aligned} \tag{3.25}$$

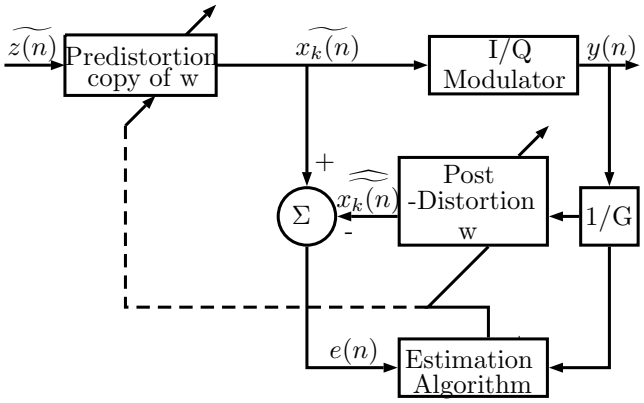

Figure 3.4: Indirect learning structure of the DPD

As explained in 3.1.3 the input and output samples are swapped ($\widetilde{x_k}(n) \rightleftarrows \widetilde{y_k}(n)$), and the inverse model is written as:

$$\hat{\tilde{\boldsymbol{x}}} = \widetilde{\boldsymbol{Y}}\boldsymbol{\omega} \tag{3.26}$$

An error is calculated from the transmitted and the estimated samples inputs, as shown below:

$$e(n) = \tilde{x}(n) - x(n) \tag{3.27}$$

To minimize the error, least square algorithm is applied where the optimal DPD coefficients are using (3.28):

$$\boldsymbol{\omega} = \left(\tilde{\boldsymbol{Y}}^H \tilde{\boldsymbol{Y}}\right)^{-1} \tilde{\boldsymbol{Y}}^H \tilde{\boldsymbol{x}} \tag{3.28}$$

In the next section, simulation and experimental results of the proposed model are given.

3.3 Simulation and Experimental Results

In this section, the test configurations as well as the results of DPD application in simulation and experiments are presented. 2048 symbols are generated as 698880 samples ($OSR = 336$) for each of the three component carriers with the specifications given in Table 3.1. They are generated using AWG7122b Tektronix arbitrary waveform generator (in LI frequency) and up-converted using the I/Q modulator depicted in Figure 2.15(a). The test bench with the transmitter and receiver is shown in Figure 3.5. At the receiver,

an application FSW R&S named I/Q Analyzer is in charge of down-conversion and sampling of the received signal using the internal mono-band demodulator and ADC of the FSW. This application does not do any signal processing, it only stores the samples in a file in order to be processed by MATLAB® or other digital signal processing tools. The received component carriers are down-converted one-by-one and sampled at a rate of 80 Ms/s. 50000 samples are stored for each component carriers which are used as data of the complex envelops of the received signals $\widetilde{y_1}(n)$, $\widetilde{y_2}(n)$ and $\widetilde{y_3}(n)$.

RF Frequency	$f_1 = 2.2$ GHz	$f_2 = 2.5$ GHz	$f_3 = 2.9$ GHz	$f_c = 2.52$ GHz
LI Frequency	$h_1 = -320$ MHz	$h_2 = -20$ MHz	$h_3 = 380$ MHz	$\eta = 30$ MHz
Power	-42 dBm	-42 dBm	-42 dBm	10 dBm
Bandwidth	10 MHz	10 MHz	10 MHz	–
Sampling rate	3.36 GHz	3.36 GHz	3.36 GHz	–
Modulation	QPSK-OFDM			CW
N	32			–
L	8			–
DC-Null Subcarrier	✓			–
TS	CAZAC			–

Table 3.1: Specification of the carrier aggregated signal

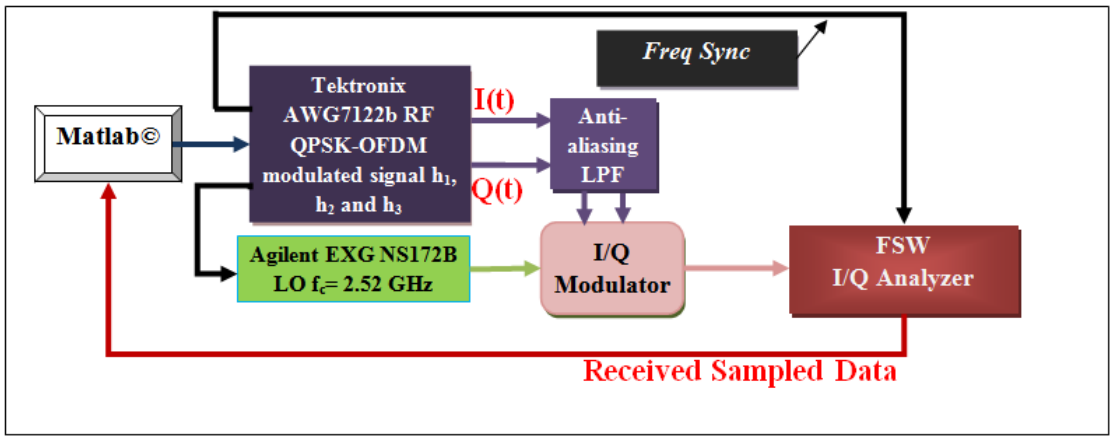

Figure 3.5: DPD Test bench

The input sample of each component carrier is decimated by a factor of 42 so that its sampling rate corresponds to the sampling rate of the receiver (80 Ms/s). The time synchronization process as explained in section 2.6.1 is performed to ensure that each output sample corresponds to its initial input samples and not others. Moreover, 31 samples are added to the end of the initial samples due to the FIR filter delays (a raised cosine filter with a roll-off factor of 0.35 is used) which should be removed from the samples. The first 500 samples of the synchronized input and output samples are plotted in Figure 3.6. The plot shows the output waveform (red line) distortion with respect to the input waveform (blue line).

Remark 3.2. Different pulse shaping filters are used in wireless communication. In our application we used a raised cosine filter, because it is only required at the transmitter and no pulse shaping filter is needed at the receiver. On the other hand, if root raised cosine filter was used, it should have been applied at the transmitter and receiver, hence complexity is increased.

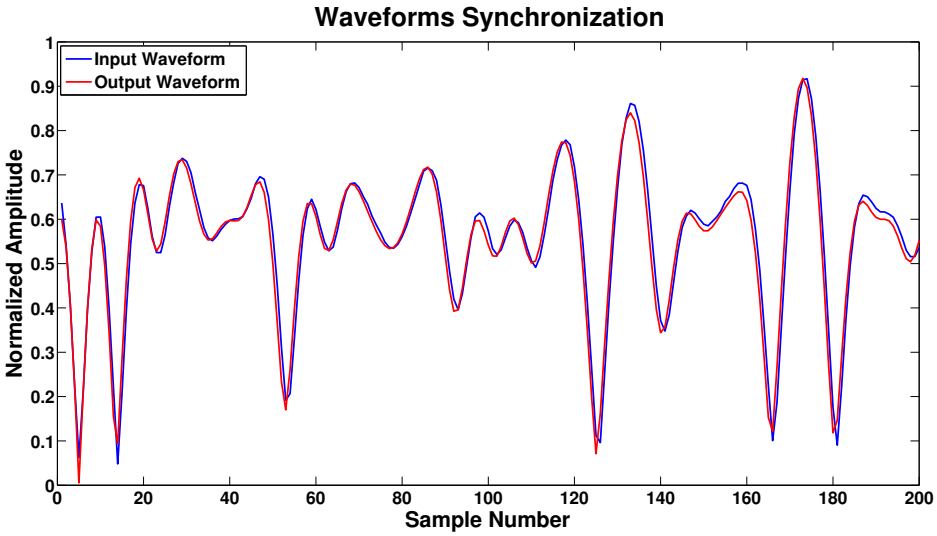

Figure 3.6: DPD Test bench

Using the input and output samples of the first component carrier, its behavioral model in (3.22) is built in a matrix form as given in (3.25). In our experiment, we

took all the decimated input samples, including the CAZAC traning sequence. However, using a portion of it as training block is also possible.[3]The DPD coefficients are estimated as explained in section 3.2.2. Once DPD coefficients are obtained, they are fed to the model (in MATLAB®) to observe the distortion reduction at the output of the model. The mean-squared error (MSE) between the output and the input samples without any DPD is 13×10^{-4} . Table 3.2 shows the MSE of different DPD configurations. We took nonlinearity order of 3 since our modulator is mildly nonlinear. The best performance

M	0	1	2	3	4	5
MSE	1.6×10^{-4}	1.3×10^{-4}	4×10^{-7}	2.4×10^{-6}	1.1×10^{-6}	8.1×10^{-7}

Table 3.2: mean-squared error in function of the memory depth for N=3

is obtained for memory depth of 2 where an improvement in MSE by a factor of 3250 is obtained in comparison to the case where no DPD is used. Figure 3.7 depicts the normalized AM-AM curves of the case without DPD (red dots) and the case with DPD (N = 3, M = 2) (blue dots) which give a graphical insight about the enhancement obtained by DPD. The red dots are obtained by measured output samples and the blue dots are obtained by the samples that passed through the behavioral model in MATLAB®. We observe the memory effect compensation by the fact that the DPD curve is much more concentrated than the curve without DPD.

Figure 3.8 shows the PSD of the output signal of the modulator without applying the DPD. The component carriers and their corresponding images are shown with the same color. After finding the behavioral model and creating the DPD signal, the DPD baseband signal is imported to AWG7122b Tektronix to see its performance in practice. Moreover, no carrier feedthrough cancellation was performed at the input of the modulator using polarization Tees, hence carrier feedthrough exists while modeling. Figure 3.8(a),(b) and (c) show 20 dB, 3 dB and 5 dB reduction of the image signal

[3]The training block should not be mistaken with the CAZAC training sequence that is used for time synchronization.

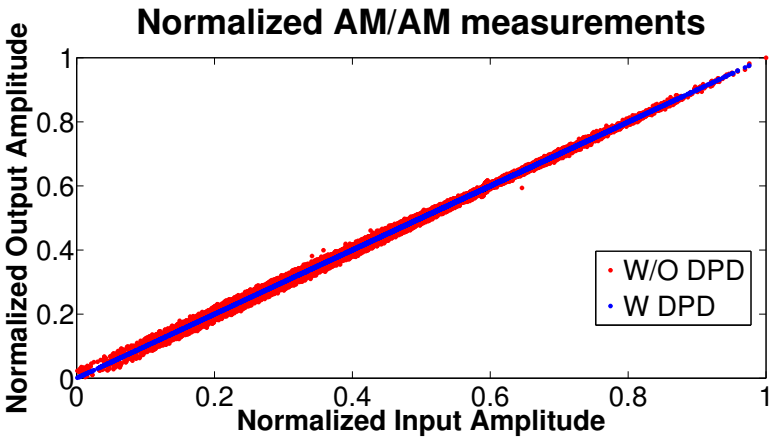

Figure 3.7: Normalized AM/AM Plots

levels,respectively , after applying the DPD (red lines). Furthermore, Figure 3.8(d) and (f) show that the DPD has not changed the spectrum of the first and third component carriers. On the other hand, a spectral regrowth is observed in Figure 3.8(e) which is due to the fact that the carrier feed-through plays role of the blocker for the model which led to erroneous calculation of the DPD coeeficients for the second component carrier

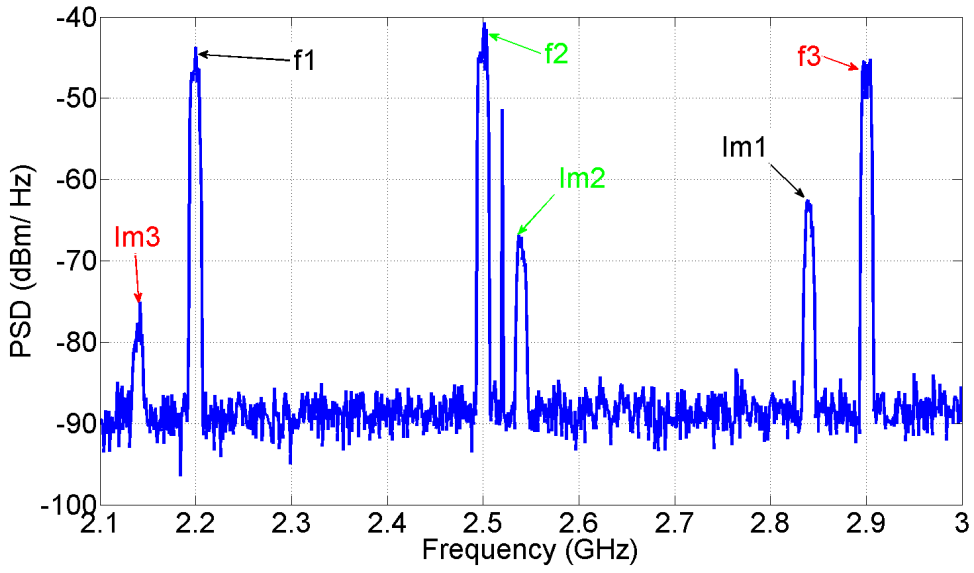

Figure 3.8: PSD of the I/Q Modulator output signal without DPD

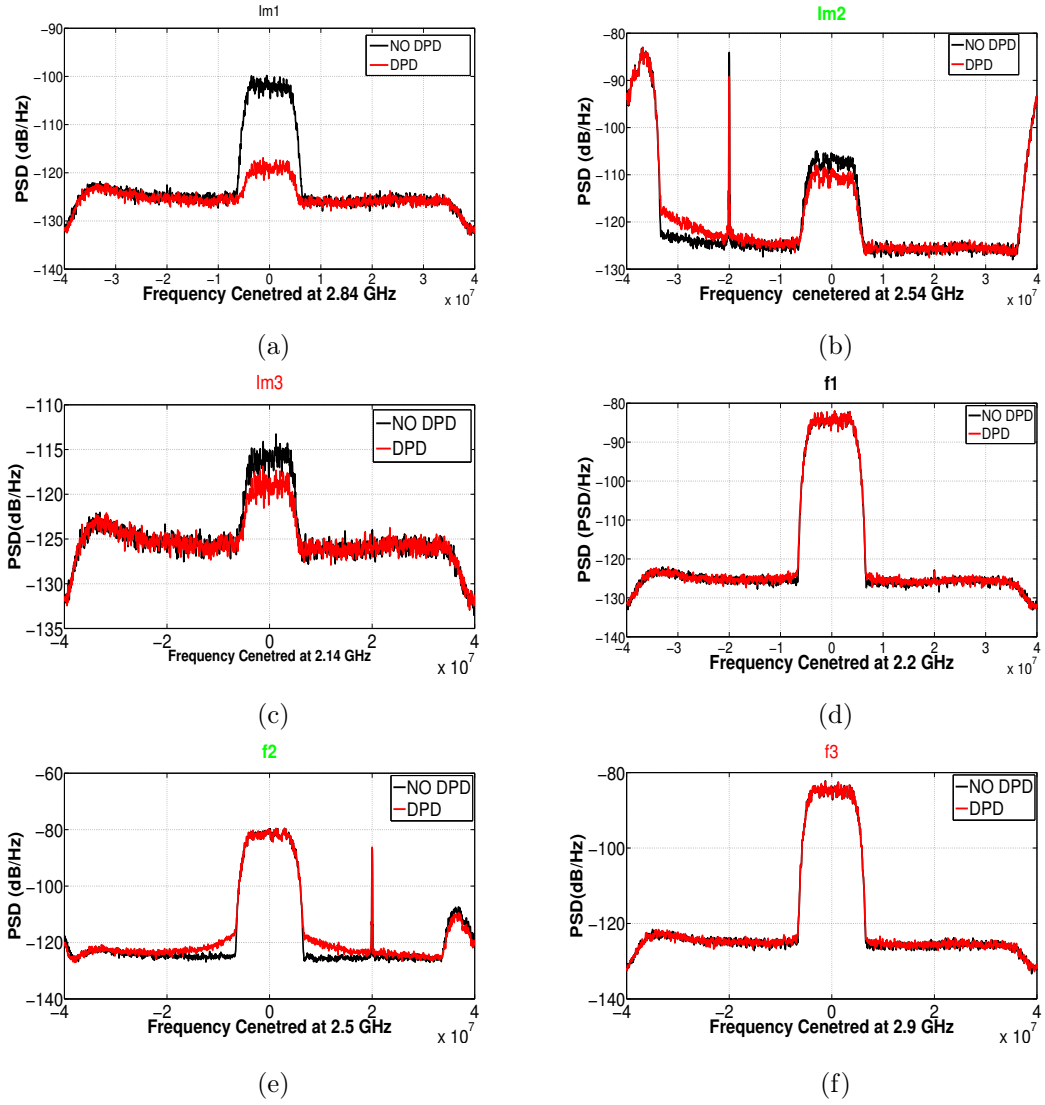

Figure 3.9: Spectral regrowth cancellation with DPD (a) Im1 @ 2.84 GHz (b) Im2 @ 2.54 GHz (c) Im3 @ 2.14 GHz (c) f1 @ 2.2 GHz (b) f2 @ 2.5 GHz (b) f3 @ 2.9 GHz

3.4 Conclusion

In this chapter, linearization methods for power amplifiers and I/Q modulators were presented, moreover the impairment compensation of I/Q modulators were also proposed. Behavioral modeling was chosen as the best linearization solution where firstly, mono-band cases were studied and then multi-band PAs and I/Q modulators were presented. We proposed a behavioral model for linearization and impairment compensation of an I/Q modulator which generates three component carriers. Moreover, a digital predistorter was used, based on indirect learning, which performed as the "inverse" of the behavioral model. Finally, simulation results which showed the reduction of the distortion at the output of the I/Q modulator were given. The implementation of the DPD was explained and the PSD of the I/Q modulator was obtained which suffered from spectral regrowth due to phase discontinuity that happens at our arbitrary waveform generator.

Conclusion and Perspectives

Conclusion

During this dissertation, different aspects of RF communications were studied and developed. It focused on LTE and LTE-A communications that are widely used in 4G technology and beyond. To increase the data rate in the dense RF spectrum, 3GPP proposed a concept to use multiple carriers, simultaneously, on different parts of the spectrum. This concept is called carrier aggregation (CA). Multi-carrier (multi-band) communications have some difficulties regarding the interactions among different bands, the excessive use of equipment and the performance quality of these equipment. This thesis explored these different problems and tried to bring some solutions.

In the first chapter, the thesis demonstrates that n LO devices can be replaced by one LO device, 2 DACs and one I/Q modulator. Both DACs are used to generate the complex envelop of a multi-tone LIF signal where the tones are distributed over positive and negative LIF. In that way a factor of two is obtained in the reduction of the frequency sample of the DACs. It was shown that the amplitude of each tone was digitally controllable. Moreover, practical considerations as well as physical impairments of the system such as I/Q imbalances and carrier feed-through were studied and analyzed. The structure was simulated in Matlab environment and implemented in experiment. The structure was implemented and SFDRs of 52 dB and 50 dB were obtained for 3-tone and a 4-tone signal, respectively. This multi-tone LO signal is used as a CA solution in a

LTE-A TPD receiver, to down-convert, at the same time, all the component carriers of the transmitted CA signal. Using this structure, multiple transmission chains (DAC, I/Q Modulator and LO) are replaced by one. Finally, we showed that the DAC sampling rate is much lower in our structure than the case where the signal is directly synthesized from baseband to RF using high performance DACs. Based on Nyquist criterion to synthesize a signal, the sampling rate must be at least twice of its highest frequency component. Hence, to directly synthesize a multitone signal at 2.00 GHz, 2.03 GHz and 2.07 GHz a sampling rate of 4.14 Gs/s is required, whereas in our structure the same signal generated with a sampling rate of 135 Ms/s.

In the second chapter, we focused on LTE-A transmitter and adapted the structure of chapter one to transmit different symbols over different component carriers instead of having multi-tone CW signals. At first, the OFDM signal modulation and demodulation process as well as their practical considerations were explained. Then, a frequency diversity solution was proposed where identical OFDM symbols were transmitted over different component carriers. The structure was further developed to transmit different OFDM symbols over 3 component carriers, which is required in LTE-A transmitter. The structure can be adapted to the case of n component carriers by modifying the mathematical development of the complex envelop signal. Using our method the component carriers of the LTE-A signal were generated at negative and positive low intermediate frequencies by two DACs and up-converted using a single I/Q modulator and a LO signal. Similar to the multi-tone case this structure requires lesser equipment, because one transmission chain is used for all of the component carriers. It, also, reduces the DAC sampling rate with respect to the direct baseband-RF signal generation. We showed that to generate 3 component carriers at 2.2 GHz, 2.5 GHz and 2.9 GHz a sampling rate of 1.14 Gs/s is required using our structure, whereas in direct baseband-RF synthesis a sampling rate of at least 5.8 Gs/s is needed. Moreover, I/Q imbalances and carrier feed-through were studied and a look-up table impairment compensation solution was proposed. Finally, the demodulation of the signals was explained in details, using a multi-band demodulator called TPD. The signals were also demodulated using a commercial mono-band vector

signal analyzer (VSA) and their results were compared. An ACLR of 43 dB was obtained with our structure, moreover, an EVM of -28 dB was obtained by the VSA demodulator for a 64-QAM signal at -42 dBm.

In the third chapter, the system functionality was studied to compensate for its impairments using predistortion techniques. We modeled the system using the output and input samples without going into the detailed circuitry of each component of the system. This method is called behavioral modeling. We proposed a behavioral multi-band model to cover the mild nonlinearities of the I/Q modulators in the presence of the impairments. Moreover, the "inverse" of the model was obtained using indirect learning and least square algorithm. The inverse signal, DPD signal, is fed to the modulator to linearize and correct its output. Simulation and experimental results were presented to confirm the functionality of the model. Simulations showed that with a memory depth of 2 and a nonlinearity order of 3, an enhancement of 3250 is obtained in mean squared error of the output signal with respect to the case where no DPD is used. Moreover, we obtained, by measurement, a 20 dB signal rejection on the image signals.

Perspectives

There are some aspects of this work that one should shed lights on. New CA configurations need to be implemented and evaluated. For instance, component carriers with different bandwidths and different modulations need to be implemented. These combinations can be sensitive since, the designer needs to make sure to have same number of samples at each component carrier. Moreover, the signal generation structure was implemented using arbitrary waveform generator, it should be also implemented using a field programmable gate array (FPGA) to be used in real time applications. On the other hand, the performance of our DPD needs to be studied in the presence of a multi-band power amplifier (the case with strong nonlinearities). Furthermore, DPD performance needs to be improved by making several iterations of the DPD coefficient calculations. Moreover, the performance and the stability of the DPD in long time intervals and different temperatures need to be studied. CA is a powerful tool that can be used in

different technologies such as 5G [108]. In 5G the component carrier bandwidths are much higher than LTE-A, hence, new DPD structures need to be developed to take into account the very large bandwidth of the component carriers. Moreover, other types of waveforms are proposed for 5G [109] such as filter bank multi-carrier (FBMC), universal filtered multi-carrier (UFMC), Generalized Frequency Division Multiplexing (GFDM) and filtered OFDM (F-OFDM) which need to be implemented in our structure, too.

Appendix II: Anti-Aliasing Filter

A post-DAC anti-aliasing filter is a low-pass filter which removes the Nyquist components at the output of DAC. In our case, a third order Chebyshev low-pass filter with a cut-off frequency at 550 MHz was designed and implemented in micro-strip technology using Advanced Design System (ADS) software. The third order filter schematics is depicted in Figure A2.1.

The filter is also designed for a micro-strip with an FR-4 epoxy substrate. Its relative

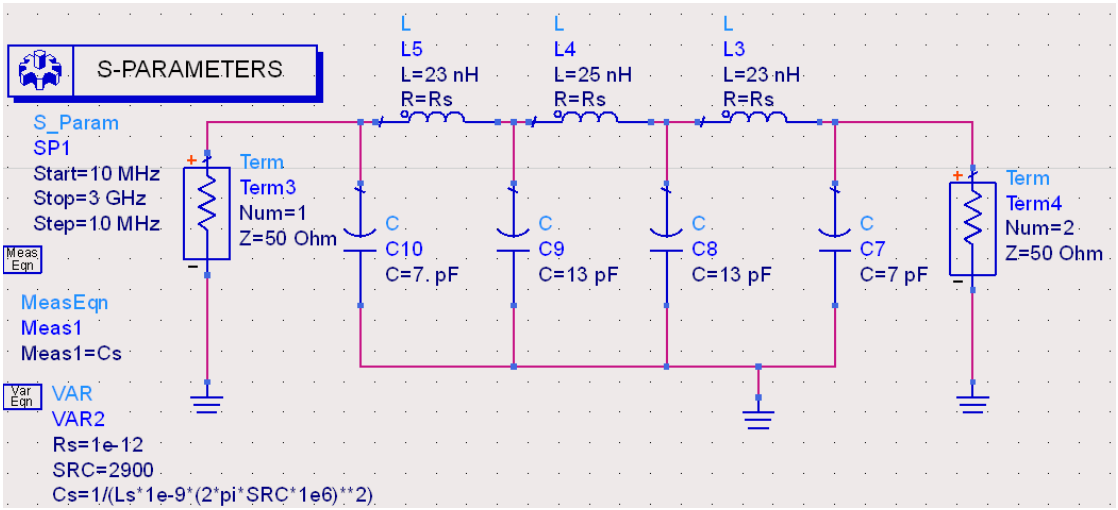

Figure A2.1: Schematics of a third order LPF

dielectric constant is (ϵ_r) is 4 and it has 1.59 mm of thickness. The schematics is given in Figure A2.2.

Figure A2.3 shows the magnitude of the parameter S(2,1), in dB, of the filter of regular

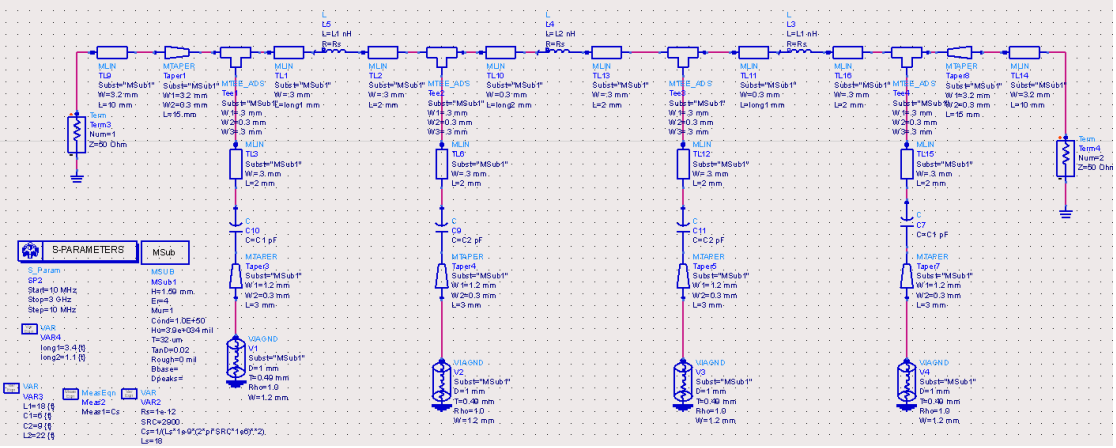

Figure A2.2: Schematics of a third order LPF in micro-strips technology

Chebyshev (pink curve with a zoomed representation in sky blue) and its micro-strip counterpart (red curve with a zoomed representation in blue). The cut-off frequency is at 550 MHz. Moreover, 4 of these filter are built for the 4 output of the DAC (I,$\bar{I}$, Q, $\bar{Q}$) using the Layout given in Figure A2.4. Finally, all designs and components are available in the following link: http://s000.tinyupload.com/?file_id=06891166732787653485

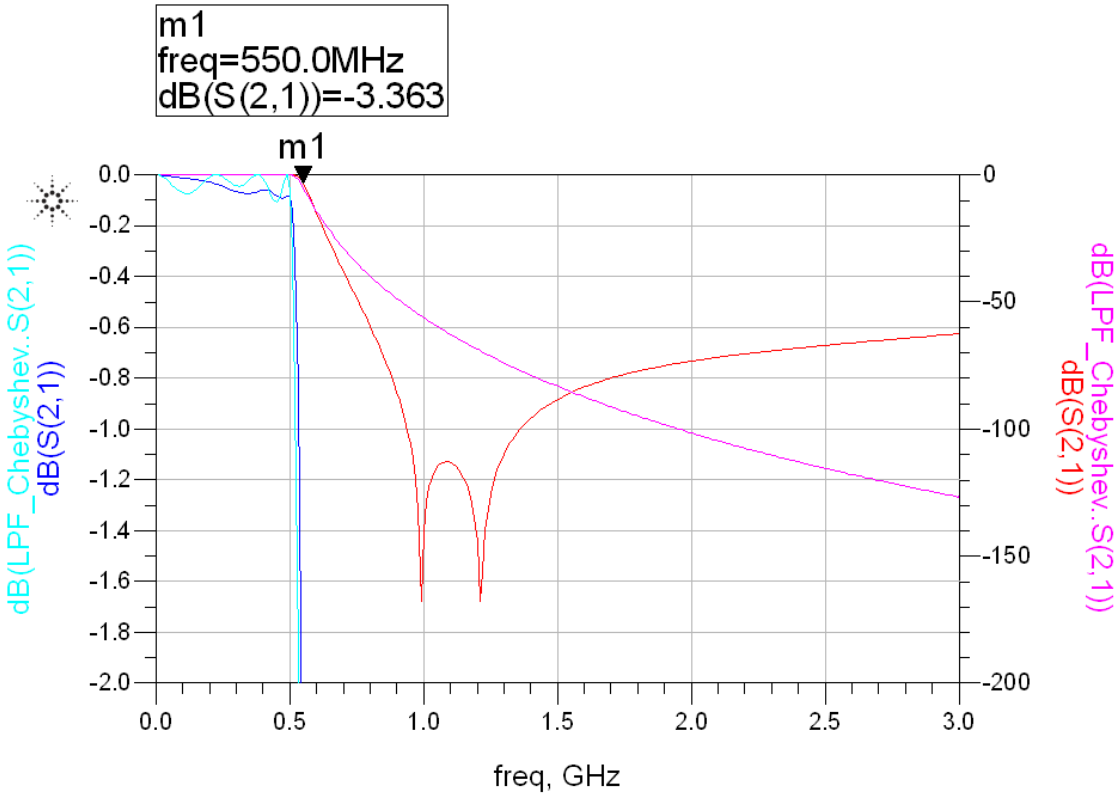

Figure A2.3: Filter gain as S(2,1) parameter

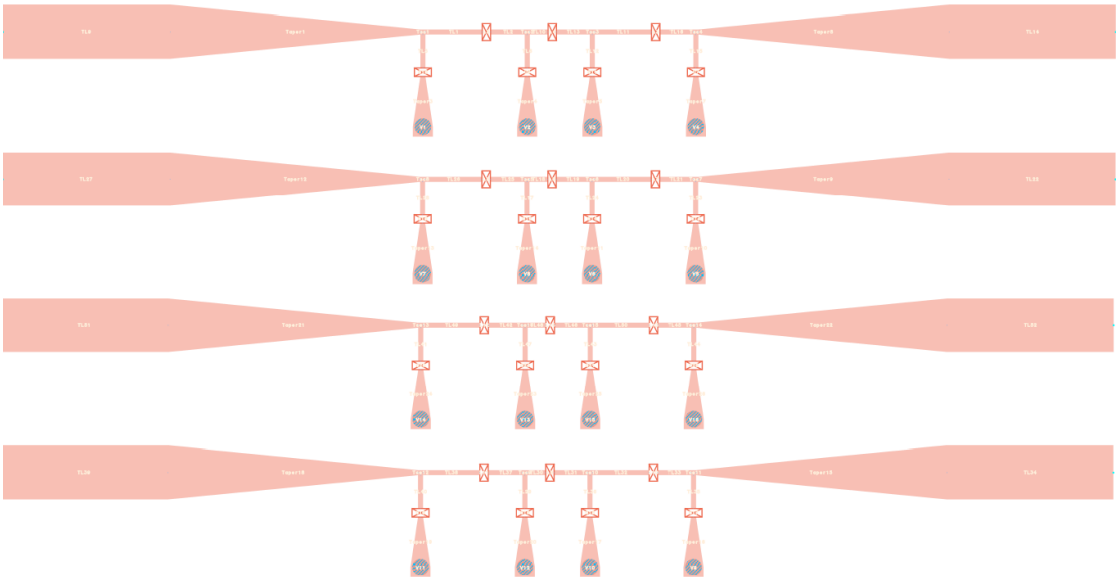

Figure A2.4: Filters layout

Appendix III: Three-Phase Demodulator

A Three-Phase Demodulator (TPD) is an enhanced five -port demodulator where the power detectors are replaced by mixers for signal down-conversion. The use of mixers increase the sensitivity, because they have small compression gain (in passive mixers) and some conversion gains (in active mixers). The detailed description of TPD is given in [110]. The general structure of the TPD is shown in Figure A3.1. RF CA signal passes through a division-by-three power splitter. $\boldsymbol{B_3}$, $\boldsymbol{B_4}$, $\boldsymbol{B_5}$, $\boldsymbol{\gamma_3}$, $\boldsymbol{\gamma_4}$ and$\boldsymbol{\gamma_5}$ are the amplitude and phase of the loss of the power splitter outputs. To perform the down-conversion CA LO signal passes through a division-by-three power splitter. $\boldsymbol{A_3}$, $\boldsymbol{A_4}$, $\boldsymbol{A_5}$, $\boldsymbol{\varphi_3}$, $\boldsymbol{\varphi_4}$ and $\boldsymbol{\varphi_5}$ are the amplitude and phase of the loss of the power splitter outputs. $v_3(t)$, $v_4(t)$ and $v_5(t)$ are the outputs of the demodulator. In [110], the TPD outputs are given in the function of in-phase ($I(t)$) and in-quadrature ($Q(t)$) components of the complex envelop as:

$$\begin{bmatrix} \tilde{v}_3(t) \\ \tilde{v}_4(t) \\ \tilde{v}_5(t) \end{bmatrix} = \begin{bmatrix} S_3 & L_3 cos(\phi_3) & L_3 sin(\phi_3) \\ S_4 & L_4 cos(\phi_4) & L_4 sin(\phi_4) \\ S_5 & L_5 cos(\phi_5) & L_5 sin(\phi_5) \end{bmatrix} \cdot \begin{bmatrix} n(t) \\ I(t) \\ Q(t) \end{bmatrix} \tag{A3.1}$$

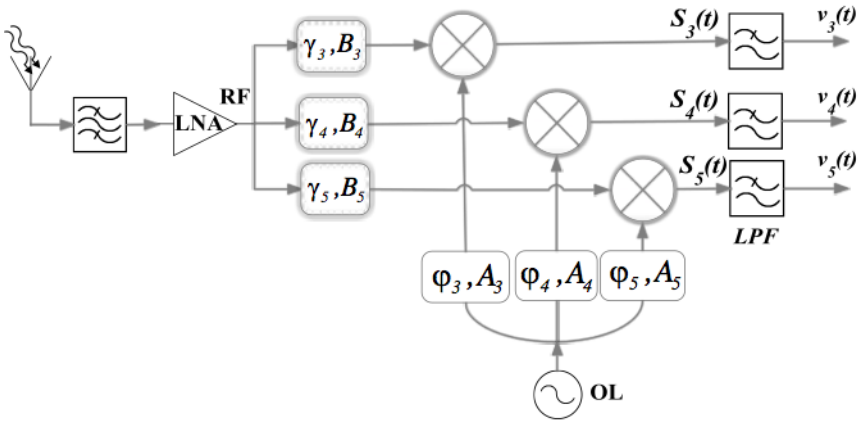

Figure A3.1: TPD structure

where $\tilde{v}_k$, L_k, ϕ_k for $k = \{4, 5, 6\}$ are the alternative part of TPD outputs, magnitude overall conversion coefficient of TPD and phase difference between RF and LO input phases. $I(t)$ and $Q(t)$ can be extracted from (A3.1) as follows:

$$\begin{aligned} I(t) &= t_I \tilde{v}_3 + l_I \tilde{v}_4 + s_1 \tilde{v}_5 \\ Q(t) &= t_Q \tilde{v}_3 + l_Q \tilde{v}_4 + s_Q \tilde{v}_5 \end{aligned} \tag{A3.2}$$

Where t_I, l_I , s_I, t_Q, l_Q and s_Q are the calibration coefficients to be found. If v_3 and v_5 are in symmetry with respect to v_4, then the number of ADC is reduced from 3 to 2 [24], therefore:

Symmetrical amplitudes:

$$A_3 = A_5 \ , \ B_3 = B_5 \tag{A3.3}$$

Symmetrical phases:

$$\phi_3 = \theta + C \ , \ \phi_4 = C \ , \ \phi_5 = \theta - C \tag{A3.4}$$

where C is any arbitrary constant phase that is chosen to be zero. After some mathematical developments, shown in [110], in-phase $I(t)$ and in-quadrature $Q(t)$ component of the signal complex envelop is given as:

$$\begin{aligned} I(t) &= \mu_I \left[-v_3(t) + 2v_4(t) - v_5(t) \right] = \mu_I P_I(t) \\ Q(t) &= \mu_Q \left[v_3(t) - v_5(t) \right] = \mu_Q P_Q(t) \end{aligned} \tag{A3.5}$$

where

$$\mu_I = \frac{1}{2L_3}\frac{1}{1-cos(\theta)}\ ,\ \mu_Q = tan\left(\frac{\theta}{2}\right)\mu_I$$

The operations in (A3.5) are performed using I/Q regeneration circuit that consists of simple operational amplifiers to perform addition and subtraction, as shown in Figure A3.2.

$P_I(t)$ and $P_Q(t)$ are sampled using two ADCs and $I(t)$, $Q(t)$ are obtained digitally

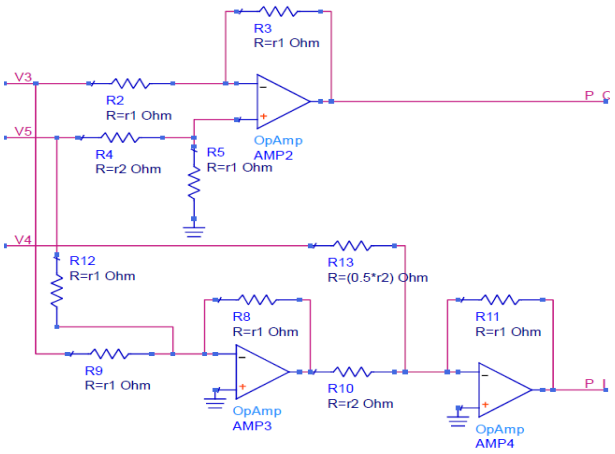

Figure A3.2: I/Q regeneration circuit

using the method explained in section 2.6.1.

Résumé

3 GPP a introduit la norme LTE-Avancé (LTE-A) comme la mise à jour de la norme LTE. Elle a ajouté deux concepts d'agrégation en fréquences des bandes LTE et MIMO (en anglais: Multiple Input Multiple Output) en réponse à l'augmentation exponentiel de demande de débit de données par les utilisateurs du réseau. L'agrégation en fréquences réalise la transmission de données sur plusieurs porteuses, en parallèle, afin de couvrir une bande passante plus large dans le spectre RF qui est lourdement chargé par d'autres applications. Dans ce travail de thèse, on a proposé une structure de génération des signaux multi-porteuse afin de créer plusieurs oscillateurs locaux (OL) tout en utilisant qu'un modulateur I/Q. Ces signaux peuvent être utilisés dans les récepteurs de LTE-A pour la transposition des signaux agrégé en fréquence vers la bande de base.

On développe la structure afin de l'utiliser en émetteur répondant aux normes du standard LTE-A. La nouvelle structure nous permet de générer n signaux agrégés en fréquences, de manière simultanée, par une seule chaine de transmission (c.a.d un modulateur I/Q, un OL). En utilisant cette structure on réduit le nombre de circuits utilisés, en comparaison du cas où n signaux agrégés en fréquences sont générés par n émetteurs. La fréquence d'échantillonnage est réduite dans notre cas par rapport au cas où les signaux sont générés directement de la bande de base à la bande RF avec des convertisseurs analogiques numériques adéquats.

Dans la troisième partie, on se concentre sur les imperfections et les non linéarités du modulateur I/Q dans le cadre de notre structure multi-bande. On modélise le fonctionnement du modulateur multi-bande en utilisant les échantillons en entrée et en sortie. Notre modèle est dérivé de la série de Volterra qui prends en compte les effets non linéaires et les effets mémoires ainsi que les imperfections du modulateur I/Q. Puis, on obtient la fonction "inverse" du modèle et on l'applique à l'entrée du modulateur afin de corriger et linéariser la sortie du modulateur I/Q. La fonction "inverse" est appelée DPD (en anglais: Digital Pre-Distortion). Enfin, on a évalué le modèle et la DPD en simulations et en mesures.

A la fin de ce manuscrit, on décrit la conclusion de ce travail de recherche et les directions à suivre pour les futures recherches dans ce domaine.

Mots-Clés: LTE-A, Agrégation en fréquences, DPD, Modulateur I/Q multi-bande, récepteurs très large bande, OFDM, Effets non linéaires, Effets mémoires

Introduction

De nos jours, les communications ont de nombreuses formes différentes. Les appels vocaux, les SMS et les transmissions de données sont les principales formes utilisées par les utilisateurs. Les objectifs des opérateurs sont : Améliorer la qualité du service et répondre à la demande en croissance exponentielle. Pour des connexions plus rapides et plus fiables, différentes technologies ont été utilisées. De la première génération de communications mobiles où les communications vocales étaient seules possibles, à la quatrième génération de communications mobiles où les appels vidéo de haute qualité deviennent le quotidien des utilisateurs. Ces améliorations sont devenues possibles grâce à l'évolution des structures des émetteurs, récepteurs et des réseaux. Des algorithmes et des techniques de codage plus complexes ont été développés dans les communications numériques. D'autre part, les équipements RF ont été améliorés pour avoir une meilleure performance avec une consommation d'énergie plus faible et une plus grande autonomie. En outre, les communications optiques sont utilisées comme l'épine dorsale du réseau pour la quantité massive de données.

L'un des principaux facteurs permettant d'améliorer le débit de données dans la communication RF est la bande passante. Elle est directement proportionnelle au débit de données des communications. Cependant le spectre RF est très occupé par d'autres utilisateurs et applications. Par exemple, l'application Wi-Fi est transmise sur des bandes de fréquences à 2,4 GHz, 3,6 GHz, 4,9 GHz, 5GHz et 5,9 GHz. Un autre exemple est l'application WiMAX où, comme indiqué dans la norme IEEE 802.16d et 802.16e, les bandes utilisées sont 2,3 GHz, 2,5 GHz, 3,5 GHz et 5,8 GHz. En outre, le spectre est une ressource coûteuse pour les opérateurs de communication, par exemple, les opérateurs français ont payé 2 798 976 324 euros, à titre de redevance, pour les applications LTE dans la bande de 700 MHz, [703 733] MHz et [758 788] MHz [1]. Il est donc très utile d'utiliser tous les petits morceaux du spectre disponibles pour augmenter le débit de données. Cette idée est proposée par le groupe 3GPP pour la norme LTE-A. La technique est appelée agrégation de porteuse (CA).

Pour transmettre des données sur différentes porteuses, simultanément, des émetteurs multi-bandes sont nécessaires. De plus, ces signaux peuvent interagir les uns avec les autres ce qui est une question importante. D'autre part, la transmission de signaux à large bande est

vulnérable aux canaux sélectifs en fréquence, aux effets mémoires dans les amplificateurs de puissance, etc. Dans ce manuscrit de thèse, ces problèmes sont étudiés et quelques solutions sont proposées pour réduire le coût et la consommation des systèmes CA.

Dans le premier chapitre de cette dissertation, une structure est proposée pour les récepteurs CA qui réduit la taille du circuit RF et en particulier le nombre d'oscillateurs locaux (LO). Dans les récepteurs CA, les n bandes de fréquences doivent être transposées en basses fréquences intermédiaires (LIF). Ensuite, les signaux de fréquence (LIF) doivent être échantillonnés par le convertisseur analogique-numérique (ADC). Ceci est habituellement effectué en utilisant n LO différents. La structure proposée consiste en un unique circuit générant un signal multi-tons, composé de multiples signaux de fréquence fixe CW, en utilisant un signal LIF particulier, un modulateur I / Q et un seul oscillateur local (LO). Le signal LIF est obtenu à partir d'expressions mathématiques originales, créés à l'aide de MATLAB®, et de 2 convertisseurs numériques-analogiques (DAC). En fait, il est également un signal multi-ton où les fréquences LIF des signaux sont réparties sur l'axe négatif et positif afin de réduire la fréquence d'échantillonnage du DAC. De plus, la structure donne un contrôle total sur l'amplitude de chaque signal CW ce qui est une caractéristique importante, puisque les signaux reçus dans chaque sous bande peuvent avoir des niveaux de puissance différents. En outre, les considérations pratiques ainsi que les altérations du modulateur sont analysés et étudiés. Enfin, la structure complète a été simulée avec MATLAB® et mise en œuvre en pratique dans un récepteur CA. Il est également démontré que dans la solution proposée le taux d'échantillonnage est beaucoup plus faible que dans les solutions habituelles où le signal multi-tons est généré directement à partir de la bande de base en RF.

Dans le deuxième chapitre de ce rapport, l'émetteur CA est étudié et la technique développée précédemment pour la génération du signal multi-tons est adaptée pour être utilisée pour la génération du signal CA. Le chapitre commence par la description de la modulation et de la démodulation (OFDM). Les aspects pratiques de la mise en œuvre du signal OFDM, tels que la synchronisation de temps et de fréquence du signal, sont expliqués. Ensuite, une méthode hybride de synchronisation de fréquence est proposée. Une solution de diversité de fréquence, où un symbole OFDM identique est transmis sur différentes porteuses de composants est proposée. Différents signaux OFDM sont générés sur différentes bandes de fréquence comme requis dans la norme LTE-A.

La structure est développée et mise en œuvre pour un cas avec à 3 bandes de fréquence. Comme dans le cas de la structure multi-tons, le taux d'échantillonnage du DAC est considérablement réduit. En outre, n émetteurs (1 émetteur par bande de fréquence) sont remplacés par un seul dans la structure proposée. De plus, la dégradation du modulateur I / Q dans le cas de l'émetteur CA est étudiée et une solution de compensation numérique (look-up table) est proposée. Le chapitre se termine par une mise en œuvre expérimentale de la structure CA et la démodulation des 3 bandes de fréquence en utilisant deux récepteurs différents, qui sont un démodulateur triphasé multi bandes et un analyseur de signaux vectoriels mono bande. Enfin, les résultats sont comparés à l'état de l'art actuel pour évaluer les performances de notre solution.

Le dernier chapitre de ce document se focalise sur la compensation des imperfections et notamment de la faible non-linéarité du modulateur I / Q de notre structure. La modélisation comportementale est utilisée pour modéliser la fonctionnalité de notre modulateur multi-bandes I / Q. Le chapitre commence par citer l'état de l'art des modèles comportementaux utilisés dans les cas mono-bande et multi-bandes. Le processus de recherche de l'inverse du modèle comportemental ou de la pré-distorsion numérique (DPD) est expliqué en détail. Un modèle comportemental adapté au cas d'un signal CA à trois bandes est proposé qui inclut les non-linéarités ainsi que les déséquilibres de gain et de phase du modulateur I / Q. Le signal DPD est obtenu en utilisant un algorithme d'apprentissage indirect et un algorithme de moindres carrés. Le modèle et le DPD sont simulés par MATLAB® et mis en œuvre expérimentalement à l'aide d'un générateur de forme d'onde arbitraire. La simulation montre une amélioration significative de la valeur quadratique moyenne des signaux de sortie du modulateur I / Q. Enfin, la mise en œuvre expérimentale montre la compensation de la dégradation apportée par le modulateur I / Q, mais une certaine régénération spectrale, dont on explique l'origine, est observée à la sortie du modulateur I / Q. Enfin, la dissertation se termine par la conclusion de cette recherche et des perspectives pour des travaux futurs sont proposées.

Chapitre 1 : Génération d'un signal multi-tone

Des signaux multi-tones sont utilisés dans plusieurs domaines de transmission radio fréquence. Ils sont utilisés pour caractériser la non-linéarité des mélangeurs et des amplificateurs de puissance (PA). En plus, les signaux multitones peuvent remplacer plusieurs oscillateurs locaux (OL) dans les émetteurs et récepteurs à multi-porteuses/multi-bandes. Par Ex: la technologie de quatrième génération de téléphonie mobile (LTE-A) utilise la technique de l'agrégation en fréquences où on peut remplacer les OLs par un signal multitone en réception et en émission. En outre, afin d'augmenter le taux binaire de transmission, la cinquième génération de téléphonie mobile propose aussi l'utilisation de l'agrégation en fréquence pour sa transmission.

1.1 Etat de l'art :

Il y a plusieurs travaux qui s'intéressent au signaux multi-tones. Lu *et al.* [7] ont proposé une méthode de génération de signal avec 4 tones. Ils utilisent un OL en multiplexage temporelle en parallèle avec des registres et additionneurs numériques. Un Convertisseur Numérique Analogique (CNA) convertis le signal numérique vers analogique. La méthode porte deux contraintes majeures, la première est que la fréquence d'échantillonnage de CNA qui est directement proportionnelle aux nombres des tones et leur espace de séparation. La seconde contrainte vient du fait qu'ils génèrent leur signal directement en bande RF ce qui nécessite un CNA avec une fréquence d'échantillonnage très élevée. Dans un autre travail, Traverso *et al.* [8] ont présenté un synthétiseur créant un signal multi-bande de type « Orthogonal Frequency Division Multiplexing « (OFDM) qui est suggéré dans la norme IEEE 802.15.3a. Ils ont utilisé une boucle à verrouillage de phase, 4 circuits de division par deux, un mélangeur large bande et quatre mélangeurs classiques (bande étroite) pour générer 14 canaux de 528 MHz, comme affiché en Figure 1 :

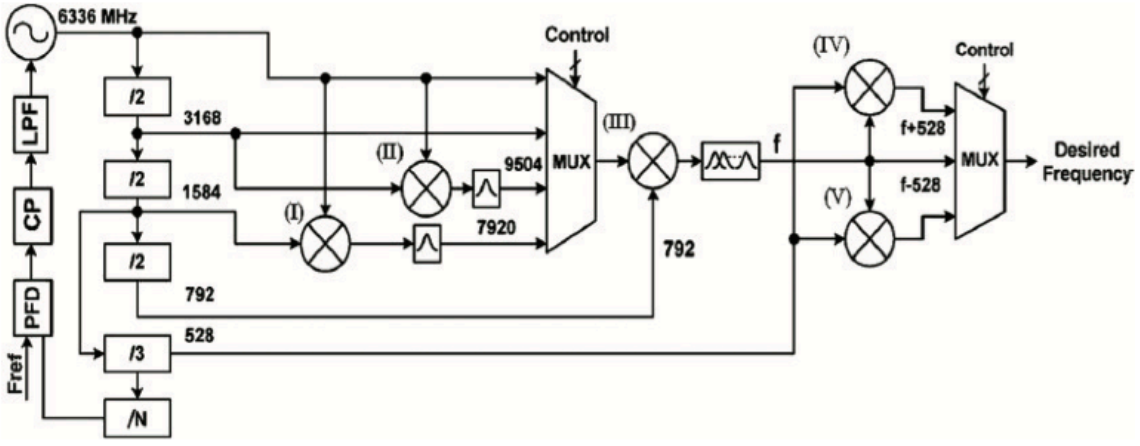

Figure 1 : Synthétiseur d'un signal OFDM multi-bande

La contrainte de ce travail est que les canaux sont situés sur des fréquences centrales sous multiples de 2, ce qui limite l'allocation fréquentielle.

Keysight a implémenté les signaux multi-tones dans ses générateurs des signaux. Plusieurs porteuses sont créées autour de la fréquence centrale. Donc, pour avoir une configuration précise, il faut éteindre les porteuses non désirées, comme illustré dans la Figure 2. La contrainte de cette méthode est liée au fait que les fréquences doivent être séparées d'une valeur minimale Δf, ce qui limite la configuration fréquentielle dans les systèmes de communications.

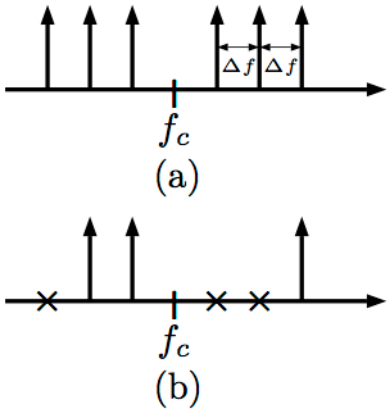

Figure 2 : (a) Génération de beaucoup de tones équidistantes (b) éteindre plusieurs afin d'atteindre la configuration désirable

Les « Direct Digital Synthesizers » (DDS) proposent une nouvelle méthode pour générer des signaux périodiques, y compris des signaux multi-tones. Un DDS est un système basé sur la lecture ou la sélection d'échantillons. Il contient une horloge fréquentielle de référence, un accumulateur de phase, un oscillateur contrôlé par entrée numérique et un CNA. Le signal est transformé sous forme d'états de phase stockés dans un accumulateur de N bits. Puis, avec un tableau de recherche (Look-Up Table (LUT)) chaque mot de code de l'accumulateur est associé à l'échantillon de phase voulu. A la fin, le CNA génère la forme d'onde analogique du signal. Un DDS contrôle assez finement la résolution sur la forme d'onde et l'allocation fréquentiel du signal. La fréquence de sortie de DDS est donnée par la suite [12, 13] :

$$F_o = \frac{F_{clk}}{2^N}\Delta_{ACC} \qquad (1)$$

où F_o, F_{clk} , N et Δ_{ACC} sont la fréquence de sortie, la fréquence d'échantillonnage d'horloge, la longueur de l'accumulateur et la phase d'incrémentation de l'accumulateur, respectivement. Un DDS peut générer toutes les fréquence jusqu'au $\frac{F_{clk}}{2}$. Par contre, il y a des contraintes aussi, les produits harmoniques de CNA sont directement proportionnels $\frac{F_{clk}}{f_o}$ ce qui limite la

dynamique d'un DDS. Ceci est lié au fait que l'erreur de quantification de DAC augmente avec ce rapport. Pour alléger cette contrainte, on peut ajouter un petit offset fréquentiel sur la fréquence de sortie pour qu'elle ne soit pas une valeur entière de la fréquence d'horloge. Toutefois, ceci augmente le bruit de phase du signal [13]. On a caractérisé les performances d'un DPG3 de chez Analog Devices avec sa carte d'évaluation. C'est un générateur numérique sur la base d'un DDS. On n'a pas pu exploiter cette solution, car la longueur des signaux générés est imposée par Analog Devices pour qu'il soit un multiple de 256 échantillons. Ceci est un contraint majeur, par exemple, un signal modulé avec 2048 symboles QPSK, un facteur de sur-échantillonnage de 6 avec un filtre de racine de Nyquist (roll-off = 0,35) crée une forme d'onde de longueur de 12 480 échantillons. Donc, on a choisi le générateur arbitraire du signal ce qui nous offre plus de degré de liberté.

1.1.1Agrégation de porteuses :

Afin d'augmenter le débit binaire, la norme LTE-A propose la transmission avec une bande passante qui peut atteindre à 100 MHz. Cette bande passante est très large pour le domaine RF dont les ressources spectrales disponibles sont limitées. La norme propose d'utiliser jusqu'à 5 sous bandes dont la largeur carie entre 1,4 à 20MHz. Les sous bandes sont réparties dans le spectre sous trois formes ; (a) intra-bande contigu, (b) intra-bande non contigu et (d) inter-bande non-contigu . Les trois configurations sont affichées en Figure 2.

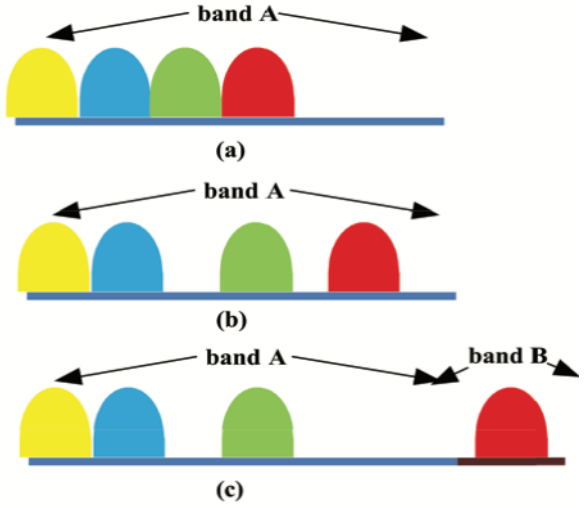

Figure 3 : (a) intra-bande contigu, (b) intra-bande non contigu, (d) inter-bande non-contigu

En réception, on transpose nos signaux agrégés en fréquence en bande de base ou en bande intermédiaire. Ceci peut être fait de plusieurs façons dont l'utilisation d'un démodulateur tri-phasé (TPD) à mélangeurs. Dans [17], les auteurs ont utilisé un TPD ultra-large bande afin de démoduler un signal avec trois bandes agrégées en fréquence toute en utilisant qu'un seul

convertisseur analogique numérique (CAN). Toutefois, ils ont utilisé 3 OLs pour transposer les 3 bandes en bande intermédiaire. Afin d'éviter l'utilisation de plusieurs OLs, on propose l'utilisation d'un signal multi-tone (3-tones).

1.2 L'oscillateur local multi-tone pour l'agrégation en fréquence

Il y a plusieurs manières de démodulation d'un signal agrégé en fréquence. La première est d'utiliser un récepteur pour transposer chacune des bandes de manière séquentielle, comme affichée en Figure 4 (a). La deuxième s'agit d'utiliser *K* récepteurs pour *K* bandes, Figure 4(b) ; Figure 4 (c) montre la troisième manière où toutes les bandes sont transposées à la bande intermédiaire. La dernière s'agit transposer *K* bandes en bande intermédiaire, de manière simultanée, avec *K* OLs, Figure 4 (d). la stratégie (d) ne convient le plus est on a choisi pour notre démodulateur.

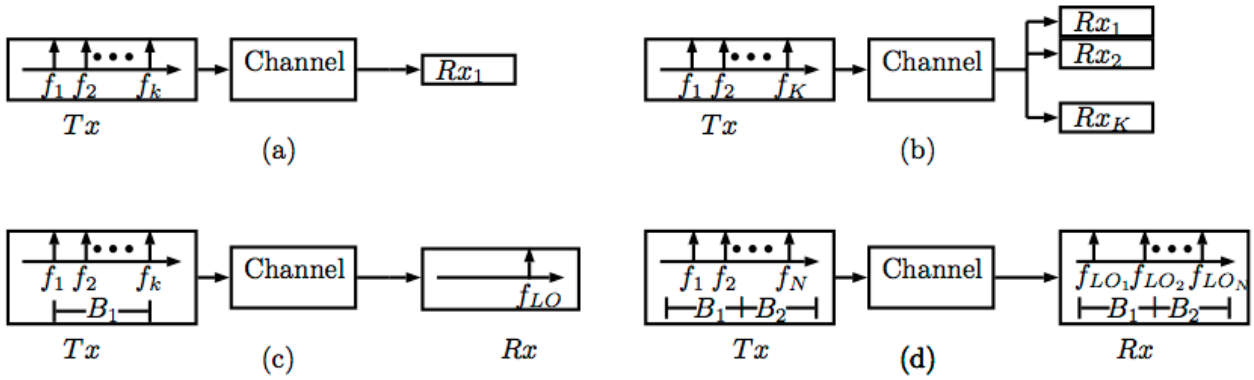

1.2.1 Méthode de génération des signaux M-tone

On peut créer le signal multi-tone en bande intermédiaire et le transposer en bande RF avec un modulateur RF. Un signal avec N tones est écrit :

$$x(t) = Re\{\sum_{k=1}^{N} \alpha_k e^{i(2\pi f_k t + \theta_k)}\}$$

$$x(t) = Re\{(\sum_{k=1}^{N} \alpha_k e^{i(2\pi h_k t + \theta_k)}) e^{i2\pi f_c t}\} \qquad (2)$$

Où $x(t)$, $Re\{\}$, a_k, θ_k, f_k, h_k, f_c, N et t sont le signal RF multi-tones, la partie en réel, l'amplitude de tone *k*, la phase tone k, sa fréquence en bande RF, sa fréquence en bande intermédiaire, la fréquence de porteuse centrale, le nombre des tones et la variable de temps, respectivement. L'Eq (2) peut-être réécrite :

$$x\,(t) = Re\{(I\,(t) + jQ\,(t))\, e^{i2\pi f_c t}\} \qquad (3)$$

Avec :

$$I(t) = \sum_{k=1}^{N} \alpha_k cos\{2\pi h_k t + \theta\}$$

$$Q(t) = \sum_{k=1}^{N} \alpha_k sin\{2\pi h_k t + \theta\}$$

Où $I(t)$ et $Q(t)$ sont les parties en phase et en quadrature, respectivement.

D'après (2), les fréquences RF s'écrivent :

$$f_k = h_k + f_c \qquad for \qquad k = 1, 2, ..., N \tag{4}$$

Et la fréquence d'échantillonnage de CNA est donnée par :

$$f_{DAC} > OSR * max\{|\ h_k\ |\} \tag{5}$$

Ceci nous permet de réduire la fréquence d'échantillonnage, car les fréquences intermédiaires h_k sont situées aux fréquence négatives et positives. Afin de montrer le fonctionnement de notre méthode, on simule, sur Matlab, notre génération de signaux pour des fréquences à 2,2 GHz, 2,3 GHz et 2,7 GHz. Les signaux intermédiaires et leurs images sont affichés au Tableau 1.

	h_1	h_{im1}	h_2	h_{im2}	h_3	h_{im3}
LIF (MHz)	-350	350	-50	50	350	-350

Tableau 1 les tones intermédiaires et leurs images

La Figure 4 montre les parties en phase (a), en quadrature (b) et l'amplitude de l'enveloppe complexe (c) du signal multi tones avec les fréquences intermédiaires.

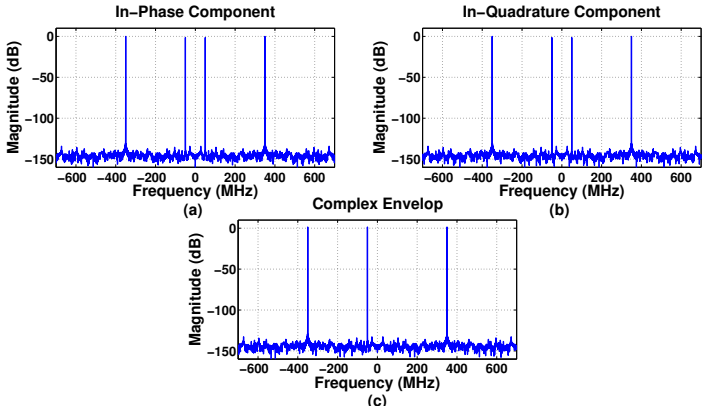

Figure 4 l'amplitude des parties (a) en phase (b) en quadrature (c) l'enveloppe complexe

Dans la partie suivante, on se concentre sur la réalisation pratique de la génération de ce signal.

1.3 Résultats expérimentaux

On a implémenté notre méthode en utilisant le générateur des signaux N5172B qui a un CNA avec une fréquence d'échantillonnage de 150 Mech/s. On a généré un signal RF avec 3 tones qui sont affichés au Tableau 2. On a créé sous Matlab l'enveloppe complexe qui contient les tones aux fréquences intermédiaires. Cet enveloppe complexe est transposée en bande RF en utilisant le modulateur interne du générateur. On a aussi ajouté un offset fréquentiel (γ) à la fréquence de porteuse afin d'éviter le chevauchement spectral entre les tones en bande intermédiaire et leurs images. La fréquence d'échantillonnage est de 135 Mechan/s pour valider (5).

f_1	f_2	f_3	h_1	h_2	h_3	f_c	γ	*Freq. D'échantillonage*
2,00 GHZ	2,03 GHz	2,07 GHz	25 MHz	5 MHz	45 MHz	2,025 GHz	10 MHz	135 M.echan/s

Tableau 2 Les tones RF et leurs tones en bande intermédiaire

La Figure 5 montre le spectre à la sortie du générateur. On a réduit le niveau de puissance de la première fréquence de 20 dB pour montrer la possibilité de contrôler le niveau de puissance de chacune des tones.

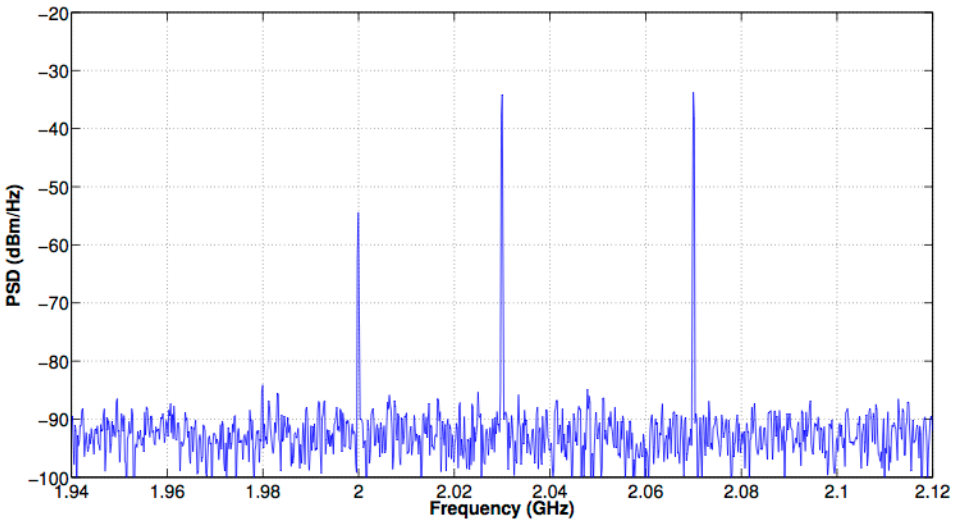

Figure 5 la densité spectral du signal à la sortie de modulateur.

On a appliqué dans un démodulateur TPD fabriqué au sein de notre laboratoire, afin de transposer les signaux RF agrégés en fréquences aux fréquences intermédiaires. La Figure 6 affiche la sortie de notre démodulateur qui montre que la transposition en bande intermédiaire

est bien effectuée. Les bandes agrégées en fréquence sont situées aux 1.9978 GHz, 2.0273 GHz et 2.0668 GHz. Les tones sont situés aux 2.00 GHz, 2.03 GHz et 2.07 GHz.

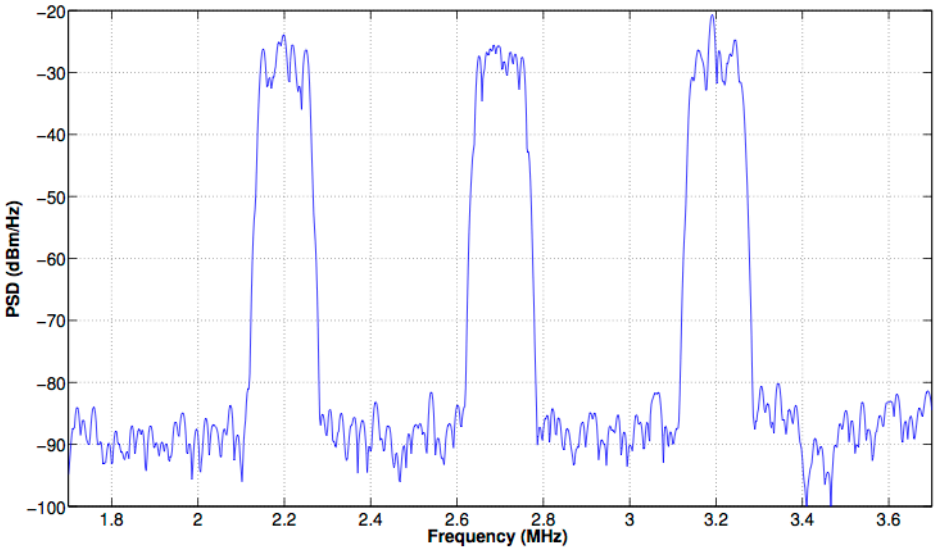

Figure 6 la densité spectrale à la sortie du TPD

1.4 Conclusion

Dans ce chapitre, on a vu comment générer un signal multitone en utilisant un seul générateur de signal avec 2 CNAs, un modulateur I/Q et un OL. On réduit fortement la fréquence d'échantillonnage du CNA par rapport à la génération directe, grâce à la distribution des tones en fréquence intermédiaire dans la partie positive et négative du spectre. On a aussi montré une application où on a appliqué notre signal multitone dans un démodulateur TPD afin de transposer les signaux agrégés en fréquences en bande intermédiaire.

Chapitre 2 : Agrégation en fréquence dans le contexte de LTE-A

LTE-A est la seconde phase dans l'évolution du LTE. Il augmente le débit binaire aux 1 Gbps en lien descendant est 200 Mbps en lien montant. Il utilise MIMO (Multiple Input Multiple Output) et l'agrégation en fréquence afin d'atteindre les débits proposés. Dans ce travail de recherche on s'est concentré sur l'agrégation en fréquence. Afin de réduire l'interférence entre symbole (ISI), LTE-A propose une modulation de type OFDM pour l'émission des symboles. OFDM rendre un canal, sélectif en fréquence, non sélectif. Dans ce type de modulation, plusieurs sous porteuses orthogonales transmettent les symboles avec diffèrentes modulations (BPSK, FSK, QPSK,…) en parallèle dans des bandes passantes réduites.

2.1 Modulation OFDM

L'idée est d'utiliser plusieurs porteuses avec une bande passante réduite (les symboles plus longs). Imaginez le symbole $X_q(k)$ soit le symbole numéro q parmi un nombre infini des symboles émis sur la sous porteuse numéro k (k = 1,…, N) . Ces symboles sont mis en parallèle pour qu'ils soient émis sur les N sous porteuses. Un signal OFDM en bande de base est écrit comme :

$$x_q(t) = \sum_{q=0}^{\infty} \sum_{k=0}^{N-1} X_q(k) e^{j2\pi f_k (t-qT)} \tag{2.1}$$

où $X_q(t)$ et T sont le symbole OFDM en domaine temporel et la durée de symbole, respectivement.

En domaine discret, (2.1) est écrit :

$$x_q(n) = \sum_{k=0}^{N-1} X_q(k) e^{j2\pi k \frac{n}{N}} \quad for\ n = 0, ..., N-1 \tag{2.2}$$

qui est la transformation inverse de Fourier pour N points.

2.2 Démodulation OFDM

Imaginons qu'on reçoit le symbole de (2.2) en récepteur, donc le signal est écrit :

$$y_q(n) = \sum_{k=0}^{N-1} X_q(k) e^{j2\pi k \frac{n}{N}} \quad for\ n = 0, ..., N-1 \tag{2.3}$$

Sa transformation de Fourier devient :

$$
\begin{aligned}
Y_q(k) &= \sum_{n=0}^{N-1} y_q(n) e^{-j2\pi k \frac{n}{N}} \\
&= \sum_{n=0}^{N-1} \left\{ \frac{1}{N} \sum_{l=0}^{N-1} X_q[l] e^{j2\pi l \frac{n}{N}} \right\} e^{-j2\pi k \frac{n}{N}} \\
&= \sum_{n=0}^{N-1} \sum_{l=0}^{N-1} \frac{1}{N} X_q[l] e^{j2\pi (l-k) \frac{n}{N}} = X_q[k]
\end{aligned}
\tag{2.4}
$$

la dernière partie de (2.4) est vraie si les sous porteuses sont orthogonales. En utilisant l'OFDM, on a réduit l' ISI lié aux canal sélectif en fréquence, mais l'ISI lié aux effet multi-trajets existe toujours. Pour ceci on a ajouté un préfix cyclique (CP). Le CP est une séquence de symboles de longueur L (L supérieure à la longueur de filtre du canal) que l'on place en fin de trame des symboles et répétée en début de trame suivante pour réduire l'ISI des symboles de la trame OFDM précédente, Figure 7.

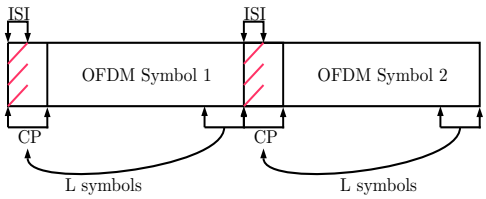

Figure 7 Les symboles OFDM avec CP : robuste contre ISI

2.3 Génération d'un signal OFDM

Afin d'éviter une mauvaise réception des symboles, il faut s'assurer des synchronisations temporelles et fréquentielles. Si la synchronisation temporelle n'est pas respectée, la constellation des symboles reçus n'est pas net (erreur de phase). Les symboles sont éloignés de leur lieu, Figure 8.a. Si la synchronisation fréquentielle n'est pas respectée, les symboles subissent une rotation de phase dépendante de l'écart fréquentiel généré Figure 8.b. .

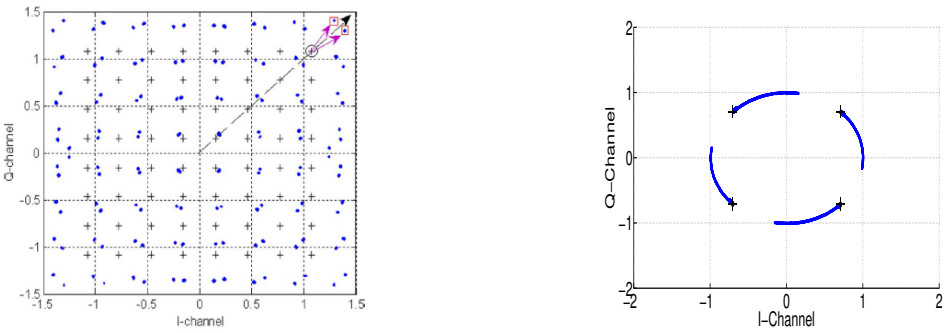

(a) (b)

Figure 8 Les effets de désynchronisation : (a) temporelle, (b) fréquentielle

La synchronisation temporelle est réalisée en utilisant une corrélation glissante entre la séquence d'apprentissage et la trame des échantillonnes reçus [68]. Afin d'établir la synchronisation fréquentielle on transmet successivement deux séquences d'apprentissage identiques de type CAZAC et on calcule la différence de phase entre deux symboles correspondant de chaque séquence, comme affiché en Figure 9.

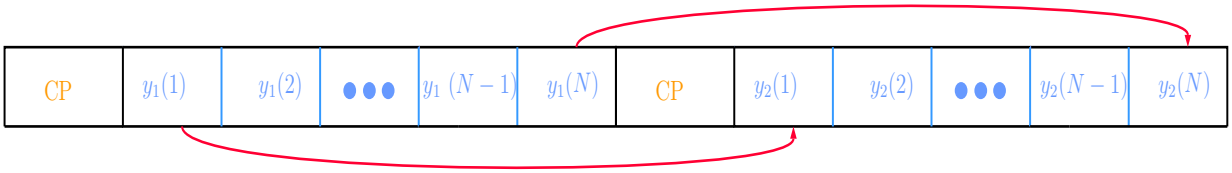

Figure 9 Synchronisation fréquentielle

On cherche à trouver l'offset fréquentielle entre les deux séquences d'apprentissage, par :

$$y_2(k) = y_1(k)e^{j2\pi f_{CFO}\Delta T} \quad for\ k = 1, \ldots, N \tag{2.5}$$

où $y_1(k)$, $y_2(k)$, F_{CFO} et Δt sont la première et la deuxième séquence d'apprentissage , l'offset fréquentielle et la différence de temps entre les symboles de deux sous porteuses. On peut trouver l'offset fréquentiel par la formule suivante :

$$f_{CFO} = \frac{1}{2\pi\Delta T} arg\left(\sum_{k=1}^{N} y_2(k)y_1^*(k)\right) \tag{2.6}$$

où ()* montre la conjugué du signal.

On appliquant notre méthode de synchronisation on a pu compenser un offset fréquentiel de 69Hz, comme affiché en Figure 10.

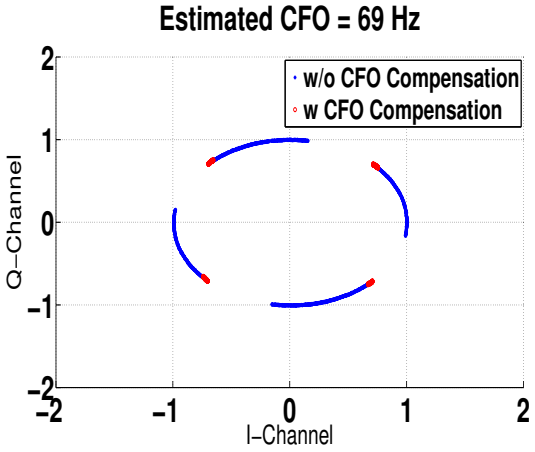

Figure 10 La synchronisation fréquentielle : (a) sans synchronisation. (b) avec synchronisation

2.4 Agrégation en fréquence avec trois signaux OFDM

Dans cette partie, on montre comment transmettre trois signaux OFDM sur trois porteuses agrégées. En plus, on montre qu'on a le contrôle sur le niveau de puissance de chacune des porteuses.

Imaginons que les trois porteuses sont situées f_1, f_2 et f_3 ($f_1 < f_2 < f_3$), les porteuses agrégées en fréquence sont données par :

$$x(t) = Re\left\{\alpha e^{i2\pi f_1 t} + \beta e^{i2\pi f_2 t} + \gamma e^{i2\pi f_3 t}\right\} \tag{2.7}$$

Ceci est réécrit de cette manière :

$$x(t) = Re\left\{\left(\alpha e^{i2\pi h_1 t} + \beta e^{i2\pi h_2 t} + \gamma e^{i2\pi h_3 t}\right) e^{i2\pi f_c t}\right\} \tag{2.8}$$

Où :

$$\begin{aligned} h_1 &= f_1 - f_c & h_2 &= f_2 - f_c \\ h_3 &= f_3 - f_c & f_c &= \frac{f_1 + f_3}{2} \end{aligned} \tag{2.9}$$

avec α, β, γ sont les amplitudes de chaque porteuse.

Le signal OFDM en bande de base pour chaque porteuse est donnée par :

$$x_{OFDM_k}(t) = I_k(t) + jQ_k(t)t \quad k \in \{1,2,3\} \tag{2.10}$$

En combinant (2.8) avec (2.10), on obtient les porteuses modulées.

$$\begin{aligned} x(t) = Re\{&(\alpha\,(I_1(t) + jQ_1(t))\,e^{i2\pi h_1 t} + \beta\,(I_2(t) + jQ_2(t))\,e^{i2\pi h_2 t} \\ &+ \gamma\,(I_3(t) + jQ_3(t))\,e^{i2\pi h_3 t})e^{i2\pi f_c t}\} \\ = Re&\left\{(I(t) + jQ(t))\,e^{i2\pi f_c t}\right\} \end{aligned} \tag{2.11}$$

Avec les parties en phase et en quadrature :

$$\begin{aligned} I(t) = &\alpha\,(I_1\cos(2\pi h_1 t) - Q_1\sin(2\pi h_1 t)) \\ &+ \beta\,(I_2\cos(2\pi h_2 t) - Q_2\sin(2\pi h_2 t)) \\ &+ \gamma\,(I_3\cos(2\pi h_3 t) - Q_3\sin(2\pi h_3 t)) \end{aligned} \tag{2.12}$$

$$\begin{aligned} Q(t) = &\alpha\,(I_1\sin(2\pi h_1 t) + Q_1\cos(2\pi h_1 t)) \\ &+ \beta\,(I_2\sin(2\pi h_2 t) + Q_2\cos(2\pi h_2 t)) \\ &+ \gamma\,(I_3\sin(2\pi h_3 t) + Q_3\cos(2\pi h_3 t)) \end{aligned}$$

En utilisant notre méthode on a réduit la fréquence d'échantillonnage de CNA par rapport à la génération directe : (2.13)

$$f_{s_{carrier}} > 2|h_3|$$

Cette réduction de fréquence d'échantillonnage est liée au fait que les porteuses en bande intermédiaires sont placées dans la partie positive et négative de spectre.

Afin de bien implémenter la méthode il faut que les symboles aient la même fréquence d'échantillonnage que les porteuses, donc il faut les sur-échantillonner avec le facteur suivant :

$$OSR_k = \frac{f_{s_{carrier}}}{R_{OFDM_k}} \quad k \in \{1, 2, 3\} \tag{2.14}$$

Où R_{OFDM_k}et OSR_k sont le taux de symboles et le facteur de sur-échantillonnage de porteuse numéro *k*, respectivement.

2.5 Les déséquilibres I/Q

Un modulateur I/Q n'est jamais parfait, un déséquilibre en phase est souvent présent. Dans ce cas on peut modéliser notre modulateur de la façon suivante :

$$\begin{aligned}
x(t) &= Re\left\{(I(t) + jQ(t))\, e^{i2\pi f_c t}\right\} \\
I(t) &= \alpha\,(I_1\cos(2\pi h_1 t + \phi_1) - Q_1\sin(2\pi h_1 t + \phi_1)) \\
&\quad + \beta\,(I_2\cos(2\pi h_2 t + \phi_2) - Q_2\sin(2\pi h_2 t + \phi_2)) \\
&\quad + \gamma\,(I_3\cos(2\pi h_3 t + \phi_3) - Q_3\sin(2\pi h_3 t + \phi_3)) \\
Q(t) &= \alpha\,(I_1\sin(2\pi h_1 t) + Q_1\cos(2\pi h_1 t)) \\
&\quad + \beta\,(I_2\sin(2\pi h_2 t) + Q_2\cos(2\pi h_2 t)) \\
&\quad + \gamma\,(I_3\sin(2\pi h_3 t) + Q_3\cos(2\pi h_3 t))
\end{aligned} \tag{2.15}$$

où ϕ_1, ϕ_2, ϕ_3 sont les déséquilibres de phase pour les porteuse numéro 1, 2 et 3, respectivement.

Les déséquilibres I/Q nous évitent la disparition des signaux d'images, comme on a expliqué dans le premier chapitre. On ajoute un offset fréquentiel (η) afin d'éviter le chevauchement entre les porteuses et leurs images. (2.16) montre l'offset fréquentielle ajouter à la fréquence d'OL.

$$f_c = -\eta + \frac{f_1 + f_3}{2} \tag{2.16}$$

Le problème de chevauchement est montré dans la Figure 11. Afin de l'éviter les conditions suivantes doivent être établies :

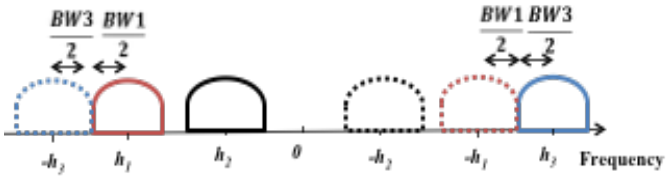

Figure 11 les porteuses modulées avec leur image

$$h_3 - \frac{BW3}{2} \geq -h_1 + \frac{BW1}{2} \Rightarrow \eta \geq \frac{BW1 + BW2}{4} \tag{2.17}$$

$$|h_2| + \frac{BW2}{2} \geqslant \eta \tag{2.18}$$

Où $BW1$, $BW2$ et $BW3$ sont les bandes passantes des porteuses 1, 2 et 3, respectivement. Pour le cas général avec n. Il faut que la condition suivante soit valide.

$$f_c = -\eta + \frac{f_1 + f_n}{2} \quad with \quad \eta \geqslant \frac{BW1 + BWn}{4} \tag{2.19}$$

Si n soit impaire :

$$|h_g| + \frac{BWg}{2} \geqslant \eta \ , \ g = \frac{n+1}{2} \tag{2.20}$$

La Figure 12 montre l'effet des déséquilibres I/Q sur le spectre à la sortie du modulateur. Le modulateur

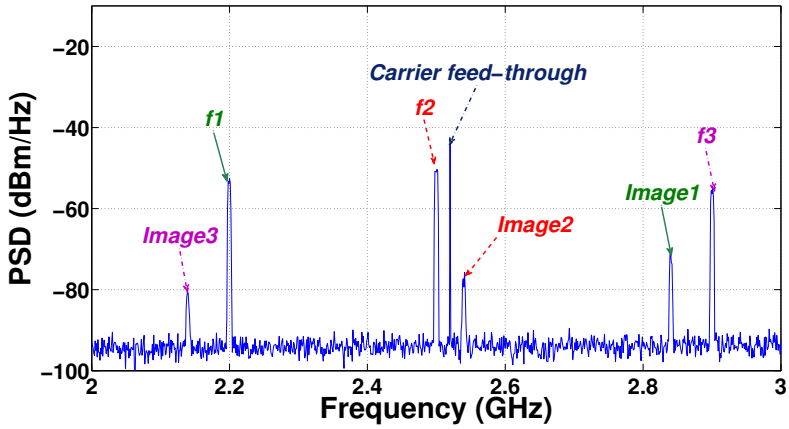

Figure 12 L'effet des déséquilibres I/Q

2.5.1 La compensation des déséquilibres I/Q

On a étudié chacune des porteuses séparément afin de trouver, manuellement, la phase qui minimise le signal "image". On sauvegarde les valeurs de phase de chacune des porteuses dans un tableau et on les utilisera pour différentes configurations fréquentielles.

Dans la partie suivante on verra l'efficacité de notre méthode.

2.6 Génération du signal

On a généré un signal agrégé en fréquences avec les spécifications données dans le Tableau 3.

RF Frequency	$f_1 = 2.2$ GHz	$f_2 = 2.5$ GHz	$f_3 = 2.9$ GHz	$f_c = 2.52$ GHz
LI Frequency	$h_1 = -320$ MHz	$h_2 = -20$ MHz	$h_3 = 380$ MHz	$\eta = 30$ MHz
Power	-42 dBm	-42 dBm	-42 dBm	10 dBm
Bandwidth	5 MHz	5 MHz	5 MHz	–
Sampling rate	1.14 GHz	1.14 GHz	1.14 GHz	–
Modulation	QPSK-OFDM			CW
N	32			–
L	8			–
DC-Null Subcarrier	✓			–
TS	CAZAC			–

Tableau 3 Les spécifications du signal agrégé en fréquence

On a généré avec Matlab les parties en phase et en quadrature du signal. Ainsi, on les a transmis aux générateurs du signal (Tektronix AWG7122b) qui contient 2 CNA. A la sortie du générateur on a mis les filtres anti-repliement fabriqué au laboratoire. Puis, les signaux filtrés entre dans le modulateur I/Q. On a aussi utilisé les Tés de polarisation afin de réduire la fuite d'OL dans le modulateur, en ajoutant quelques mV de tension sur la voie I. le modulateur et le banc de test sont affichés en Figure 13.

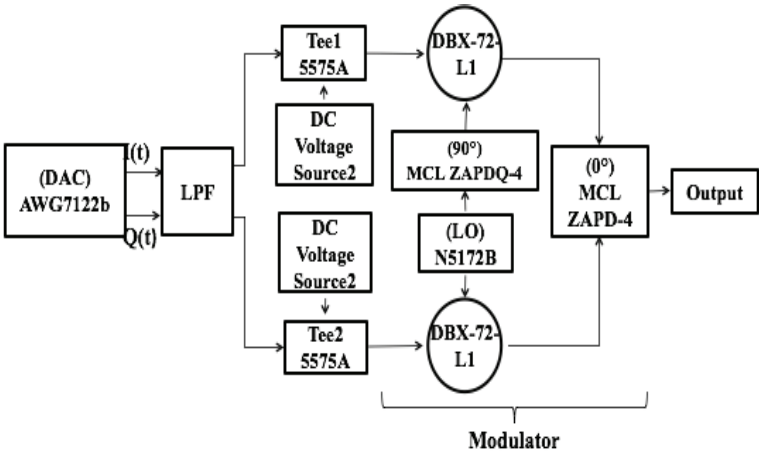

(a)

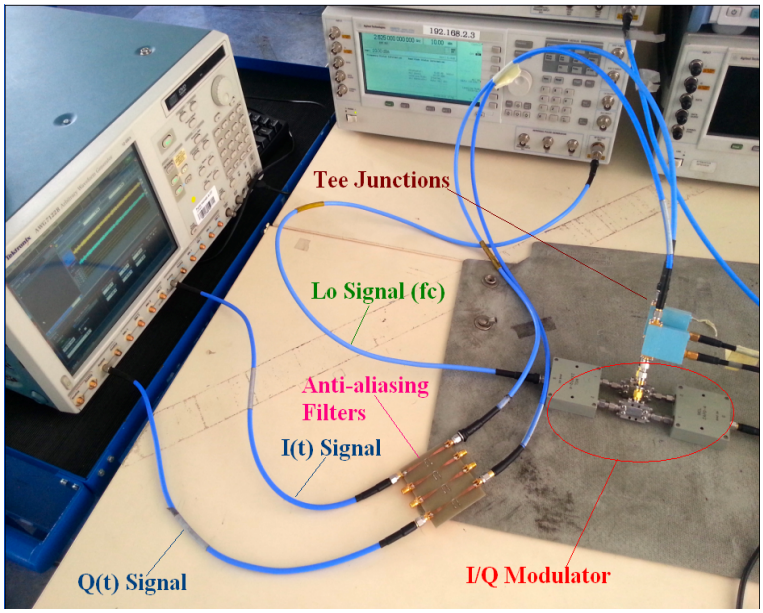

(b)

Figure 13 (a) Le schéma synoptique de modulateur (b) La photo de banc de test

Pour cette configuration fréquentielle, on a compensé les déséquilibres de phase en ajoutant les phases données dans le Tableau 4 aux porteuses.

Component Carriers	Images	Phase Compensation
$f_1 = 2.2$ GHz	$Imag1 = 2.84$ GHz	$\phi_1 = 9.5\ ^\circ$
$f_2 = 2.5$ GHz	$Imag2 = 2.54$ GHz	$\phi_2 = 5\ ^\circ$
$f_3 = 2.9$ GHz	$Imag3 = 2.14$ GHz	$\phi_3 = -4\ ^\circ$

Tableau 4 Compensation de phase

La Figure 14(a) montre le spectre du signal après avoir effectué la compensation. La figure 14(b) montre le contrôle sur le niveau de puissance émise à la sortie de modulateur.

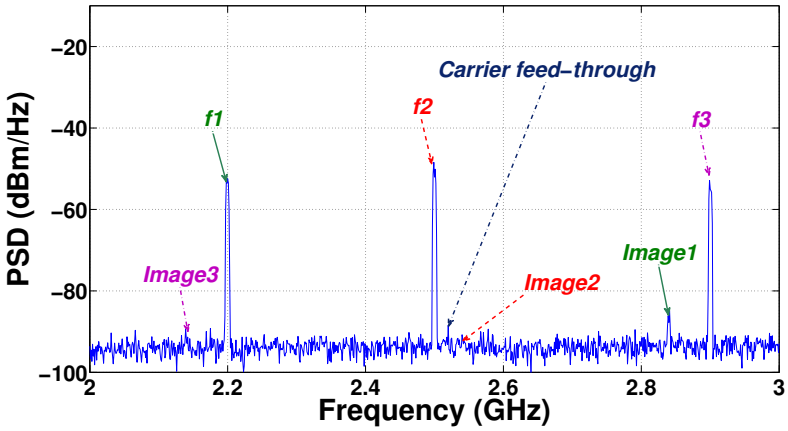

(a)

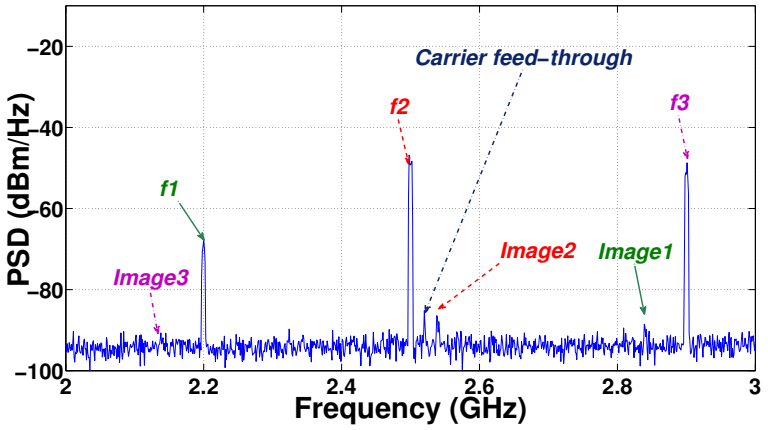

(b)

Figure 14 Le spectre à la sortie du modulateur : (a) après calibrage (b) contrôler la puissance émise sur chacune des porteuses

On voit dans la Figure 14 (a) que l'Image1 n'est pas éliminée, ceci est lié au fait que les porteuses sont corrélées à travers le fonctionnement non linéaire du modulateur. Afin de réduire les images, on propose dans le chapitre suivant un modèle et une pré-distorsion numérique (DPD).

2.7 Démodulation du signal

Afin de démoduler le signal, on a utilisé deux démodulateurs : le démodulateur TPD et l'analyseur du signal vectoriel (VSA) de Rhode & Schwartz. Le TPD est capable de démoduler tous les signaux agrégés en fréquences de manière simultanée, mais le VSA démodule de manière séquentielle. Les Figure 15 montre le schéma de notre système avec un démodulateur VSA.

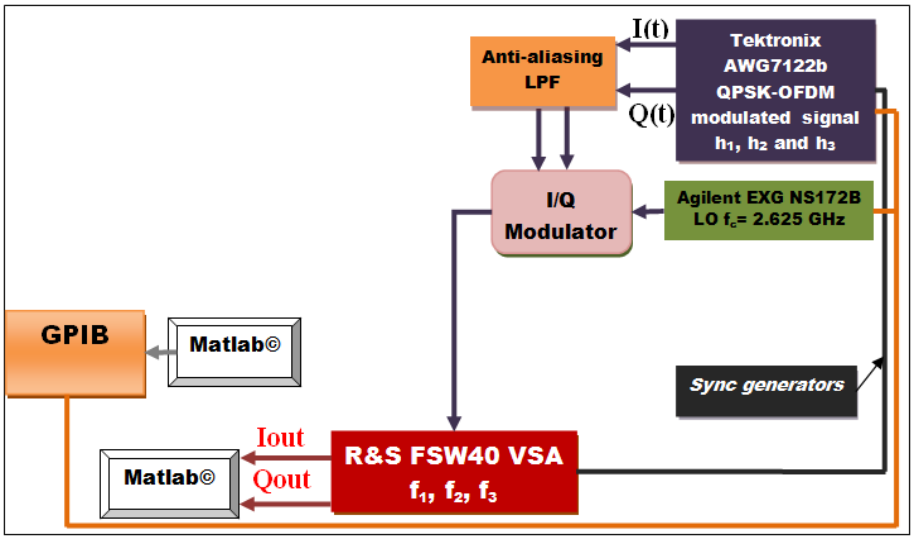

Figure 15 Le banc de test avec le VSA

La Figure 16 montre la constellation de phase des symboles démodulés avec le VSA pour différents ordres de modulation. On observe une très bonne constellation.

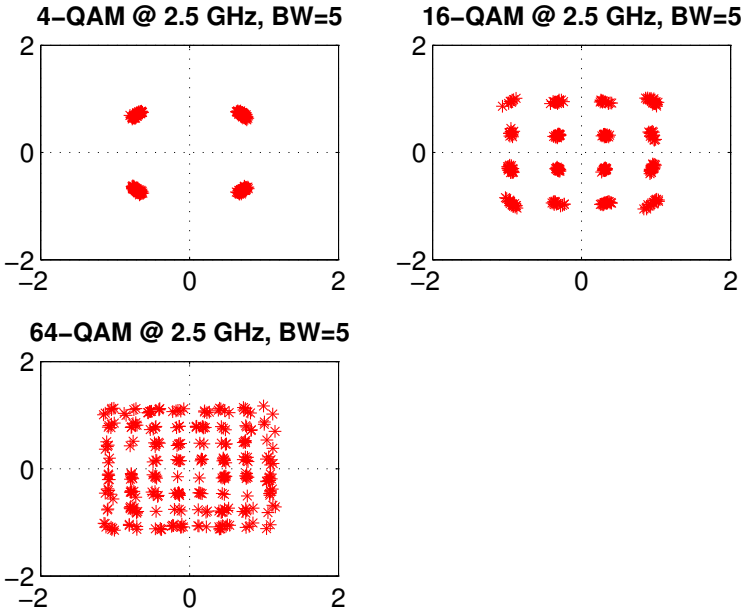

Figure 16 La constellation des symboles démodulés

On a comparé notre méthode avec d'autres méthodes proposées dans la littérature dans le Tableau 5

Techniques	$[f_{min}\ f_{max}]$	Spurs and/or intermodulation component (dBc)	Sampling frequency GS/s
	Bandwidth Component carriers	Component carrier dynamic range	ACLR (dB) EVM [dB]
$\Delta\ \Sigma$ [61]	[0.8 1.5] GHz 5 MHz 2	-10 N.A.	3.9 50 N.A.
$\Delta\ \Sigma$ +Out Phased Multi-level RF Pruning [62]	[0.87 1.5] GHz 10 & 20 MHz 2	-10 N.A.	25 40 N.A.
IFFT Pruning URSP2 [64]	2.4 GHz + [-80 80] KHz 20&60 MHz 2	-20 N.A.	0.1 N.A. -44
DUC [65]	[6.15 6.6] GHz 14 & 122 MHz 4	45 N.A.	2.4 N.A. N.A.
CA OFDM Signals (This Work)	[2.2 2.9] GHz 5 & 10 MHz 3	35 42	1.14 43 -28

Tableau 5 La comparaison des méthodes

La première colonne du Tableau 5 montres les différentes techniques. : ΔΣ [60], ΔΣ + Out phase Multi-level RF Prunning [61], IFFT Prunning URSP2 [63], DUC [64] et notre méthode. La seconde colonne donne les valeurs maximales et minimales de fréquence et la bande passante de chaque signal modulé. Ils sont dans l'intervalle de [0.8 2.4] GHz et 10 MHz, respectivement, sauf [64] où les valeurs sont [6.15 6.6] GHz et 122 MHz. La troisième colonne donne en dBc la rejection des signaux parasites et la dynamique des porteuses agrégées en fréquence. La technique avec DUC et notre méthode montrent une rejection améliorée de 35 dB en comparant avec 10 et 20 dB montré en [60], [61], [63]. Par contre, dans notre travail on a un contrôle de 42 dB sur l'amplitude. La dernière colonne donne les valeurs de fréquence d'échantillonnage, l'ACLR et l'EVM. Notre méthode utilise la plus petite fréquence d'échantillonnage.

2.8 La conclusion

On a proposé une méthode pour l'agrégation de plusieurs porteuses modulées en OFDM. On a montré, aussi, une réduction sur la fréquence d'échantillonnage de CNA. En plus, on a étudié les effets de déséquilibre I/Q dans le modulateur et comment les compenser. On a montré la

procédure de démodulation et en dernière partie on a comparé notre méthode avec les autres dans la littérature.

Chapitre 3 : Le modèle comportementale pour corriger les défauts du modulateur multi-bande.

Les transmissions aux débits élevés ont besoin des signaux très larges bandes. Les signaux ne sont pas parfaits dus aux erreurs quantiques de CNA, de l'imperfection du modulateur I/Q et de la non linéarité de l'amplificateur de puissance. Dans ce chapitre, on se concentre sur les déséquilibres du modulateur I/Q multi-bandes et son fonctionnement non linéaire. Ce fonctionnement non linéaire est lié aux mélangeurs internes du modulateur I/Q. On propose un modèle comportemental et le DPD (pré distorsion) afin de corriger le modulateur I/Q multi-bandes.

3.1 Modèle comportemental mono-bande

Les modèles comportementaux ont deux critères principaux, l'effet mémoire et l'ordre de non linéarité. On a deux types d'effet mémoire ; l'effet mémoire thermique et l'effet mémoire

électrique [77]- [78]. Pour les signaux larges bandes (bande-passante supérieur à 1 MHz) l'effet électrique est dominant.

Le modèle le plus complet et le plus complexe pour un système mono bande est donné par la série de Volterra suivante :

$$y(n) = \sum_{k=1}^{N} \sum_{m_1=0}^{M} \dots \sum_{m_p=0}^{M} h_p(m_1, \dots, m_p) \prod_{j=1}^{k} x(n - m_j) \tag{3.1}$$

où $x(n)$, $y(n)$, $h_p(m_1, \dots, m_p)$, M, N sont respectivement le signal en entrée, le signal en sortie, la fonction des paramètres de Volterra (le kernel de Volterra), la longueur de mémoire et l'ordre de non linéarité. Ce modèle est compliqué, d'autres modèles sont proposés pour simplifier le modèle de Volterra [80]-[81]-[82]-[83]-[84].

3.2 Modèle comportemental multi-bandes

Dans les transmissions multi-bandes les effets non linéaires et l'effet mémoire sont plus importants, donc, il faut prend en compte les différentes porteuses, leurs produits d'intermodulation et leurs harmoniques. Dans [93], un modèle de linéarisation d'un amplificateur de puissance, en considérant les déséquilibres I/Q du modulateur a été proposé. Le modèle donné est (3.2).

$$\begin{aligned} y_1(n) = \sum_{m=0}^{M} \Bigg(& \sum_{k=0}^{N_1} \sum_{j=0}^{k} \alpha_{q,k,l}^{(1)} x_1(n-m) |x_1(n-m)^{k-j}| |x_2(n-m)|^j \\ & + \sum_{k=0}^{N_2} \sum_{j=0}^{k} \beta_{q,k,l}^{(1)} x_1^*(n-m) |x_1(n-m)^{k-j}| |x_2(n-m)|^j \Bigg) + d_1 \end{aligned}$$

$$\begin{aligned} y_2(n) = \sum_{m=0}^{M} \Bigg(& \sum_{k=0}^{N_1} \sum_{j=0}^{k} \alpha_{q,k,l}^{(2)} x_2(n-m) |x_2(n-m)^{k-j}| |x_1(n-m)|^j \\ & + \sum_{k=0}^{N_2} \sum_{j=0}^{k} \beta_{q,k,l}^{(2)} x_2^*(n-m) |x_2 n-m)^{k-j}| |x_1(n-m)|^j \Bigg) + d_2 \end{aligned} \tag{3.2}$$

où $\alpha_{q,k,l}^{(1)}$, $\alpha_{q,k,l}^{(2)}$ sont les coefficients du modèle pour les porteuses 1 et 2, respectivement. En plus, $\beta_{q,k,l}^{(1)}$, $\beta_{q,k,l}^{(2)}$ sont les coefficients du modèle pour les images 1 et 2, respectivement. N_1, N_2 et M sont l'ordre de non linéarité des porteuses, les signaux images et la longueur de mémoire, respectivement.

Dans [70], ils ont étudié un amplificateur de puissance trois bandes, sans prendre en compte les imperfections du modulateur I/Q. On a adapté ce modèle pour un modulateur I/Q multi-bandes avec ses imperfections. Le modèle qu'on a obtenu est le suivant :

$$\begin{aligned}
\widetilde{y_1}(n) &= \sum_{m=0}^{M}\sum_{i=0}^{N_1}\sum_{s=0}^{i}\sum_{l=0}^{s}\Big(h_{misl}^{(1)}\widetilde{x_1}(n)|\widetilde{x_1}(n)|^{i-s}|\widetilde{x_2}(n)|^{s-l}|\widetilde{x_3}(n)|^{l} \\
&\qquad + q_{misl}^{(1)}\widetilde{x_1}^{*}(n)|\widetilde{x_1}(n)|^{i-s}|\widetilde{x_2}(n)|^{s-l}|\widetilde{x_3}(n)|^{l}\Big) + C_1 \\
\widetilde{y_2}(n) &= \sum_{m=0}^{M}\sum_{i=0}^{N_1}\sum_{s=0}^{i}\sum_{l=0}^{s}\Big(h_{misl}^{(2)}\widetilde{x_2}(n)|\widetilde{x_2}(n)|^{i-s}|\widetilde{x_1}(n)|^{s-l}|\widetilde{x_3}(n)|^{l} \\
&\qquad + q_{misl}^{(2)}\widetilde{x_2}^{*}(n)|\widetilde{x_2}(n)|^{i-s}|\widetilde{x_1}(n)|^{s-l}|\widetilde{x_3}(n)|^{l}\Big) + C_2 \\
\widetilde{y_3}(n) &= \sum_{m=0}^{M}\sum_{i=0}^{N_1}\sum_{s=0}^{i}\sum_{l=0}^{s}\Big(h_{misl}^{(3)}\widetilde{x_3}(n)|\widetilde{x_3}(n)|^{i-s}|\widetilde{x_1}(n)|^{s-l}|\widetilde{x_2}(n)|^{l} \\
&\qquad + q_{misl}^{(3)}\widetilde{x_3}^{*}(n)|\widetilde{x_3}(n)|^{i-s}|\widetilde{x_1}(n)|^{s-l}|\widetilde{x_2}(n)|^{l}\Big) + C_3
\end{aligned} \tag{3.3}$$

où $h_{misl}^{(k)}$, $q_{misl}^{(k)}$ et C_k pour $k = \{1,2,3\}$, sont les coefficients du modèle, les coefficient de la partie conjuguée du modèle et la valeur DC, respectivement.

Dans la section suivante, on va monter comment trouver l'inverse du ce modèle, afin d'établir son DPD.

3.3 Conception du DPD

On peut écrire (3.3) sous la forme matricielle suivante :

$$\begin{aligned}
\hat{\boldsymbol{y}} &= \boldsymbol{h}\widetilde{\boldsymbol{X_{in}}} + \boldsymbol{q}\widetilde{\boldsymbol{X_{in}}}^{*} \\
&= \underbrace{\left[\widetilde{\boldsymbol{X_{in}}} \quad \widetilde{\boldsymbol{X_{in}}}^{*}\right]}_{\widetilde{\boldsymbol{X}}} \underbrace{\begin{bmatrix}\boldsymbol{h}\\ \boldsymbol{q}\end{bmatrix}}_{\boldsymbol{\omega}} \\
\hat{\tilde{\boldsymbol{y}}} &= \widetilde{\boldsymbol{X}}\boldsymbol{\omega}
\end{aligned} \tag{3.4}$$

Où $\hat{\tilde{\boldsymbol{y}}}$ est un vecteur de P*1 des échantillons de $\tilde{y}_k(n)$. $\widetilde{X_{in}}$ et $\widetilde{X_{in}}^{*}$ sont les matrices de taille P*R qui contiennent les échantillons de l'entrée et leur conjugué, respectivement. *h* et *q* sont les vecteurs de taille R*1 représentant les coefficients de la partie principale du modèle et la partie conjugué, respectivement.

On a remplacé les échantillons de l'entrée et de la sortie et on obtient l'Eq (3.5) comme le modèle inverse :

$$\hat{\tilde{\boldsymbol{x}}} = \widetilde{\boldsymbol{Y}}\boldsymbol{\omega} \tag{3.5}$$

On a calculé l'erreur entre les échantillons d'entrée émis et leurs estimations :

$$e(n) = \tilde{x}(n) - x(n) \tag{3.6}$$

Afin de minimiser cette erreur, on a appliqué la méthode des moindres carrés :

$$\boldsymbol{\omega} = \left(\tilde{\boldsymbol{Y}}^H \tilde{\boldsymbol{Y}}\right)^{-1} \tilde{\boldsymbol{Y}}^H \tilde{\boldsymbol{x}} \tag{3.7}$$

3.3 Les résultats de simulation et expérimentaux

On a généré un signal agrégé en fréquence avec les configurations données au Tableau 6.

RF Frequency	$f_1 = 2.2$ GHz	$f_2 = 2.5$ GHz	$f_3 = 2.9$ GHz	$f_c = 2.52$ GHz
LI Frequency	$h_1 = -320$ MHz	$h_2 = -20$ MHz	$h_3 = 380$ MHz	$\eta = 30$ MHz
Power	-42 dBm	-42 dBm	-42 dBm	10 dBm
Bandwidth	10 MHz	10 MHz	10 MHz	–
Sampling rate	3.36 GHz	3.36 GHz	3.36 GHz	–
Modulation	QPSK-OFDM			CW
N	32			–
L	8			–
DC-Null Subcarrier	✓			–
TS	CAZAC			–

Tableau 6 La spécification du signal agrégé en fréquence

Le banc de test du DPD est affiché dans la Figure 15 où on échantillonne les porteuses à la sortie du modulateur I/Q avec le VSA. Ces échantillons sont utilisés afin d'établir le modèle matriciel donnée en (3.4).

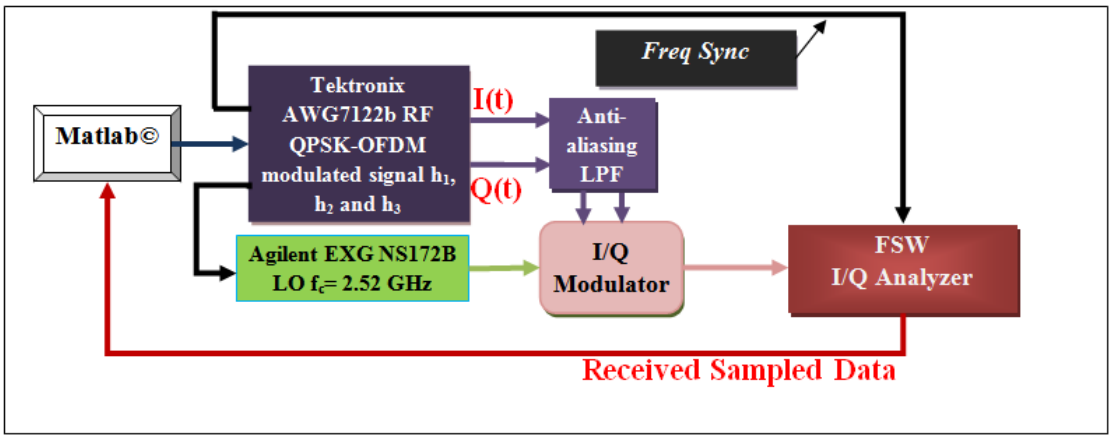

Figure 15 Le banc du teste de DPD

Le Tableau 7 montre les erreurs quadratiques (MSE) simulées pour une longueur de mémoire de M et un ordre de non linéarité de 3. La valeur de MSE pour un cas sans DPD est de 13×10^{-4}. On observe que en appliquant le DPD avec un M= 2 on gagne un facteur de 3250.

M	0	1	2	3	4	5
MSE	1.6×10^{-4}	1.3×10^{-4}	4×10^{-7}	2.4×10^{-6}	1.1×10^{-6}	8.1×10^{-7}

Tableau 7 L'erreur quadratique pour un effet mémoire M et une ordre de non linéarité de 3

La Figure 16 montre le spectre du signal en sortie de modulateur sans avoir appliqué le DPD.

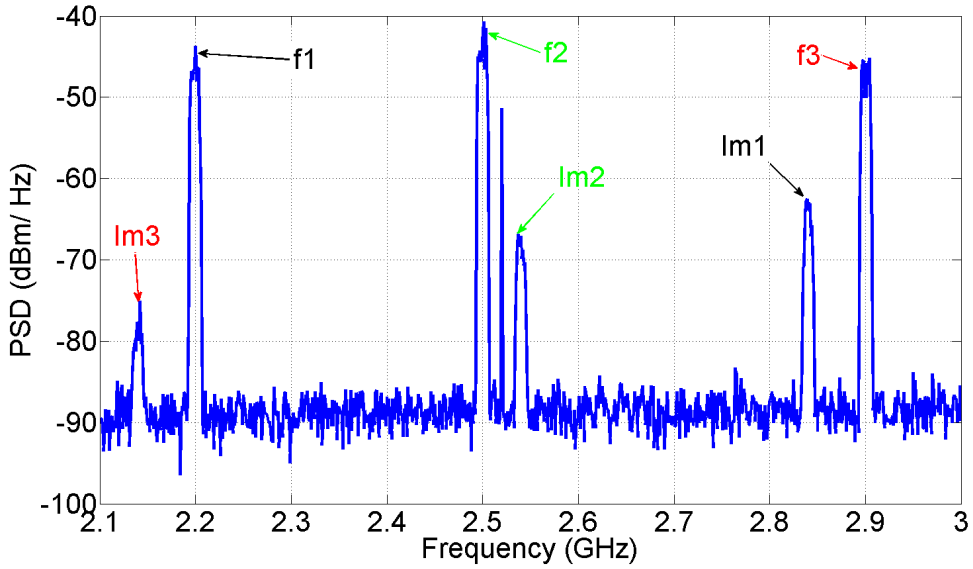

Figure 16 Le spectre à la sortie du modulateur sans DPD

Après avoir appliqué notre DPD, en pratique, pour un M et N de 2 et 3, respectivement, on a obtenu une forte rejection sur les niveaux de signaux parasite comme affiché dans la Figure 17. On observe une réjection de 20 dB, 3 dB et 5 dB sur les signaux d'images sur les Figures 17 (a), (b) et (c). On observe que les porteuses ne sont pas affectées par le DPD.

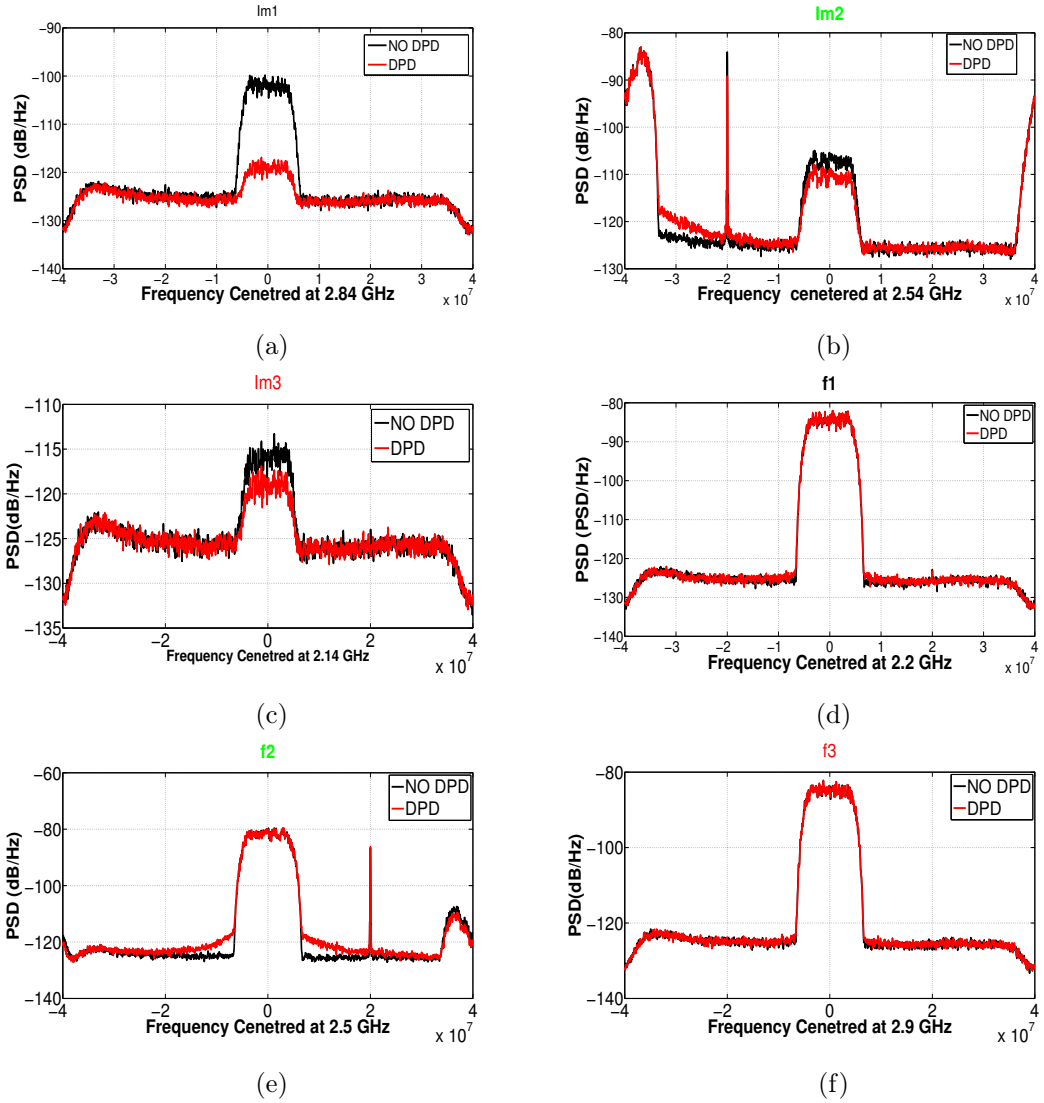

3.3 La conclusion

Dans ce chapitre, nous avons montré que les modèles comportementaux de linéarisation des amplificateurs de puissance étaient aussi utilisables pour modéliser le comportement des modulateurs I/Q mono et multi bandes. On a adapté un modèle développé pour un amplificateur de puissance 3 bandes pour modéliser un modulateur I/Q trois bandes et ses déséquilibres I/Q. On a simulé et implémenté notre modèle et son DPD et on a obtenu une forte réjection sur les signaux d'images.

Conclusion

Au cours de cette dissertation, différents aspects des communications RF ont été étudiés et développés. On a mis l'accent sur les communications LTE et LTE-A qui sont largement utilisées dans la technologie 4G et au-delà. Pour augmenter le débit de données dans le spectre dense RF, le 3GPP a proposé un concept pour utiliser simultanément plusieurs porteuses sur différentes parties du spectre. Ce concept est appelé agrégation de porteuse (CA). Les communications utilisant de multi-bandes de fréquence présentent certaines difficultés comme la consommation et l'encombrement des émetteurs et récepteurs ainsi que les interactions entre les différentes bandes de fréquence. Cette thèse a exploré ces différents problèmes et a essayé d'apporter quelques solutions.

Dans le premier chapitre, la thèse démontre que n oscillateurs locaux LO des récepteurs peuvent être remplacés par un dispositif LO, 2 DAC et un modulateur I / Q. Les deux DAC sont utilisés pour générer l'enveloppe complexe d'un signal LIF multi-tons, composé de multiples signaux sinusoïdaux, dont les fréquences sont réparties sur des fréquences intermédiaires LIF positives et négatives. De cette façon, on obtient une réduction d'un facteur de deux de la fréquence d'échantillonnage des DAC. Il a été montré que l'amplitude de chaque ton était contrôlable numériquement. De plus, les déséquilibres en amplitude et phase du modulateur I / Q induisant une fuite du signal Lo ont été étudiées et analysées. La structure a été simulée dans l'environnement Matlab. Elle a été mise en œuvre pratiquement et des niveaux de signaux parasites SFDR de 52 dB et 50 dB ont été obtenus respectivement pour le signal LO à 3 tons et le signal LO à 4 tons. Ce signal LO multi-tons est utilisé dans un récepteur TPD LTE-A pour convertir en même temps toutes les bandes de fréquence du signal CA transmis. En utilisant cette structure, plusieurs chaînes de réception (DAC, Modulateur I/Q et LO) sont remplacées par une. Enfin, nous avons montré que le taux d'échantillonnage du DAC est beaucoup plus faible dans notre structure que dans le cas où le signal est directement synthétisé de la bande de base à la RF en utilisant des DAC de haute performance. Sur la base du critère de Nyquist pour synthétiser un signal, la fréquence d'échantillonnage doit être au moins deux fois supérieure à sa composante de fréquence la plus élevée. Par conséquent, pour synthétiser directement un signal multi ton à 2,00 GHz, 2,03 GHz et 2,07 GHz, une fréquence d'échantillonnage de 4,14 GS/s est nécessaire, alors que dans notre structure le même signal est généré avec une fréquence d'échantillonnage de 135 MS/s.

Dans le deuxième chapitre, nous nous sommes concentrés sur l'émetteur LTE-A et avons adapté la structure du générateur multi tons développé au chapitre un pour générer un signal CA. Tout d'abord, le processus de modulation et de démodulation du signal OFDM ainsi que leurs considérations pratiques ont été expliqués. Ensuite, une solution de diversité de fréquence a été proposée où des symboles OFDM identiques ont été transmis sur différentes bandes de fréquences. La structure a été développée pour transmettre des symboles OFDM différents sur 3 bandes de fréquences, ce qui est requis dans la norme LTE-A. La structure peut être adaptée au cas de n bandes de fréquences en modifiant le développement mathématique pour créer l'enveloppe complexe du signal CA. En utilisant notre méthode, les porteuses du signal LTE-A ont été générés à l'aide d'un seul modulateur I/Q , d'un signal LO et de deux Dac. Comme dans le cas multi-tons, cette structure nécessite moins d'équipement, car une seule chaîne d'émission est utilisée pour générer toutes les bandes de fréquences. Grâce au choix du signal LIF, comportant des fréquences positives et négatives, on réduit également le taux d'échantillonnage du DAC par rapport à la génération directe de signaux RF. Nous avons montré que pour générer 3 porteurs de composantes à 2,2 GHz, 2,5 GHz et 2,9 GHz, une fréquence d'échantillonnage de 1,14 GS/s est requise en utilisant notre structure, alors que dans la synthèse directe RF, un taux d'échantillonnage d'au moins 5,8 GS/s est nécessaire . De plus, les déséquilibres d'I / Q et la fuite du signal LO ont été étudiés et une solution de compensation numérique par look-up table a été proposée. Enfin, la démodulation des signaux a été expliquée en détail, en utilisant un démodulateur multi bandes appelé TPD. Les signaux ont également été démodulés à l'aide d'un analyseur de signal vectoriel mono-bande commercial (VSA) et leurs résultats ont été comparés. Un ACLR de 43 dB a été obtenu avec notre structure, en outre, un EVM de -28 dB a été obtenu par le démodulateur VSA pour un signal 64-QAM à -42 dBm.

Dans le troisième chapitre, la fonctionnalité du système a été étudiée pour compenser ses défauts en utilisant des techniques de pré distorsion numérique. Nous avons modélisé le système en utilisant les échantillons de sortie et d'entrée sans entrer dans le détail de chaque composant du système. Cette méthode est appelée modélisation comportementale. Nous avons proposé un modèle multi-bandes comportemental pour compenser les faibles non-linéarités des modulateurs I/Q en présence de ses déséquilibres en amplitude et phase. De plus, l'inverse du modèle a été obtenu à l'aide de l'apprentissage indirect et de l'algorithme des moindres carrés. Le signal inverse, appelé signal DPD, est fourni au modulateur pour linéariser et corriger sa sortie. La simulation et les résultats expérimentaux ont été présentés

pour confirmer la fonctionnalité du modèle. Les simulations ont montré qu'avec une profondeur de mémoire de 2 et un ordre de non-linéarité de 3, une amélioration de 3250 est obtenue en erreur quadratique moyenne du signal de sortie par rapport au cas où aucun DPD n'est utilisé. De plus, nous avons obtenu, par mesure, une rejection de de 20 dB sur des signaux parasites images.

Perspectives

Il ya certains aspects de ce travail que l'on devrait développer. Les nouvelles configurations de signaux CA doivent être mises en œuvre et évaluées. Par exemple, des signaux CA avec des largeurs de bande de fréquence et des modulations différentes doivent être mis en œuvre. Ces combinaisons peuvent être sensibles puisque, le concepteur doit s'assurer d'avoir le même nombre d'échantillons dans chaque bande de fréquence. De plus, la structure de génération de signal a été mise en œuvre en utilisant un générateur de forme d'onde arbitraire, elle devrait également être mise en œuvre en utilisant un circuit FPGA pour des applications en temps réel. D'autre part, la performance de notre DPD doit être étudiée en présence d'un amplificateur de puissance multi-bandes (cas avec des non-linéarités fortes). De plus, les performances du DPD doivent être améliorées en effectuant plusieurs itérations des calculs des coefficients de la DPD. De plus, les performances et la stabilité du DPD dans des intervalles de temps longs et des températures différentes doivent être étudiées. La technique CA est utilisée dans différentes technologies telles que 5G . En 5G, les largeurs de bande de chaque sous bande de fréquence sont beaucoup plus élevées que dans le LTE-A, par conséquent, de nouvelles structures DPD doivent être développées pour tenir compte de la très grande largeur de bande de fréquence. De plus, d'autres types de formes d'onde sont proposés pour 5G tels que FBMC, UFMC, GFDM et F-OFDM qu’il faudra mettre en œuvre dans notre structure.

Bibliography

[1] L'attribution des fréquences de la bande 700 MHz. url = http://www.arcep.fr/index.php?id=12899.

[2] A. Biondi, F. Declercq, D. D. Zutter, H. Rogier, and L. Vallozzi. Electromagnetic compatibility aware design and testing of intermodulation distortion under multiple co-located sources illumination. *IET Science, Measurement Technology*, 6(2):105–112, March 2012.

[3] A. Biondi, H. Rogier, D. Vande Ginste, and D. De Zutter. Multi-tone EMC testing strategy for RF-devices. In *2012 IEEE Electrical Design of Advanced Packaging and Systems Symposium (EDAPS)*, pages 89–92, December 2012.

[4] Behzad Razavi. *RF Microelectronics (2Nd Edition) (Prentice Hall Communications Engineering and Emerging Technologies Series)*. Prentice Hall Press, Upper Saddle River, NJ, USA, 2nd edition, 2011.

[5] A. Kaissoine and B. Huyart. Demodulation of RF Signal Aggregating Four Non-Contiguous Frequency Carriers. In *Electronics, Circuits, and Systems (ICECS), 2014 IEEE 21th International Conference*, Marseille, December 2014. IEEE.

[6] A. O. Olopade and M. Helaoui. Mitigation of distortion and memory effect in a concurrent dual-band six port receiver. In *Microwave Conference (EuMC), 2014 44th European*, pages 1138–1141, October 2014.

[7] A.K. Lu and G.W. Roberts. An oversampling-based analog multitone signal generator. *IEEE Transactions on Circuits and Systems II: Analog and Digital Signal Processing*, 45(3):391–394, March 1998.

[8] Sylvain Traverso, Myriam Ariaudo, Jean-Luc Gautier, Inbar Fijalkow, and Christian Lereau. A 14-Band Low-Complexity and High-Performance Synthesizer Architecture for MB-OFDM Communication. *IEEE Transactions on Circuits and Systems II: Express Briefs*, 54(6):552–556, June 2007. bibtex: traverso_14-band_2007.

[9] Sylvain Traverso, Myriam Ariaudo, Jean-Luc Gautier, Inbar Fijalkow, and Christian Lereau. A 14-Band Low-Complexity and High-Performance Synthesizer Architecture for MB-OFDM Communication. *IEEE Transactions on Circuits and Systems II: Express Briefs*, 54(6):552–556, June 2007.

[10] L.J. Greenstein and P. Fitzgerald. Phasing Multitone Signals to Minimize Peak Factors. *IEEE Transactions on Communications*, 29(7):1072–1074, July 1981.

[11] Keysight E8257d/67d & E8663d PSG Signal Generators, March 2016.

[12] L. Cordesses. Direct digital synthesis: a tool for periodic wave generation (part 1). *IEEE Signal Processing Magazine*, 21(4):50–54, July 2004.

[13] MT-085 Tutorial: Fundamentals of Direct Digital Synthesis (DDS).

[14] ETSI Standard. 3gpp TR 36.912 version 10.0.0 Release 10. 2008.

[15] ETSI TS 136 211 V10.0.0 (2011-01) LTE; Evolved Universal Terrestrial Radio Access (E-UTRA); Physical channels and modulation.

[16] A.O. Olopade, A. Hasan, and M. Helaoui. Concurrent Dual-Band Six-Port Receiver for Multi-Standard and Software Defined Radio Applications. *IEEE Transactions on Microwave Theory and Techniques*, 61(12):4252–4261, 2013.

[17] A. Kaissoine, B. Huyart, and K. Mabrouk. Demodulation of aggregated RF signal in three frequencies bands with a unique Rx chain. pages 561–564, 2013.

[18] Mike Arnold Randy Class Francesco Dantoni Shrinivasan Jaganathan and Roland Sperlich. LO Harmonic Effects on I/Q Balance and Sideband Suppression in Complex I/Q Modulators. Technical report, 05 2010.

[19] N. Poobuapheun, W. h Chen, Z. Boos, and A. M. Niknejad. A 1.5v 0.7-2.5ghz CMOS Quadrature Demodulator for Multi-Band Direct-Conversion Receivers. In *IEEE Custom Integrated Circuits Conference 2006*, pages 797–800, September 2006.

[20] Keysight x-series signal generators.

[21] T. Kaho, Y. Yamaguchi, H. Shiba, K. Akabane, K. Uehara, and K. Araki. A simultaneous receiving multi-band mixer with independent gain control. In *Asia-Pacific Microwave Conference 2011*, pages 383–386, 2011.

[22] R. Chen and H. Hashemi. Dual-Carrier Aggregation Receiver With Reconfigurable Front-End RF Signal Conditioning. *IEEE Journal of Solid-State Circuits*, 50(8):1874–1888, August 2015.

[23] R. Chen and H. Hashemi. 19.3 Reconfigurable SDR receiver with enhanced front-end frequency selectivity suitable for intra-band and inter-band carrier aggregation. In *2015 IEEE International Solid-State Circuits Conference - (ISSCC) Digest of Technical Papers*, pages 1–3, February 2015.

[24] Bernard Huyart and Kaïs Mabrouk. Demodulation circuit, December 2012. U.S. Classification 329/304, 329/305, 329/306, 375/330, 329/310, 375/329, 375/334; International Classification H04L27/22; Cooperative Classification H03D3/007; European Classification H03D3/00C.

[25] TeliaSonera. First in the world with 4g - TeliaSonera History. http://www.teliacompanyhistory.com/pioneering-the-future/pioneering-the-future/first-in-the-world-with-4g/, 2009. [Online; accessed 20-July-2016].

[26] 3GPP. ETSI TS 136 211 V10.0.0 (2011-01) LTE; Evolved Universal Terrestrial Radio Access (E-UTRA); Physical channels and modulation, 2011. [Online; accessed 20-July-2016].

[27] Yun Rui, Peng Cheng, Mingqi Li, Q. T. Zhang, and Mohsen Guizani. Carrier aggregation for LTE-advanced: uplink multiple access and transmission enhancement features. *IEEE Wireless Communications*, 20(4):101–108, 2013.

[28] Ian F. Akyildiz, David M. Gutierrez-Estevez, and Elias Chavarria Reyes. The evolution to 4g cellular systems: LTE-Advanced. *Physical Communication*, 3(4):217–244, December 2010.

[29] ETSI . TS 136 306 - V10.6.0 - LTE; Evolved Universal Terrestrial Radio Access (E-UTRA); User Equipment (UE) radio access capabilities (3gpp TS 36.306 version 10.6.0 Release 10).

[30] ARCEP. Décision autorisant la société française du radiotéléphone à utiliser des fréquences dans la bande 2,6 GHz en France métropolitaine pour établir et exploiter un réseau radioélectrique mobile ouvert au public. [Online; accessed 19-July-2016].

[31] ARCEP. Décision autorisant la société Orange France à utiliser des fréquences dans la bande 2,6 GHz en France métropolitaine pour établir et exploiter un réseau radioélectrique mobile ouvert au public. [Online; accessed 19-July-2016].

[32] ARCEP. Décision autorisant la société Free Mobile à utiliser des fréquences dans la bande 2,6 GHz en France métropolitaine pour établir et exploiter un réseau radioélectrique mobile ouvert au public. [Online; accessed 19-July-2016].

[33] ARCEP. Décision autorisant la société Bouygues Telecom à utiliser des fréquences dans la bande 2,6 GHz en France métropolitaine pour établir et exploiter un réseau radioélectrique mobile ouvert au public. [Online; accessed 19-July-2016].

[34] ARCEP. Décision n° 2015-1080 de l'Autorité de régulation des communications électroniques et des postes en date du 8 septembre 2015 modifiant la décision n°

2014-1542 autorisant la société Free Mobile à utiliser des fréquences dans la bande 1800 MHz pour établir et exploiter un réseau radioélectrique ouvert au public. [Online; accessed 19-July-2016].

[35] ARCEP. 4g SPECTRUM ALLOCATION ARCEP publishes the results of the allocation procedure for 4g mobile licences in the 800 MHz band (the digital dividend). [Online; accessed 19-July-2016].

[36] ARCEP. 700 MHZ BAND Final results of the allocation procedure. [Online; accessed 19-July-2016].

[37] S. S. Jeon, Y. Wang, Y. Qian, and T. Itoh. Mixing of Technologies for Adaptive Beamforming Implementation. In *Microwave Conference, 2001. 31st European*, pages 1–4, September 2001.

[38] L. Liu, R. Chen, S. Geirhofer, K. Sayana, Z. Shi, and Y. Zhou. Downlink MIMO in LTE-advanced: SU-MIMO vs. MU-MIMO. *IEEE Communications Magazine*, 50(2):140–147, February 2012.

[39] H. Vaidya, R. Raman, and M.R. Kamath. Transitioning from mimo to siso to save power. https://www.google.com/patents/US9144025, September 22 2015. US Patent 9,144,025.

[40] ETSI . TS 136 306 - V10.6.0 - LTE; Evolved Universal Terrestrial Radio Access (E-UTRA); User Equipment (UE) radio access capabilities (3gpp TS 36.306 version 10.6.0 Release 10). http://www.etsi.org/deliver/etsi_ts/136300_136399/136306/10.06.00_60/ts_136306v100600p.pdf.

[41] David Tse and Pramod Viswanath. *Fundamentals of Wireless Communication*. Cambridge University Press, New York, NY, USA, 2005.

[42] Philippe Ciblat. Partie 1: Gestion de l'interférence entre symboles. = http://perso.telecom-paristech.fr. [COM921 course slides].

[43] M. Salehi and J. Proakis. *Digital Communications*. McGraw-Hill Education, 2007. bibtex: salehi2007digital.

[44] Ransom Stephens. Equalization: The Correction and Analysis of Degraded Signals. [White paper].

[45] H. Sari, G. Karam, and I. Jeanclaude. Transmission techniques for digital terrestrial tv broadcasting. *IEEE Communications Magazine*, 33(2):100–109, Feb 1995.

[46] D. C. Chang. Effect and Compensation of Symbol Timing Offset in OFDM Systems With Channel Interpolation. *IEEE Transactions on Broadcasting*, 54(4):761–770, December 2008.

[47] Q. Cheng. Residue carrier frequency offset estimation using cyclic prefix in OFDM systems. In *TENCON 2009 - 2009 IEEE Region 10 Conference*, pages 1–5, January 2009.

[48] J. Van De Beek, Magnus Sandell, P. Borjesson, J. Van De Beek, M. Sandell, and P. Borjesson. On synchronization in OFDM systems using the cyclic prefix. *Division of Signal Processing, Lulea University of Technology, Lulea, Sweden*, pages 1–5, 1996.

[49] S. Kapoor, D. J. Marchok, and Y. F. Huang. Pilot assisted synchronization for wireless OFDM systems over fast time varying fading channels. In *48th IEEE Vehicular Technology Conference, 1998. VTC 98*, volume 3, pages 2077–2080 vol.3, May 1998.

[50] F. Classen and H. Meyr. Frequency synchronization algorithms for OFDM systems suitable for communication over frequency selective fading channels. In *Vehicular Technology Conference, 1994 IEEE 44th*, pages 1655–1659 vol.3, June 1994.

[51] T.M. Schmidl and D.C. Cox. Robust frequency and timing synchronization for OFDM. *IEEE Transactions on Communications*, 45(12):1613–1621, December 1997.

[52] Guangliang Ren, Yilin Chang, Hui Zhang, and Huining Zhang. Synchronization method based on a new constant envelop preamble for OFDM systems. *IEEE Transactions on Broadcasting*, 51(1):139–143, March 2005.

[53] ETSI TS 136 101 V8.3.0.

[54] Chester Sungchung Park, A. Khayrallah, and others. Carrier aggregation for LTE-advanced: design challenges of terminals. *Communications Magazine, IEEE*, 51(12):76–84, 2013.

[55] Fredrik Nordström, Niklas Andgart, and Bengt Lindoff. Wireless communication methods and receivers for receiving and processing multiple component carrier signals, November 2011. US Patent 8,050,343.

[56] Yoan Veyrac, Francois Rivet, Yann Deval, Dominique Dallet, Patrick Garrec, and Richard Montigny. A 65-nm CMOS DAC Based on a Differentiating Arbitrary Waveform Generator Architecture for 5g Handset Transmitter. *IEEE Transactions on Circuits and Systems II: Express Briefs*, 63(1):104–108, January 2016.

[57] M.A. Abyaneh, A. Kaissoine, B. Huyart, and J. Cousin. Multiple RF Continuous-Wave generation using a single signal generator for carrier agrregation in LTE-advanced. In *European Microwave Conference (EuMC), 2014 44th*, pages 1246–1248, October 2014.

[58] M. A. Abyaneh, B. Huyart, and J. Cousin. Qpsk-ofdm carrier aggregation using a single transmission chain. In *2015 IEEE MTT-S International Microwave Symposium*, pages 1–4, May 2015.

[59] Agilent Option UND Generating Digital Modulation with the Agilent ESG-D Series Dual Arbitrary Waveform Generator. Product Note.

[60] Chang-Ming Lai, Je-Kuan Jau, Ping-Hsun Wu, Chun-Hsiang Chi, Chia-Hao Tu, and Jian-Yu Li. CMOS RF T/R router switch ICs for LTE carrier aggregation transceivers. pages 904–907, October 2012.

[61] Takashi Maehata, Kazuyuki Totani, Suguru Kameda, and Noriharu Suematsu. Concurrent dual-band 1-bit digital transmitter using band-pass delta-sigma modulator. pages 1523–1526, 2013.

[62] SungWon Chung, Rui Ma, Koon Hoo Teo, and K. Parsons. Outphasing multi-level RF-PWM signals for inter-band carrier aggregation in digital transmitters. pages 212–214, January 2015.

[63] R. Rajbanshi, Alexander M. Wyglinski, and G.J. Minden. An Efficient Implementation of NC-OFDM Transceivers for Cognitive Radios. pages 1–5, June 2006.

[64] Zhu Fu, L. Anttila, M. Valkama, and Alexander M. Wyglinski. Digital predistortion of power amplifier impairments in spectrally agile transmissions. pages 1–6, 2012.

[65] Sérgio Juliao, Francisco Martins, André Prata, Sérgio Lopes, Joao Duarte, Paulo Jesus, Nelson Silva, Arnaldo SR Oliveira, and Nuno B. Carvalho. High Performance Microwave Point-to-Point Link for 5g Backhaul with Flexible Spectrum Aggregation.

[66] Yang Wen, Wei Huang, and Zhongpei Zhang. CAZAC sequence and its application in LTE random access. In *2006 IEEE Information Theory Workshop-ITW'06 Chengdu*, pages 544–547. IEEE, 2006.

[67] Eamon Nash. Correcting imperfections in IQ modulators to improve RF signal fidelity. *AN-1039, Application Note, Analog Devices*, 2009.

[68] Suk Keun Myoung, Xian Cui, D. Chaillot, P. Roblin, F. Verbeyst, M. V. Bossche, Seok Joo Doo, and Wenhua Dai. Large signal network analyzer with trigger for baseband RF system characterization with application to K-modeling output baseband modulation linearization. pages 189–195, December 2004.

[69] G. Neveux, B. Huyart, and G.J. Rodriguez-Guisantes. Wide-Band RF Receiver

Using the "Five-Port" Technology. *IEEE Transactions on Vehicular Technology*, 53(5):1441–1451, September 2004.

[70] A. Kaissoine, B. Huyart, and K. Mabrouk. Demodulation of aggregated rf signal in three frequencies bands with a unique rx chain. In *Microwave Conference (EuMC), 2013 European*, pages 561–564, Oct 2013.

[71] M. Younes, A. Kwan, M. Rawat, and F.M. Ghannouchi. Three-Dimensional digital predistorter for concurrent tri-band power amplifier linearization. In *Microwave Symposium Digest (IMS), 2013 IEEE MTT-S International*, pages 1–4, June 2013.

[72] Zhebin Wang and Chan-Wang Park. Concurrent tri-band GaN HEMT power amplifier using resonators in both input and output matching networks. In *Wireless and Microwave Technology Conference (WAMICON), 2012 IEEE 13th Annual*, pages 1–4, April 2012.

[73] F. H. Raab, P. Asbeck, S. Cripps, P. B. Kenington, Z. B. Popovic, N. Pothecary, J. F. Sevic, and N. O. Sokal. Power amplifiers and transmitters for RF and microwave. *IEEE Transactions on Microwave Theory and Techniques*, 50(3):814–826, March 2002.

[74] Khalid H. Abed, M. K. Kazimierczuk, S. B. Nerurkar, and M. P. Senadeera. Linearization techniques in power amplifiers for 1.9 ghz wireless transmitters. In *48th Midwest Symposium on Circuits and Systems, 2005.*, pages 1103–1106. IEEE, 2005.

[75] A.J. Zozaya and E. Bertran. On the Performance of Cartesian Feedback and Feedforward Linearization Structures Operating at 28 GHz. *IEEE Transactions on Broadcasting*, 50(4):382–389, December 2004.

[76] Peter B. Kenington. *High Linearity RF Amplifier Design.* Artech House, Inc., Norwood, MA, USA, 1st edition, 2000.

[77] F. M. Ghannouchi and O. Hammi. Behavioral modeling and predistortion. *IEEE Microwave Magazine*, 10(7):52–64, Dec 2009.

[78] J. Vuolevi, T. Rahkonen, and J. Manninen. Measurement technique for characterizing memory effects in rf power amplifiers. In *Radio and Wireless Conference, 2000. RAWCON 2000. 2000 IEEE*, pages 195–198, 2000.

[79] W. Bosch and G. Gatti. Measurement and simulation of memory effects in predistortion linearizers. *IEEE Transactions on Microwave Theory and Techniques*, 37(12):1885–1890, Dec 1989.

[80] Taijun Liu, S. Boumaiza, A.B. Sesay, and F.M. Ghannouchi. Quantitative measurements of memory effects in wideband rf power amplifiers driven by modulated signals. *Microwave and Wireless Components Letters, IEEE*, 17(1):79–81, 2007.

[81] A. Zhu, J. C. Pedro, and T. R. Cunha. Pruning the volterra series for behavioral modeling of power amplifiers using physical knowledge. *IEEE Transactions on Microwave Theory and Techniques*, 55(5):813–821, May 2007.

[82] A. Zhu, J. C. Pedro, and T. J. Brazil. Dynamic deviation reduction-based volterra behavioral modeling of rf power amplifiers. *IEEE Transactions on Microwave Theory and Techniques*, 54(12):4323–4332, Dec 2006.

[83] P. Gilabert, G. Montoro, and E. Bertran. On the Wiener and Hammerstein models for power amplifier predistortion. In *2005 Asia-Pacific Microwave Conference Proceedings*, volume 2, pages 4 pp.–, December 2005.

[84] F.M. Ghannouchi and O. Hammi. Behavioral modeling and predistortion. *IEEE Microwave Magazine*, 10(7):52–64, December 2009.

[85] J. Kim and K. Konstantinou. Digital predistortion of wideband signals based on power amplifier model with memory. *Electronics Letters*, 37(23):1417–1418, November 2001.

[86] R. Raich, Hua Qian, and G. T. Zhou. Orthogonal polynomials for power amplifier modeling and predistorter design. *IEEE Transactions on Vehicular Technology*, 53(5):1468–1479, September 2004.

[87] D.R. Morgan, Zhengxiang Ma, Jaehyeong Kim, M.G. Zierdt, and J. Pastalan. A Generalized Memory Polynomial Model for Digital Predistortion of RF Power Amplifiers. *IEEE Transactions on Signal Processing*, 54(10):3852–3860, October 2006.

[88] Taijun Liu, S. Boumaiza, and F.M. Ghannouchi. Augmented hammerstein predistorter for linearization of broad-band wireless transmitters. *IEEE Transactions on Microwave Theory and Techniques*, 54(4):1340–1349, June 2006.

[89] Taijun Liu, S. Boumaiza, and F.M. Ghannouchi. Deembedding static nonlinearities and accurately identifying and modeling memory effects in wide-band RF transmitters. *IEEE Transactions on Microwave Theory and Techniques*, 53(11):3578–3587, November 2005.

[90] O. Hammi and F.M. Ghannouchi. Twin Nonlinear Two-Box Models for Power Amplifiers and Transmitters Exhibiting Memory Effects With Application to Digital Predistortion. *IEEE Microwave and Wireless Components Letters*, 19(8):530–532, August 2009.

[91] M. Grimm, M. Allén, J. Marttila, M. Valkama, and R. Thomä. Joint Mitigation of Nonlinear RF and Baseband Distortions in Wideband Direct-Conversion Receivers. *IEEE Transactions on Microwave Theory and Techniques*, 62(1):166–182, January 2014.

[92] X. Yang, D. Chaillot, P. Roblin, W. R. Liou, J. Lee, H. D. Park, J. Strahler, and M. Ismail. Poly-harmonic modeling and predistortion linearization for software-defined radio upconverters. *IEEE Transactions on Microwave Theory and Techniques*, 58(8):2125–2133, Aug 2010.

[93] S. A. Bassam, M. Helaoui, and F. M. Ghannouchi. 2-D Digital Predistortion (2-D-DPD) Architecture for Concurrent Dual-Band Transmitters. *IEEE Transactions on Microwave Theory and Techniques*, 59(10):2547–2553, October 2011.

[94] Ying Liu, P. Roblin, Hai Yu, Shihai Shao, and Youxi Tang. Novel multiband linearization technique for closely-spaced dual-band signals of wide bandwidth. In *2015 IEEE MTT-S International Microwave Symposium*, pages 1–4, May 2015.

[95] M. Younes and F. M. Ghannouchi. On the Modeling and Linearization of a Concurrent Dual-Band Transmitter Exhibiting Nonlinear Distortion and Hardware Impairments. *IEEE Transactions on Circuits and Systems I: Regular Papers*, 60(11):3055–3068, November 2013.

[96] Ying Liu, P. Roblin, Hai Yu, Shihai Shao, and Youxi Tang. Novel multiband linearization technique for closely-spaced dual-band signals of wide bandwidth. In *2015 IEEE MTT-S International Microwave Symposium*, pages 1–4, May 2015.

[97] M. Younes, A. Kwan, M. Rawat, and F. M. Ghannouchi. Linearization of Concurrent Tri-Band Transmitters Using 3-D Phase-Aligned Pruned Volterra Model. *IEEE Transactions on Microwave Theory and Techniques*, 61(12):4569–4578, December 2013.

[98] A. K. Kwan, M. Younes, F. M. Ghannouchi, S. Zhang, W. Chen, R. Darraji, M. Helaoui, and O. Hammi. Concurrent Multi-Band Envelope Modulated Power Amplifier Linearized Using Extended Phase-Aligned DPD. *IEEE Transactions on Microwave Theory and Techniques*, 62(12):3298–3308, December 2014.

[99] C. Yu, W. Cao, Y. Guo, and A. Zhu. Digital Compensation for Transmitter Leakage in Non-Contiguous Carrier Aggregation Applications With FPGA Implementation. *IEEE Transactions on Microwave Theory and Techniques*, 63(12):4306–4318, December 2015.

[100] Augusto Sarti and Silvano Pupolin. Recursive techniques for the synthesis of a pth-order inverse of a volterra system. *European Transactions on Telecommunications*, 3(4):315–322, 1992.

[101] B. Mohr, W. Li, and S. Heinen. Analysis of digital predistortion architectures for

direct digital-to-RF transmitter systems. In *2012 IEEE 55th International Midwest Symposium on Circuits and Systems (MWSCAS)*, pages 650–653, August 2012.

[102] D. Zhou and V. E. DeBrunner. Novel Adaptive Nonlinear Predistorters Based on the Direct Learning Algorithm. *IEEE Transactions on Signal Processing*, 55(1):120–133, January 2007.

[103] Changsoo Eun and E. J. Powers. A new Volterra predistorter based on the indirect learning architecture. *IEEE Transactions on Signal Processing*, 45(1):223–227, January 1997.

[104] Qin Zhang and Zhibin Zeng. A new adaptive algorithm for digital predistortion using LS with singular value decomposition. In *Proc. Int. Conf. Inf. Sci. Technol. Applicat.(ICISTA)*, pages 169–172, 2013.

[105] Least-Squares Fitting. http://fr.mathworks.com/help/curvefit/least-squares-fitting.html. pages 916 - 921.

[106] V.K. Ingle and J.G. Proakis. *Digital Signal Processing Using MATLAB*. Cengage Learning, 3rd edition, 2011. pages 596- 598.

[107] John G. Proakis and Dimitris K. Manolakis. *Digital Signal Processing (4th Edition)*. Prentice-Hall, Inc., Upper Saddle River, NJ, USA, 2006.

[108] Afif Osseiran, Federico Boccardi, Volker Braun, Katsutoshi Kusume, Patrick Marsch, Michal Maternia, Olav Queseth, Malte Schellmann, Hans Schotten, Hidekazu Taoka, and others. Scenarios for 5g mobile and wireless communications: the vision of the METIS project. *IEEE Communications Magazine*, 52(5):26–35, 2014.

[109] Jeffrey G. Andrews, Stefano Buzzi, Wan Choi, Stephen V. Hanly, Angel Lozano, Anthony C. K. Soong, and Jianzhong Charlie Zhang. What Will 5g Be? *IEEE Journal on Selected Areas in Communications*, 32(6):1065–1082, June 2014.

[110] Abdou Kaissoine. *Demodulation of Frequency Agrregated 4G (LTE-Advanced) Signal.* thesis dissertation, Telecom Paristech, Paris, March 2015.

Génération des signaux agrégés en fréquences dans le contexte de LTE-A

RESUME : Dans ce travail de thèse, on a proposé une structure de génération des signaux multi-porteuse afin de créer plusieurs oscillateurs locaux (OL) tout en utilisant qu'un modulateur I/Q. Ces signaux peuvent être utilisés dans les récepteurs de LTE-A pour la transposition des signaux agrégé en fréquence vers la bande de base. On développe la structure afin de l'utiliser en émetteur répondant aux normes du standard LTE-A. La nouvelle structure nous permet de générer n signaux agrégés en fréquences, de manière simultanée, par une seule chaine de transmission (c.a.d un modulateur I/Q, un OL). En utilisant cette structure on réduit le nombre de circuits utilisés, en comparaison du cas où n signaux agrégés en fréquences sont générés par n émetteurs. La fréquence d'échantillonnage est réduite dans notre cas par rapport au cas où les signaux sont générés directement de la bande de base à la bande RF avec des convertisseurs analogiques numériques adéquats. Dans la troisième partie, on se concentre sur les imperfections et les non linéarités du modulateur I/Q dans le cadre de notre structure multi-bande. On modélise le fonctionnement du modulateur multi-bande en utilisant les échantillons en entrée et en sortie. Notre modèle est dérivé de la série de Volterra qui prends en compte les effets non linéaires et les effets mémoires ainsi que les imperfections du modulateur I/Q. Puis, on obtient la fonction "inverse" du modèle et on l'applique à l'entrée du modulateur afin de corriger et linéariser la sortie du modulateur I/Q. La fonction "inverse" est appelée DPD (*en anglais : Digital Pre-Distortion*). Enfin, on a évalué le modèle et la DPD en simulations et en mesures.

Mots clés : LTE-A, Agrégation en fréquences, DPD, Modulateur I/Q multi-bande, récepteurs très large bande, OFDM, Effets non linéaires, Effets mémoires

Carrier Aggregated Signal Generation for LTE-A

ABSTRACT : In this dissertation, a signal generation structure is proposed using which a multi-tone Local Oscillator (LO) signal is created by a single I/Q modulator. These LOs can be used in the CA receivers to down-convert the transmitted component carriers simultaneously. The multi-tone LO signal structure is further developed to be used at the transmitter as a CA generation solution. Using the proposed structure n-component carriers can be generated in parallel. This structures requires lower sampling rates with respect to the case where RF signals are synthesized directly by digital-to- analog converters. Moreover, less circuitry is required, because one single I/Q modulator is used to generate n component carriers, instead of n I/Q modulators.

This work follows on investigating the origin of impairments and mild nonlinearities in our I/Q modulator. To overcome these problems, we focus on the functionality of the overall system rather than each component of the I/Q modulator. This method is called behavioral modeling. Once the nonlinear model is obtained, if its inverse function is applied to the input, a linearized output is expected. The generation of the inverse function is called Digital Pre-Distortion (DPD). We propose a tri-band behavioral model for nonlinearities and impairments in tri-band CA using our I/Q modulator. Furthermore, the DPD of the model is evaluated in simulations and experiments.

Keywords : LTE-A, carrier aggregation, behavioral modeling, digital pre-distortion, multi-band I/Q modulator, wideband receivers, OFDM, I/Q modulator impairments, nonlinearities

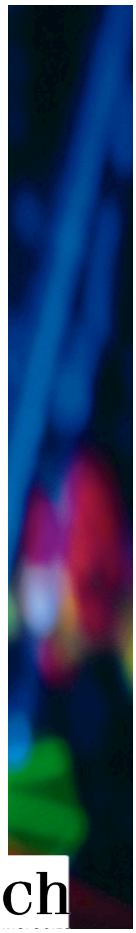

TELECOM ParisTech

ParisTech